

# Charting the low-loss region in Electron Energy Loss Spectroscopy with machine learning

Laurien Roest





# **Charting the low-loss region in Electron Energy Loss Spectroscopy with machine learning**

**Laurien Roest**

**4287320**

to obtain the degree of Master of Science in Applied Physics  
at Delft University of Technology,  
to be defended publicly on Thursday October 1st, 2020.

*Kavli Institute of Nanoscience, Delft University of Technology, 2628CJ Delft, The Netherlands  
Nikhef Theory Group, Science Park 105, 1098 XG Amsterdam, The Netherlands*

Thesis committee:

Dr. S. Conesa-Boj (Supervisor, QN)

Dr. E. Greplova (QN)

Dr. ir. J.P. Hoogenboom (ImPhys)

## Abstract

With the growing possibilities that two-dimensional (2D) materials can offer for nanodevices, so also grows the relevance to fully exploit their electronic, structural and chemical properties. Electron energy loss spectroscopy (EELS) offers a way to provide this valuable information at the nanoscale. Utilizing the information contained in EEL spectra requires reliable access to the low-loss region ( $\Delta E \lesssim$  few eV), where the contribution from the zero-loss peak (ZLP) overwhelms those from the inelastic interactions between the incident electrons and the specimen. An accurate removal of the ZLP contribution is crucial in order to efficiently chart and identify these low-loss features. In this work, we deploy machine learning techniques, inspired by particle physics applications, to realise a model-independent multidimensional determination of the ZLP with a faithful uncertainty estimate, which can be used to subtract its contribution from EEL spectra while propagating the associated uncertainties. Our method is used to disentangle the ZLP from the sample contributions in low-loss EEL spectra acquired in WS<sub>2</sub> nanostructures of different thicknesses. This makes it possible to determine not only the value and type of the WS<sub>2</sub> bandgap as a function of the underlying crystalline morphology of the nanostructures, but also to characterise exciton features arising in the ultra-low-loss region.

*Keywords:* Transmission Electron Microscopy, Electron Energy Loss Spectroscopy, Neural Networks, Bandgap, Transition Metal Dichalcogenides.

## Scientific output

The results presented in this work have been the basis for my first first-author paper. The paper has been submitted to the journal Ultramicroscopy and the pre-print can already be downloaded from the following arXiv submission: <https://arxiv.org/abs/2009.05050>.

With the method presented, I have contributed to the scientific publication of my colleague, making me co-author in the corresponding paper. This paper has been submitted to Nature Materials and the pre-print can be found in the following: <https://arxiv.org/abs/2009.08477>.

The code that I developed for the purpose of this study is made available in an open-source Python-based framework dubbed **EELSfitter**, which can be accessed from its GitHub repository

<https://github.com/LHCfitNikhef/EELSfitter>.

We provide installation and usage instructions in Appendix A.

# Contents

<b>1</b>	<b>Introduction</b>	<b>6</b>
<b>2</b>	<b>Transition metal dichalcogenides and WS<sub>2</sub></b>	<b>8</b>
<b>3</b>	<b>Fundamentals of EELS</b>	<b>12</b>
3.1	EEL spectra . . . . .	13
3.2	Energy resolution . . . . .	15
3.3	ZLP subtraction . . . . .	17
<b>4</b>	<b>Fundamentals of neural networks</b>	<b>20</b>
<b>5</b>	<b>Neural network determination of the ZLP</b>	<b>24</b>
5.1	ZLP parametrisation . . . . .	24
5.2	Uncertainty propagation . . . . .	26
5.3	Training strategy . . . . .	29
<b>6</b>	<b>Results I. Vacuum spectra</b>	<b>35</b>
6.1	Training initialization . . . . .	35
6.2	Fit quality . . . . .	38
6.3	Dependence on the electron energy loss . . . . .	39
6.4	Dependence on beam energy and exposure time . . . . .	42
6.5	Stability and reliability checks . . . . .	43
<b>7</b>	<b>Results II. Sample spectra</b>	<b>47</b>
7.1	Training dataset . . . . .	47
7.2	Subtraction procedure . . . . .	49
7.3	Bandgap analysis of sample A . . . . .	54
7.4	Mapping excitonic transitions in sample B . . . . .	57
<b>8</b>	<b>Summary and outlook</b>	<b>60</b>
<b>A</b>	<b>Installation and usage of EELSfitter</b>	<b>63</b>

# 1 Introduction

The appreciation for the family of two-dimensional (2D) materials has grown rapidly since the first isolation of graphene [1]. The properties of these two-dimensional materials are usually very different from their 3D counterparts, offering functionalities for novel nanodevices that are not accessible from other heterostructures. The combination of optically active semiconducting layers for light-emitting devices, the implementation of indirect-to-direct bandgap transition materials for flexible electronics, the effect of chemical compositions on many-body instabilities such as superconductivity [2]; these are just a few examples of the relevance to exploit the properties of these 2D materials. However, realizing the full potential of any materials system requires knowing the precise electronic, structural and chemical information at high resolution.

Thanks to recent instrumentation breakthroughs in electron microscopy, such as electron monochromators [3, 4] and aberration correctors [5], it becomes possible to map these properties with unexampled spatial and spectral resolution. Specifically by means of electron energy loss spectroscopy (EELS), it becomes possible to study the local electronic properties of nanomaterials down to the atomic scale [6], and this way to explore various important phenomena from the characterisation of bulk and surface plasmons [7, 8], excitons [9], phonons [10], and inter- and intra-band transitions [11], to the determination of the bandgap energy and the band structure [12].

Particularly important information about the material's characteristics can be extracted from studying the low-loss region of EEL spectra, defined by electrons that have lost less than a few eV ( $\Delta E \lesssim 5$  eV) following their inelastic interactions with the sample. However, an omnipresent feature called the zero-loss peak (ZLP) dominates the low-loss region of the spectra. This narrow, high intensity peak is centered at energy losses of  $\Delta E \simeq 0$ , is often asymmetric, and its tails extend significantly beyond the FWHM. This peak results from the fact that the majority of the incident electron beam will traverse the electron-penetrable sample either without interactions or scattering only elastically with the sample's crystalline lattice, therefore losing little to no energy and ending up in the ZLP. Since in the low-loss region, the contribution from the ZLP tail overwhelms those from the inelastic interactions between the incident electrons and the specimen, relevant signals of low-loss phenomena such as excitons, phonons, and intra-band transitions risk being drowned in the ZLP tail [13]. An accurate removal of the ZLP contribution is thus crucial in order to efficiently identify and study the features of the low-loss region in EEL spectra.

Several approaches to ZLP subtraction have been put forward in literature [9, 12, 14–18]. These are often based on specific model assumptions about the ZLP properties, specifically concerning its functional dependence on the electron energy loss  $\Delta E$ , from Lorentzian [16] and power laws [9] to more general multiple-parameter functions [17]. Another approach is based on mirroring the  $\Delta E < 0$  region of the spectra, assuming that the  $\Delta E > 0$  region is fully symmetric [18]. More recent studies use integrated software applications for background subtraction methods [19–22].

These subtraction methods are however affected by three main limitations. Firstly, they rely on specific model assumptions *e.g.* with the choice of a specific fit function, introducing a methodological bias whose size is difficult to quantify. Secondly, they lack an estimate of the associated uncertainties, which in turn affects the reliability of any physical interpretations of the low-loss region such as band gap extraction. Thirdly, methodolog-

ical choices such as fitting ranges introduce a significant degree of arbitrariness to the procedure.

In this work we bypass these limitations by developing a model-independent strategy that allows for a multidimensional determination of the ZLP with a faithful uncertainty estimate. Our approach is based on machine learning (ML) techniques developed in high-energy physics to study quark and gluon substructure of protons particle collisions [23–26]. This technique is based on the Monte Carlo replica method to construct a probability distribution in the space of the experimental data (here the ZLP) and to use artificial neural networks as unbiased interpolators to parametrise the ZLP. The result is a prediction of the ZLP intensity based on its input variables, without the need to make specific model assumptions or approximations, which can be used to subtract its contribution to EEL spectra while propagating the associated uncertainties. Furthermore, we can extrapolate this ZLP parametrisation to other TEM operating conditions beyond those included in the training dataset.

This work is divided into two main parts. In the first, we construct a machine learning model that is able to predict the ZLP intensity for an arbitrary number of input variables corresponding to different operating settings of the TEM, *e.g.* exposure time and beam energy. We demonstrate how the model successfully describes the input spectra and we assess its extrapolation for other operating conditions that were not used for training. Furthermore, we check the stability of the predictions and the reliability of the error estimate with respect to the neural network parametrisation.

In the second part, we construct a one-dimensional model of the ZLP as a function of the energy loss from spectra acquired on tungsten disulfide ( $\text{WS}_2$ ) nanostructures [27]. The resulting subtracted spectra are used to determine the value and type of the  $\text{WS}_2$  bandgap and its dependence on the underlying crystalline structures, and to demonstrate how one can exploit the ZLP-subtracted results to characterise features arising in the very-low-loss region.

The outline of this work is as follows. In Sects. 2 and 3 we discuss the intriguing class of transition metal dichalcogenide (TMD) materials, with emphasis on  $\text{WS}_2$ , and we review the main features of the EELS technique. Sect. 4 contains the fundamentals of neural networks and the principles of supervised machine learning. In Sect. 5 we describe our machine learning methodology for the ZLP parametrisation. Sects. 6 and 7 contain our results for the ZLP parametrisation for spectra acquired in vacuum and in samples respectively, which in the latter case allows us to study the local band structure properties of the  $\text{WS}_2$  nanoflowers. Finally in Sect. 8 we summarise and outline possible future developments. Our results have been obtained with an open-source PYTHON code, `EELSFitter`, presented in App. A together with some installation and usage instructions.

## 2 Transition metal dichalcogenides and WS<sub>2</sub>

In this work we will apply our machine learning-based method for describing the ZLP to a novel class of tungsten disulfide (WS<sub>2</sub>) nanostructures [27]. WS<sub>2</sub> is a transition metal dichalcogenide (TMD) material, which belongs to a large family of materials known as two-dimensional (2D) materials or Van der Waals materials. In order to interpret the obtained EEL spectra later in this work, we first need to understand the most important characteristics of this class of materials.

The appreciation for the family of two-dimensional (2D) materials has grown rapidly since the first isolation of graphene in 2004 [1]. Since then, the family of one-layer-thick crystals has grown with the inclusion of metals, semi-conductors, and insulators. These materials are named two-dimensional to emphasize their extraordinary thinness: TMDs are characterised by the remarkable property of being fully functional down to a single atomic layer. The properties of these materials are usually very different from their 3D counterparts and offer great flexibility for tuning their electronic properties on the nanoscale.

Interestingly, numerous possibilities appear when several 2D crystals are combined in one vertical stacking, allowing for a much greater number of combinations than traditional growth methods. The nature of the intralayer bonds is mostly covalent, whereas the stacking layers are held together by weak van der Waals forces, which allows the crystal to easily cleave along the layer surface. Such stackings behave significantly different from traditional 3D heterostructures, because each layer on itself act as both the interface and the bulk material. This has great influence on the charge displacements: within each layer, charge transfers are reduced dramatically, however the mobility can be very large between subsequent layers, which offers interesting possibilities for engineering the band structure [2]. The relative alignment of neighbouring crystals is therefore of great influence on the physics that can be observed in such crystals.

Over the past few years the exploration of these 2D layered materials has developed rapidly. In particular, significant attention has been going to transition metal dichalcogenides, atomically thin semiconductors of the type  $MX_2$ , here M is a transition metal atom (such as Mo or W) and X is a chalcogen atom (such as S, Se, or Te). All TMDs have a hexagonal structure, with each characteristic monolayer comprising one layer of M atoms that is sandwiched between two layers of X atoms. As depicted in Fig. 2.1, the two most common coordination phases of the monolayers are octahedral and trigonal prismatic, which refers to the coordination of the transition metal atom [28]. The electronic and magnetic properties of TMDs strongly depends on this coordination, giving rise to a variety of possibilities [29]. As each individual layer can have any of the two coordinations, multi-layered TMDs can have a large variety of stacking types (polytypes), of which the most commonly found are defined as 1T, 2H and 3R. In this notation, the digit indicates the number of layers in the unit cell and the letter stands for trigonal, hexagonal and rhombohedral respectively.

Most of the remarkable electronic and optical properties of TMDs can be traced back to the underlying periodic arrangements of their layers. For example, the 1T form displays metallic behaviour, while both 2H and 3R polytypes are semiconducting. While nanostructures built upon 2H or 3R crystalline phases have been routinely studied, knowledge about those based on mixed 2H/3R polytypes is far more limited [27].

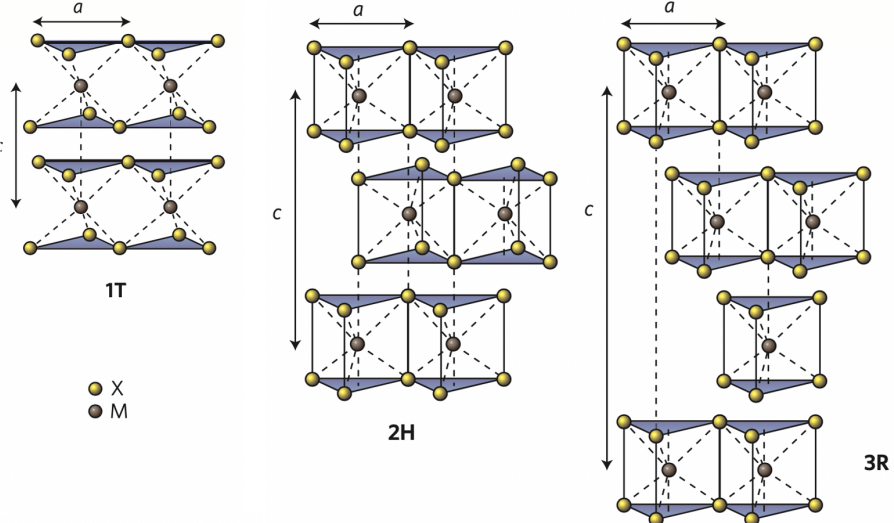


**Figure 2.1.** The most common coordinations and polytypes of TMD unit cells. Stacking single layers with the octahedral coordination yields a tetragonal symmetry (1T). The prismatic coordination can yield different stacking symmetries: hexagonal (2H) and rhombohedral (3R). Retrieved from [30].

Apart from the dependence on the stacking sequence, the properties of this class of materials vary significantly with their thickness. For instance, MoS<sub>2</sub> exhibits an indirect bandgap in the bulk form which becomes direct at the monolayer level [31]. The indirect-to-direct bandgap transition is the main reason for the interest in the use of TMDs for flexible electronics: it emphasizes the importance of the mechanical properties of these materials. However, it tends to be much more difficult to uniformly deform 2D monolayers of a material compared to bulk samples, and therefore measuring on 2D systems can be challenging. TMDs are often combined with other 2D materials like graphene to make Van der Waals heterostructures, which need to be tuned in order to function as building blocks for many devices such as LEDs, solar cells, transistors, and photodetectors. This research field is still emerging and highly promising to have a big impact on future nanotechnology.

An example of a TMD exhibiting a pronounced dependence on its thickness is tungsten disulfide (WS<sub>2</sub>), with an indirect-to-direct bandgap transition when going from bulk to bilayer or monolayer form. The effects of this transition are manifested as enhanced photoluminescence in monolayer WS<sub>2</sub>, whereas only little emission is observed in the corresponding bulk form. WS<sub>2</sub> adopts a layered structure by stacking atomic layers of S-W-S in a sandwich-like configuration, with each monolayer of the trigonal prismatic type (Fig. 2.1). Although the interaction between adjacent layers is a weak Van der Waals force, the dependence of the interlayer interaction on the stacking order of WS<sub>2</sub> is significant. Further applications of this material include storage of hydrogen and lithium for batteries [32].

For this work, we have studied specific nanostructures of WS<sub>2</sub> called nanoflowers, which are presented in [27]. A low-magnification TEM image of the WS<sub>2</sub> nanoflowers is displayed in the left panel of Fig. 2.2. These structures are grown directly on top of a TEM substrate with holes in it. The right panel shows the magnification of a representative petal of a nanoflower, where the difference in contrast indicates terraces of varying thickness. Note that the black region corresponds to the vacuum, without substrate underneath. These WS<sub>2</sub> nanoflowers contain areas with different thicknesses,

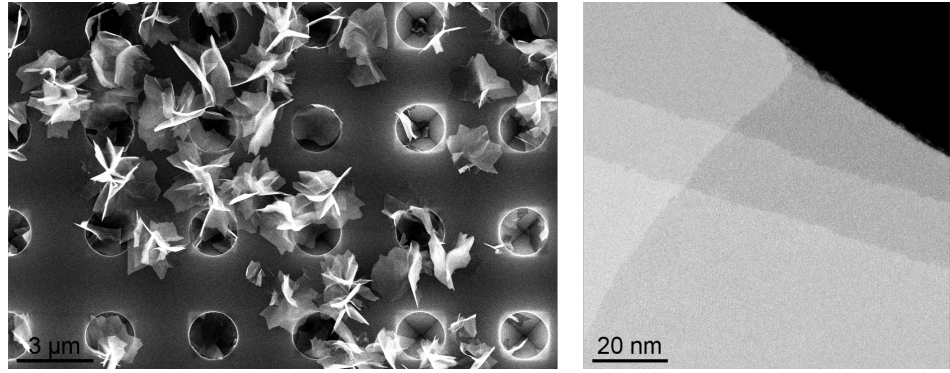


**Figure 2.2.** Left: low-magnification TEM image of WS<sub>2</sub> nanoflowers grown on top of a porous TEM substrate. Right: the magnification of a representative petal of a nanoflower, where the black region corresponds to the vacuum (no substrate) and the difference in contrast indicates terraces of varying thickness.

orientations and crystalline structures, therefore representing an ideal environment to investigate structural morphology in WS<sub>2</sub> with electronic properties at the nanoscale.

What makes these nanostructures even more interesting is that they exhibit a mixed form of 3R/2H polytypism, which is of importance for the interlayer interactions: it has been observed that the coexistence of multiple stacking types can complicate the characterization of the physical properties [33]. For example, one possible response of polytypism to electric fields is spontaneous electrical polarization, leading to modifications on the electronic band structure and correspondingly on the bandgap [34]. Tailoring the specific stacking sequences represents a powerful strategy to identify and design novel physical properties [27].

As mentioned before, one of the most interesting properties of TMDs that also occurs in WS<sub>2</sub> is the fact when the material is thinned down to a single monolayer, its indirect bandgap of  $E_{bg} \simeq 1.4$  eV switches to a direct bandgap of approximately  $E_{bg} \simeq 2.1$  eV. In general, it has been found that the type and magnitude of the bandgap of WS<sub>2</sub> depends quite sensitively on the crystalline structure and the number of layers that constitute the material. In Table 2.1 we collect representative results for the determination of the bandgap energy  $E_{bg}$  and its type in WS<sub>2</sub>, obtained by means of different experimental and theoretical techniques. For each reference we indicate separately the bulk results and those obtained at the monolayer level. We observe that for monolayers, the results for the measured value of  $E_{bg}$  are quite inconsistent, reflecting the challenges of its accurate determination.

Reference	Thickness	$E_{\text{bg}}$ (eV)	bandgap type	Technique
[35]	bulk	$1.4 \pm 0.07$	indirect	Gate-voltage dependence
[36]	ML	2.14	direct	Gate-voltage dependence
	bulk	1.40	indirect	
[37]	ML	$2.03 \pm 0.03$	direct	DFT
	bulk	$1.32 \pm 0.03$	indirect	
[38]	ML	$1.76 \pm 0.03$	direct	Absorption edge coefficient fitting
	bulk	1.35	indirect	
[39]	ML	$2.21 \pm 0.3$	direct	Bethe-Salpeter equation (BSE)

**Table 2.1.** Representative results for the determination of the bandgap energy  $E_{\text{bg}}$  and its type in WS<sub>2</sub>, obtained from a variety of experimental and theoretical techniques. For each reference we indicate separately the bulk results and those obtained for monolayers.

### 3 Fundamentals of EELS

Realizing the full potential of any material requires knowing its precise electronic, structural and chemical information at high spacial resolution. One way to achieve this is by means of electron energy loss spectroscopy (EELS). EELS is a method used in combination with transmission electron microscopy (TEM), which analyses the energy distribution of initially monoenergetic electrons after they have interacted with a specimen [15]. In this chapter, we present an introduction to the basics of EELS, followed by an overview of energy loss spectra and the limitations of the technique.

Electron energy loss spectroscopy was developed by James Hillier and R.F. Baker in the mid-1940s [40], but it was only becoming more widespread in research in the 1990s due to improvements in microscope instrumentation. Since modern instrumentation became widely available in laboratories in the mid-1990s, the scientific developments regarding electron microscopes grew rapidly. Especially since the introduction of modern aberration correctors and monochromated electron sources, energy resolutions of 100 meV or even higher could be achieved [41], which enabled measurements of single (columns of) atoms.

Transmission electron microscopy can provide structural information with excellent spatial resolution down to atomic dimensions. These compositional data can be supplemented by chemical information from the same specimen region, obtained using analytical techniques such as EELS. EELS instrumentation is typically incorporated into a scanning transmission electron microscope (STEM) or in a conventional TEM (c-TEM). These microscope types use high energy electrons, typically 60 - 300 keV, to interrogate the sample. The transmitted electrons are deflected through a uniform magnetic field of the order of 0.01 T, generated by an electromagnet with carefully shaped polepieces. Electrons that scattered inelastically will stray from the central trajectory, giving rise to a greater or lesser deflection angle, and are sorted and detected according to their energies. The existence of different kinetic energies thus results in a fringing field at the EELS detector.

A schematic illustration of a typical EELS setup is shown in the left panel of Fig. 3.1. The right panel of Fig. 3.1 shows a representative EELS spectrum in the low-loss region, recorded in one of the WS<sub>2</sub> nanostructures presented in [27], which will be further discussed later onwards.

Electron energy loss spectroscopy provides detailed information about the chemical components, bonding, and structure of the specimen. Thanks to recent progress in TEM instrumentation and data acquisition, the EELS technique benefits from a combination of both highly competitive energy (spectral) resolution and spatial resolution. Especially scanning transmission electron microscopy (STEM) equipped with a monochromator is extremely useful for high resolution imaging.

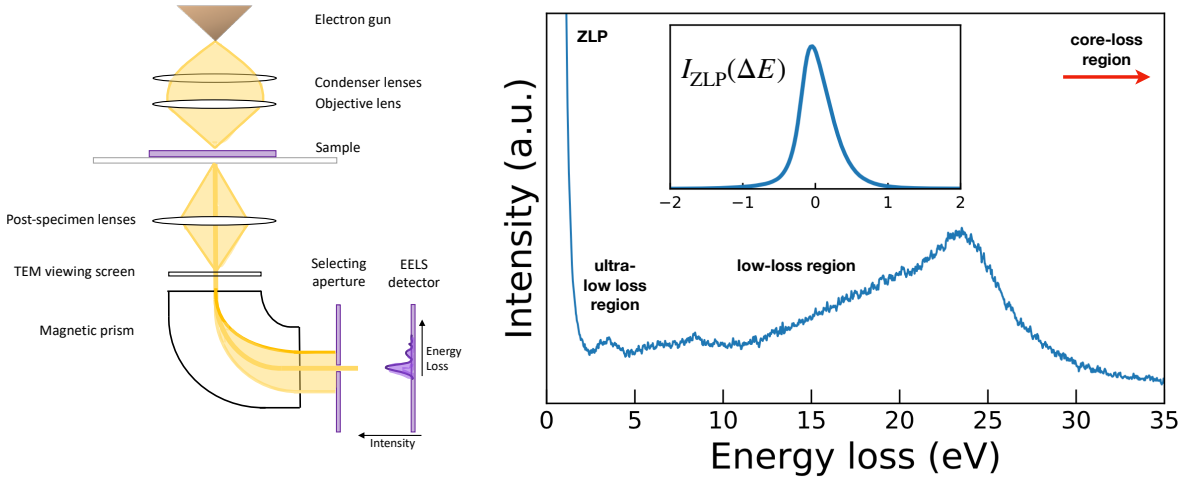


**Figure 3.1.** Left: graphical representation of a typical STEM-EELS setup. A magnetic prism is used to deflect the electron beam after crossing the sample so that the distribution of their energy losses  $\Delta E$  can be recorded. Right: a representative spectrum for  $\Delta E \leq 35$  eV acquired on a  $\text{WS}_2$  nanoflower [27] with the inset displaying the corresponding ZLP.

### 3.1 EEL spectra

If we are to understand how the features in electron energy loss spectra are produced, we must consider how the interaction of the incident electron with the sample contributes to the spectrum. Roughly speaking, EEL spectra can be divided into three main regions.

**Zero-loss region.** The first is the zero-loss region, which is centered around  $\Delta E = 0$  and contains the contributions from electrons that are transmitted without suffering measurable energy loss. Provided the thickness of the sample is small, the greatest part of the incident electron beam transfers through the sample elastically, implicating the energy exchange is less than the experimental energy resolution. A strong and narrow intensity peak around 0 eV loss can be observed called the zero-loss peak (ZLP) or elastic peak. The width of the ZLP, typically 0.2-2 eV, reflects the energy distribution of the electron source.

The inset in Fig 3.1 displays the ZLP, illustrating how nearby  $\Delta E \approx 0$  its magnitude is larger than the contribution from the inelastic interactions with the sample by several orders of magnitude. This can be explained by the fact that a nucleus is thousands of times more massive than an electron, and therefore the energy transfer involved in elastic scattering is usually negligible. The probability of elastic scattering for a single incident electron (per unit solid angle  $\Omega$ ) can to a first approximation be described by the differential cross section [15],

$$d\sigma_e/d\Omega = \frac{4Z^2/k_0^2 T}{(\theta^2 + \theta_0^2)^2} \quad (3.1)$$

where  $Z$  is the atomic number,  $k_0$  the electron wavenumber, and  $T$  is not the temperature but the incident electron energy.  $\theta$  is the scattering angle of the electron of interest, and  $\theta_0$  represents the angular width of the scattered beam.

**Low-loss region.** The second region is the low-loss region or valence region, defined for energy losses  $\Delta E \lesssim 50$  eV, which contains information about interactions between the fast incident electrons and the atoms in the specimen.

The two most fundamental types of collective electronic excitations in solids are plasmons and excitons. In EEL spectra recorded on rather thick specimens, the most prominently observed peaks are plasmon peaks. When an incident electron travels through the crystal lattice, the outer-shell electrons bound to the lattice atoms are left oscillating, creating a collective of electron excitation modes called a plasma resonance. This excitation can also be described by means of the creation of a pseudoparticle called a plasmon, whose energy depends on the plasmon frequency [42]. Plasmons contribute to the optical properties of metals and semiconductors. The higher the electron density, the higher the plasmon frequency and therefore the plasmon energy. Characteristic plasmon-loss peaks appear in the EEL spectra between 5 and 50 eV energy loss, and can be used to determine the thickness of the specimen, since a higher thickness leads to an increase in plasmon excitations.

Additionally, the passage of an incident electron can lead to the excitation of only a single outer-shell electron. For an insulator or semiconductor, this involves an inter-band transition across the energy bandgap, leaving a hole behind in the valence band. The bound state of the electron in the conduction band and electron hole in the valence band is called an exciton. Exciton features appear in the ultra-low-loss region of EEL spectra close to the ZLP, characterised by  $\Delta E \simeq$  few eV. Here, the contributions of the ZLP and those from the inelastic interactions with the sample are of the same order of magnitude, and they can be therefore difficult to distinguish [13].

When we are dealing with a metal, the higher state can be within the same energy band, corresponding to an intra-band transition. Peaks arising from intra-band transition appear very close to the ZLP, with typical energy losses below 500 meV.

For very thin specimens, the plasmon peaks largely disappear, leaving interband transitions as the main features in the low-loss regime [15]. This facilitates the study after the bandgap of the material. The bandgap refers to the energy difference between the top of the valence band and the bottom of the conduction band and the corresponding peak is expected to appear at energy losses where the joint density of states (JDOS) exhibits maxima. The nature of the bandgap can be either direct or indirect. For direct bandgap materials, electrons can be directly excited from valence to conduction band. However, for indirect bandgap materials, a photon or phonon is required to facilitate the transition. For this reason, direct bandgap materials tend to have stronger absorption properties.

It has been shown by Bruley and Brown [43] that for parabolic bands, the JDOS probed by the electrons can be described by

$$\rho(E) = \frac{V}{4\pi^2} \left( \frac{2m^*}{\hbar} \right)^{(3/2)} \alpha \sqrt{E - E_{bg}} \quad (3.2)$$

for a direct bandgap, where  $m^*$  is the mass of the electrons and holes in the valence and conduction band,  $E_{bg}$  is the bandgap energy and  $\alpha$  is the convergence angle of the electron beam. The nature (direct or indirect) and the bandgap energy can be deduced from the first few eV of the energy-loss function. From a fit of the bandgap onset to Eq. 3.2, the value of (1/2) for a direct bandgap switches to (3/2) for an indirect bandgap, as demonstrated in Fig. 3.2.

For materials with a large exciton binding energy, it might happen that the energy exchange is just barely enough to create an electron-hole pair, but too less to physically

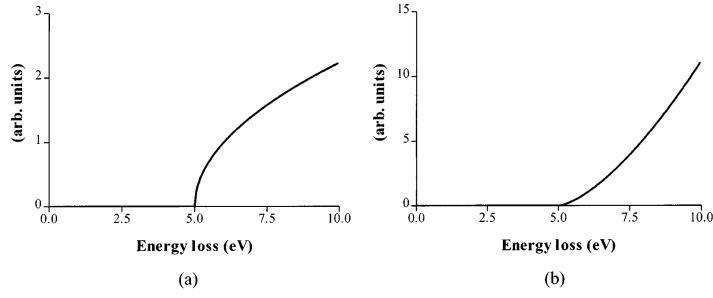


**Figure 3.2.** Schematic diagrams showing the contributions from the JDOS and matrix elements for (a) direct and (b) indirect transitions. From a fit of the bandgap onset to Eq. 3.2, the power of  $(1/2)$  for a direct bandgap switches to  $(3/2)$  for an indirect transition. Retrieved directly from [11].

separate the electron and hole. We then distinguish between the optical and the electrical bandgap, where the first is the threshold for the creation of an exciton, while the latter stands for the minimum energy required to create an electron-hole pair that is not bound together. The optical and electrical bandgap are separated by exactly the binding energy.

When we look at features in the EEL spectra for even lower energy losses,  $\Delta E \lesssim 100$  meV, vibrational modes can be revealed. These are the result of transmitted electrons that generate (and absorb) phonons while passing through the crystal. Phonon energies are of the order  $k_b T$  and corresponding energy losses are below 0.1 eV, which requires very high resolution spectroscopy to record it. Limited vibrational spectroscopy becomes possible in an electron microscope at around 30 meV energy resolution. Vibrational spectroscopy, a field that did not exist five years ago, includes vibrational mapping, analyzing the momentum dependence of vibrational states and determining the local temperature from the ratio of energy gains to losses [44], which can be achieved by studying features appearing at the left-hand side of the ZLP.

**Core-loss region.** The regime for  $\Delta E \gtrsim 50$  eV is the core-loss region, which provides compositional information on the elements that constitute the sample. In this regime, the spectrum shows characteristic features called ionisation edges, formed when an inner-shell electron absorbs enough energy from a beam electron to be excited to a state above the Fermi level. The thicker the sample, the more prominent the ionisation edges are since multiple scattering events are more common. In this work however, the focus will be on the low-loss region of EEL spectra, therefore we will not go into more detail regarding the core ionisation peaks.

## 3.2 Energy resolution

The energy resolution of an EEL spectrum is determined by several factors. Firstly, aberrations of the electron spectrometer cause blur of the incoming electron beam [4]. In general, the spectrometer dispersion becomes worse for higher electron losses, and therefore the resolution at ionization edges suffers more than close to the ZLP. Imaging quality can be improved by the implementation of an aberration corrector, to cancel the spherical aberration of the objective and condenser lenses. The energy resolution is then mainly determined by the angular distribution provided by the electron beam, usually expressed as the full width at half maximum (FWHM) of the ZLP. The peak width depends strongly

on the electron source. An electron microscope equipped with a cold field emission gun typically has an energy resolution of about 300-800 meV under normal operation conditions. While this width is small compared to the operating voltage of the STEM (usually between 60-300 keV), it sets a limit for the energy resolution of EELS and thereby hinders the ability to distinguish between peaks separated by less than this value. Furthermore, for low-loss phenomena such as excitons, excitation probabilities can be quite low and these signals can be lost in the tails of the ZLP.

The resolution can be drastically improved by implementation of a monochromator in the TEM. In monochromators, a small magnetic prism and energy-selecting slit are installed directly after the electron source. This setup essentially works as an energy filter: the incoming electron beam is first dispersed before going through a narrow slit, restricting the energy distribution of the incoming electrons. After compressing it back into the electron probe, the width of the electron beam and the tail intensity are greatly reduced. In a recent study [44], a monochromated zero-loss peak was obtained with a FWHM as small as 4.2 meV and, maybe even more importantly, the tail intensity at 20 meV loss has dropped below  $10^{-3}$  of its maximum, allowing features in the very low-loss region to be resolved. The improving energy resolution opens new possibilities for accurate measurements on the bandgap and the dielectric function.

Apart from the increase in resolution, another advantage of a monochromated electron beam is its symmetric energy distribution. This directly implies that asymmetries of absorption peaks in the spectrum can unambiguously be attributed to the response of the material [9]. The reduction of the energy spread of the incident electron beam often comes at the expense of the beam intensity.

In Fig 3.3, one can observe the effect of a monochromator on the zero-loss peaks of a Schottky field emission microscope in the work of [9]. Due to thermal broadening, the unfiltered Schottky field-emission source shows a broad tail at the high-energy side, *i.e.* at negative energy loss values. The tails of the monochromated beam are highly symmetrical and the energy dispersion (FWHM) is greatly reduced.

There is one more limitation to the EELS resolution that needs to be discussed, that is the contribution coming from multiple scattering. In the general case, but specifically for thicker samples, plural scattering of electrons is possible, introducing additional peaks at two (or three, four...) times the single scattering energy loss. Distinguishing the single scattering contributions from the multiply-scattered electrons is typically done by means of a deconvolution method [15]. Multiple scattering restricts elemental mapping to specimen thickness below the mean free path of scattered electrons, which usually corresponds to a thickness  $< 70$  nm [45].

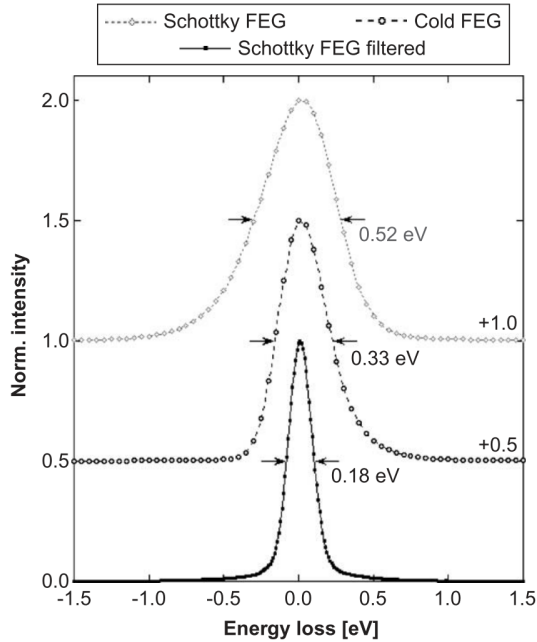


**Figure 3.3.** Comparison of the zero-loss peaks of an unfiltered Schottky field emission microscope (200 kV), a cold field-emission microscope (100 kV) and a monochromated electron beam with Schottky field-emission source (200 kV). The second ZLP shows a wider tail at the low-energy side and the tails of the monochromated beam are highly symmetrical. The FWHM indicated in each case provides a measure for the energy resolution. Retrieved directly from [9].

### 3.3 ZLP subtraction

The most important aspect complicating the study of the low-loss regime of EEL spectra is the observation of the zero-loss peak, a very intense and ubiquitous feature whose right-hand tail suppresses the low-loss features, which results in the loss of important information within the spectrum. Before analysing the low-loss region of EEL spectra, accurate removal of the ZLP is crucial. In the last several years different removal routines for the ZLP were introduced, as the increasing energy resolution of the instrumentation would allow for bandgap determination of the material.

The properties of the ZLP in monochromated EELS depend on the electron energy dispersion, the monochromator alignment, and the sample thickness [12,46]. The first two limitations are already present for a ZLP recorded in vacuum, but the third is associated to interactions with the sample, such as phonon excitations, exciton losses, and broadening at the surface of the sample. This implies that the separately recorded peak can be used for calibration purposes, but not to directly subtract the ZLP from spectra taken on specimens. Due to the obvious difference in shape between vacuum and in-sample recorded ZLPs, direct subtraction of the first on the latter would introduce an extra source of error.

For this reason, the most general suggestion is the subtraction of a fitted ZLP from the EEL spectrum. Representative examples include the subtraction of a fitted Lorentzian distribution [16], directly subtracting the mirrored left-hand side of the ZLP [18], the subtraction of a power-law fit [9], and the use of a more general multi-parameter function [17]. The fitted ZLPs and the corresponding subtracted spectra can be observed in Fig. 3.4.

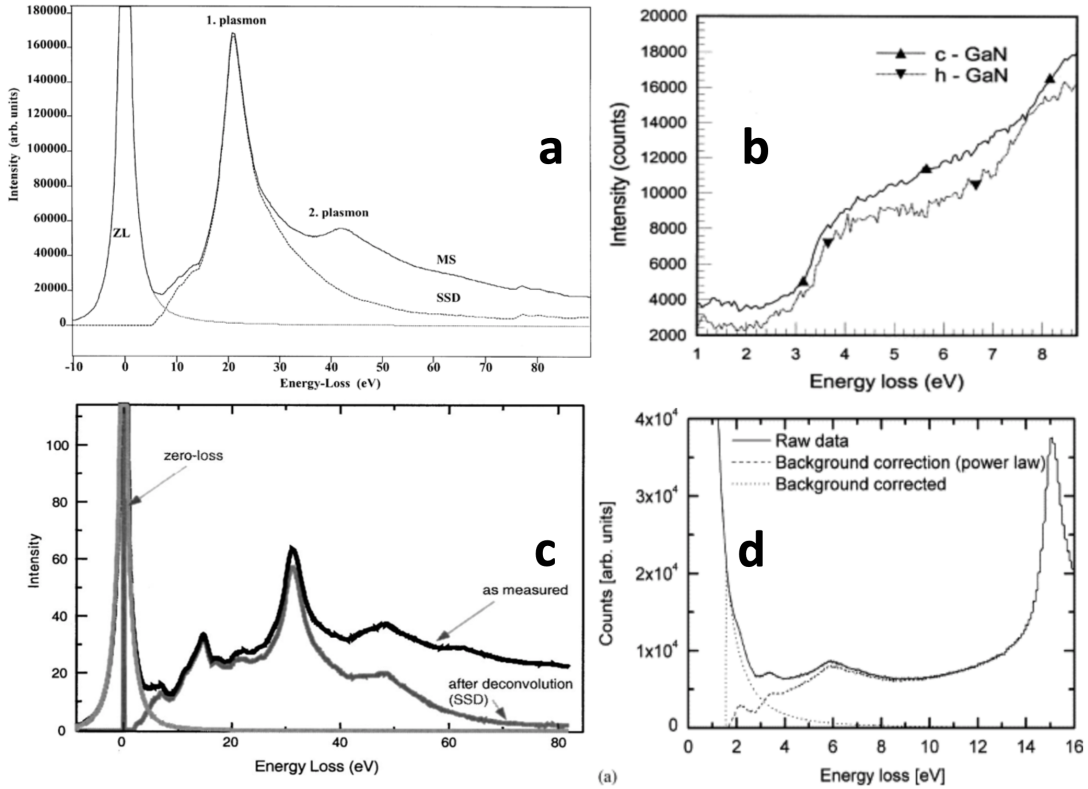


**Figure 3.4.** Comparison of the fitted zero-loss peaks and the corresponding ZLP-subtracted spectra by means of fitting an (a) Lorentzian distribution [16], (b) mirrored left-hand side [18], (c) power-law fit [9], (d) general multi-parameter function [17]. One can observe how all subtracted spectra lack any form of associated uncertainties.

These and several other attempts to model the ZLP distribution have had some success at describing the main intensity of the peak, but in the tails discrepancies can be as large as several tens of percent [47]. The standard method for background subtraction of the tails is to fit a power law to the tails, however this approach is not suitable in many circumstances [48–51]. Especially in the very-low-loss region, a simple functional fit completely removes all intensities belonging to losses within the bandgap energy. More recent studies use integrated software applications for background subtraction methods [19–22].

One common flaw of these subtraction methods is the fact that they are often based on specific model assumptions about the ZLP properties and thereby introduce a methodological bias whose size is difficult to quantify. This bias arises from assumptions made *e.g.* on its functional form, symmetry properties, or the fitting range that has been used, all introducing an arbitrariness to the procedure. Crucially, these subtraction methods lack an estimate of the associated uncertainties, which in turn affects the reliability of any physical interpretation of features that are observed in the ZLP-subtracted spectra.

Developing a model-independent strategy that allows for a determination of the ZLP with a faithful uncertainty estimate is highly coveted. With the knowledge that the magnitude and shape of the ZLP depend not only on the specific values of the electron energy loss  $\Delta E$ , but also on other operation parameters of the TEM such as the electron beam energy  $E_b$ , the exposure time  $t_{\text{exp}}$ , the aperture width and the potential use of a monochromator, one cannot measure the ZLP for a given operating condition, for instance a high beam voltage of  $E_b = 200$  keV, and expect to reproduce the ZLP distribution

associated to different conditions, such as a lower beam voltage of  $E_b = 60$  keV, without introducing model assumptions.

Since it is not possible to compute the dependence of the ZLP directly on  $\Delta E$  and the other operating conditions of the microscope, reliance on specific models appears to be unavoidable. Furthermore, even for identical operating conditions, the intensity of the ZLP will in general vary due to *e.g.* external perturbations such as electric or magnetic fields [14], the stability of the microscope and spectrometer electronics [52], the local environment (possibly exposed to mechanical, pressure and temperature fluctuations) and spectral aberrations [15]. Any model for the ZLP should thus account for this source of uncertainties.

## 4 Fundamentals of neural networks

One of the most successful machine learning techniques, artificial neural networks, is based on the idea of simulating the functioning of neuron connections of the human brain. This machine learning technique is trained in a fashion similar to human learning with the goal to process complex inputs and conclude correct outputs [53]. A neural network (NN) is defined by a (usually large) number of neurons interconnected with strength parameters called weights. A typical multilayer neural network architecture is schematically shown below in Fig. 4.1.

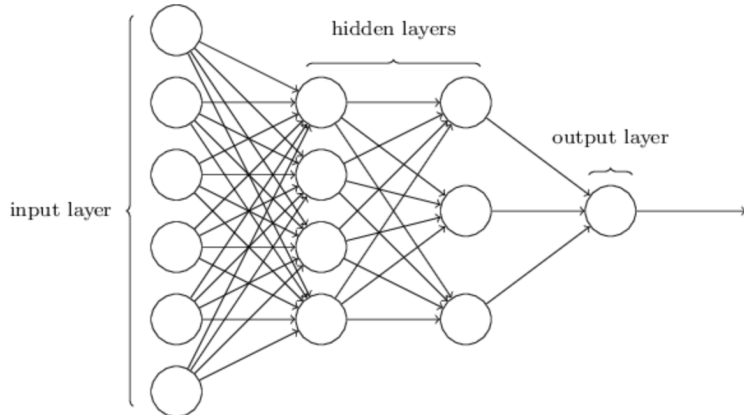


**Figure 4.1.** Schematic representation of a four-layer Neural Network with two hidden layers and one output neuron

Each neuron, represented in the above figure with a circle, is connected to a number of neurons in the previous layer. The far left neurons are the input neurons, they represent an input vector where each neuron holds one dimension of the vector, *e.g.* an energy loss bin in an EEL spectrum. The far right neurons are the output neurons and they can be either real-valued numbers or classification labels (1 or 0). For each neuron, its output is the result of an activation function to its inputs:

$$z = \sum_j w_j x_j + b, \quad (4.1)$$

where  $x_j$  are the outputs of the preceding neurons,  $w_j$  are the corresponding weights and  $b$  is the bias (offset) of the neuron. It is the latter two that will be optimized by training.

A nonlinear activation function  $f(z)$  is applied to come to the output value for each neuron; this procedure is called forward propagation. Through the use of these nonlinear functions, the neural network graph resembles an efficient nonlinear regression model. Typical examples for  $f(z)$  are the Rectified Linear Unit (ReLU) and sigmoid function, as depicted in Fig. 4.2. Note that these are two often-used, but not the only possible activation functions. The choice of nonlinear activation function influences computational and training properties of the neural nets [54]. For example, choice for the ReLU function ensures absolute positivity.

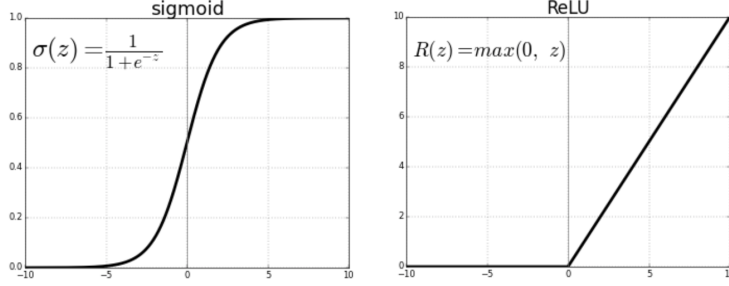


**Figure 4.2.** Sigmoid (left) and ReLU (right) activation functions. Both approach 0 as  $z \rightarrow -\infty$  but note the different behaviour for  $z \gg 0$ .

The input vector is passed through each layer of the neural network and is transformed by the nonlinear operations until it arrives at the output layer. For a certain set of inputs  $x_0$  and a collection of weights and biases  $(w_{jk}^l, b_j^l)$ , where  $w_{jk}^l$  is the connection between the  $j$ -th neuron in the  $l$ -th layer and the  $k$ -th neuron in the  $(l+1)$ -th layer,  $b_j^l$  being the corresponding bias, the neural network gives an output  $y$  that can be compared to the desired (target) output  $\hat{y}$ . A cost function  $C(y, \hat{y})$  is used to quantify how far we are from our desired output. It is for this reason that this type of machine learning is called supervised learning: after each iteration, under supervision of the correct output, the model parameters are adjusted. This is in contrast to unsupervised learning, where one only has a collection of data, and is looking to find structure without knowing the desired outcome.

Training the algorithm is done by minimizing the cost function with respect to all tunable parameters  $(w_{jk}^l, b_j^l)$  of the system. This minimization is done by means of the gradient descent method, a first-order optimization algorithm for finding a local minimum of a differentiable function, in this case the cost function  $C$ . To find the local minimum, after each iteration the weights and biases are adjusted a bit proportional to the negative of the gradient of the cost function at the current point.

To make this minimization computationally tractable, the so-called back-propagation algorithm is used [55], allowing us to approximate the derivative of the cost function by averaging over the training set. All together, training the network relies on the following four fundamental equations:

$$\begin{aligned}\delta_j^L &= \frac{\partial C}{\partial a_j^L} f'(z_j^L), \\ \delta^l &= (w^{l+1} \delta^{l+1}) \odot f'(z^l), \\ \frac{\partial C}{\partial b_j^l} &= \delta_j^l, \\ \frac{\partial C}{\partial w_{jk}^l} &= a_k^{l-1} \delta_j^l.\end{aligned}\tag{4.2}$$

Here,  $\delta_j^l$  is the error and  $a_j^l$  is the output of neuron  $j$  in layer  $l$ ;  $C$  is the cost function;  $b$  is the bias and  $w$  is the weight of each neuron. It is the error  $\delta_j^L$  in the first line that represents the total cost of the network. The second line presents the backpropagation: from layer  $(l+1)$ , the error is propagated back through the network until the very first layer. The last two equations evaluate the gradient of the model parameters with the gradient of the cost function.

With this info one can update the model parameters by

$$\begin{aligned} b^{l+1} &= b^l - \eta \frac{\partial C}{\partial b^l} \\ w^{l+1} &= w^l - \eta \frac{\partial C}{\partial w^l} \end{aligned} \quad (4.3)$$

where  $\eta$  is the pre-defined learning rate, a measure for the size of the step taken with each iteration. From Eqns. (4.2), one can see that the choice of nonlinear activation function  $f(z)$  affects the learning of the network. This could already be deduced from the shape of the functions in Fig. 4.2: since  $\sigma(z)$  saturates for large inputs  $z \gg 0$ ,  $d\sigma/dz \rightarrow 0$  and the network loses sensitivity [54].

We use the definition *epoch* for each time that the entire set of training data is passed forward once through the neural network and the network has backpropagated the error and updated all of its parameters accordingly. The network needs much more than just one epoch to optimize by means of gradient descent, as this is an iterative process.

After each epoch, the performance of the network is evaluated by calculating the error ( $\delta_j^L$ ) on the training data and the weights and biases are adjusted accordingly. As the number of epochs increases, the network parameters are adjusted repeatedly and where the network was first underfitting the inputs at the beginning, at a certain moment it goes to optimal fitting, before it enters the overfitting regime.

Several methods can be applied to determine the optimal stopping point of the network, that is, to find the moment at which the network is neither under-, nor overfitting the training data. One of such is splitting the total set of experimental data into two sets: the training dataset is the one we use to train the model, usually 80% of the total set. The other 20% is what we call the validation set and it is used to provide an unbiased evaluation of the model fit on the training set. This split ratio is common for models with a moderate number of hyperparameters: increasing the size or increasing the tunability of the model usually goes with increasing the share of the validation set. The validation subset is left out of the training set on purpose and the model cannot learn on these inputs. After each epoch, the total performance of the system can be validated by feeding this subset to the network and calculating the total corresponding error.

Tracing the cost function on both the training and the validation set gives insight on whether the network is overfitting the training data. First, both the training and validation error will decrease, but at a certain point the network will start overfitting and the validation error slowly starts to increase. The optimal stopping point is defined as the global minimum of the error of the validation sample, computed over a large fixed number of iterations. A typical progress of the training and validation error over the course of the optimization can be observed in Fig. 4.3.

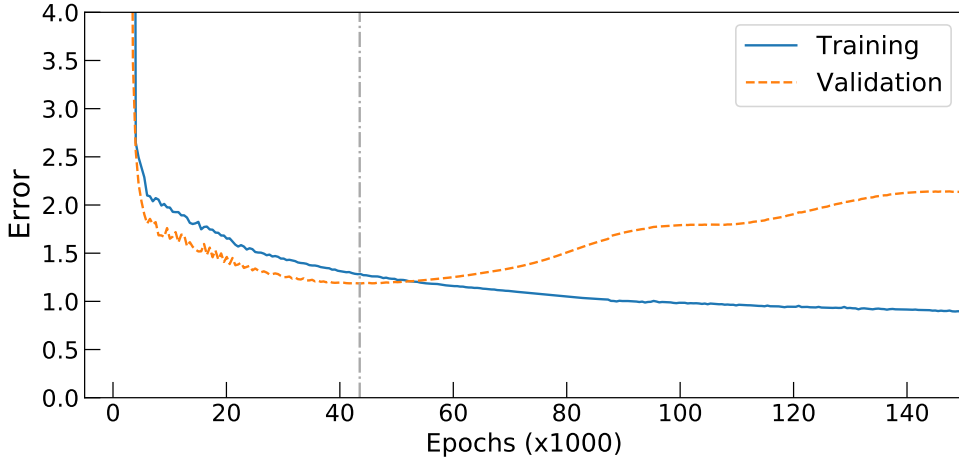


**Figure 4.3.** Progress of both the training and validation error over one training session as a function of the number of epochs. The optimal stopping point is where the validation error is at its absolute minimum, here after 43,500 epochs.

Once the optimal network parameters have been determined and stored, the network can be used to make predictions on any set of inputs.

### Computational methods

In this work, the neural network training was performed in Python using Google’s machine learning library Tensorflow. This open source library includes a great deal of neural network models and algorithms and makes them accessible through a convenient front-end programming interface. Tensorflow applications can be run on almost any target: both CPU and GPU, on-device and in the cloud. The most-mentioned advantage is Tensorflow’s transparency and eager executions, allowing for immediate model iteration and easy debugging.

Creating a Tensorflow machine learning model typically involves the following stages:

- Load and preprocess data: construct a dataset from data in memory, or use a readily available training dataset from the built-in library. For example, for image recognition, one training element corresponds to an image and its label. The image pixels need to be converted to a real-valued tensor in order to function as training inputs.
- Build, train and reuse models: initialize the model architecture and start training. Tensorflow makes it possible to commonly evaluate, save and restore models, and it is possible to speed up the training by leveraging multiple GPUs in parallel.
- Deploy: obtain and interpret predictions, accelerate training, optimize performance, and visualize output.

Setting up and fine-tuning the neural network model can be a delicate process that is conditional to the specific task or goal to be fulfilled.

## 5 Neural network determination of the ZLP

In this section we present our strategy to parametrise, predict, and subtract the zero-loss peak by means of machine learning. Neural networks benefit from the ability to parametrise multidimensional input data with nonlinear relationships. In fact, a neural network with fixed architecture and loss function would just be a parametric nonlinear regression model. Even with a single hidden layer, a neural network can reproduce arbitrary functions provided that the number of neurons is chosen large enough. We use this in our advantage for the determination of the functional dependence of the ZLP intensity.

Recently, several applications of machine learning to transmission electron microscopy analyses in the context of material science have been presented, see *e.g.* [56–62]. For the readout of EEL spectra specifically, machine learning has been put forward for the prediction of spectral features in the core-loss regime [63]. As mentioned in the introduction, the strategy presented in this section is inspired by the NNPDF method [64] which was originally developed in the context of high-energy physics for studies of the quark and gluon substructure of the proton [65].

To the best of our knowledge, this is the first time that neural networks are implemented as background-removal interpolators and combined with Monte Carlo sampling to construct an estimate of the model uncertainties.

The ultimate goal is to create a model that is able to predict the contribution  $I_{\text{ZLP}}$  in the total intensity profile of any EEL spectrum recorded over a specimen, and subsequently to subtract this distribution from the spectrum to isolate the inelastic scattering contributions. In order to do so, we first need to develop a model that is able to predict the general shape of the zero-loss peak as a function of its input parameters. We use zero-loss peaks that have been recorded in vacuum to function as a baseline to create this generic, multidimensional model. In this regard we also explain the Monte Carlo replica method, which is used to estimate and propagate the uncertainties from the input data to the model predictions. After this we move on to the training strategy on sample spectra: we explain how the method is modified to use it on spectra recorded over WS<sub>2</sub> specimens and how one can select the hyper-parameters that appear in the model.

### 5.1 ZLP parametrisation

Generally stated, the intensity profile of any EEL spectrum is the sum of two separate contributions, which can be described as

$$I_{\text{EEL}}(\Delta E) = I_{\text{ZLP}}(\Delta E) + I_{\text{inel}}(\Delta E), \quad (5.1)$$

where  $\Delta E$  is the measured electron energy loss;  $I_{\text{ZLP}}$  is the zero-loss distribution arising both from instrumental origin and from elastic interactions; and  $I_{\text{inel}}(\Delta E)$  contains the contributions from the electrons that have undergone inelastic scattering with the specimen. It is the latter contribution that we are particularly interested in, but in order to get hold of it we need to disentangle it from the zero-loss contribution, which makes it desirable to rewrite Eq. (5.1) into

$$I_{\text{inel}}(\Delta E) = I_{\text{EEL}}(\Delta E) - I_{\text{ZLP}}(\Delta E). \quad (5.2)$$

There are two regions in the energy loss spectrum for which one can straightforwardly separate the two contributions. The first is for sufficiently high energy losses, where  $I_{\text{ZLP}}$

vanishes and  $I_{\text{EEL}} \rightarrow I_{\text{inel}}$ . Secondly, in the region close to zero, all emission can be associated to the ZLP such that  $I_{\text{EEL}} \rightarrow I_{\text{ZLP}}$ . It is the region in between that is of particular interest, the very-low-loss region where  $I_{\text{ZLP}}$  and  $I_{\text{inel}}$  become of comparable order of magnitude.

Our goal is to construct a parametrisation of  $I_{\text{ZLP}}$  based on artificial neural networks, which allows us to extract the relevant inelastic contribution by subtracting the contribution of the ZLP from the total EEL spectra. This turns Eq. (5.2) into

$$I_{\text{inel}}(\Delta E) \simeq I_{\text{EEL}}(\Delta E) - I_{\text{ZLP}}^{(\text{mod})}(\Delta E). \quad (5.3)$$

Isolating  $I_{\text{inel}}$  from the total spectrum makes it possible to exploit the physical information contained in the low-loss region. In this respect, we aim to estimate and propagate all the relevant sources of uncertainty associated both to the experimental input and introduced by the methodology. This helps us to verify our results and to separate lucky findings from real insights.

As discussed in Sect. 3, the ZLP depends both on the value of the electron energy loss  $\Delta E$  as well as on the operating conditions of the microscope, such as the electron beam energy  $E_b$  and the exposure time  $t_{\text{exp}}$ . However, also other conditions could be taken into account, *i.e.* aperture width, aberration correction, convergence and collector angles, and so on. Therefore, we want to construct a multidimensional model which can theoretically take any number of relevant variables as input - ideally as many as possible - in order to reproduce the predicted zero-loss peak. This means that in general Eq. (5.3) can be rewritten as

$$I_{\text{inel}}(\Delta E) = I_{\text{EEL}}(\Delta E, E_b, t_{\text{exp}}, \dots) - I_{\text{ZLP}}^{(\text{mod})}(\Delta E, E_b, t_{\text{exp}}, \dots), \quad (5.4)$$

where the modeled ZLP contribution  $I_{\text{ZLP}}^{(\text{mod})}$  is the output of the artificial neural networks, which in turn corresponds to the output of the single output neuron in the very last layer of the NN. It is also important to note that the subtracted spectrum  $I_{\text{inel}}(\Delta E)$  should depend only on the measured energy loss, but not on the microscope parameters.

The  $n_I$  inputs are the variables  $\{\Delta E, E_b, t_{\text{exp}}, \dots\}$  that represent the relevant information about the operating conditions during the recording of the spectra. For this study specifically, we have used spectra recorded under the known conditions for the energy loss  $\Delta E$ , exposure time  $t_{\text{exp}}$  and electron beam energy  $E_b$ , but this set of inputs could potentially be extended by including extra variables. The NN is then trained on these  $n_I$  inputs, using the known corresponding ZLP intensities as training outcomes.

The number of hidden layers and neurons that is optimal is very task dependent and should therefore be decided empirically; there is no general rule of thumb. We have chosen to use an  $n_I$ -10-15-5-1 architecture with three hidden layers, which corresponds to a total number of 289 (271) free parameters for  $n_I = 3$  ( $n_I = 1$ ) to be optimised. However, we have verified that results are fairly independent of this exact choice; we will elaborate on this later onwards.

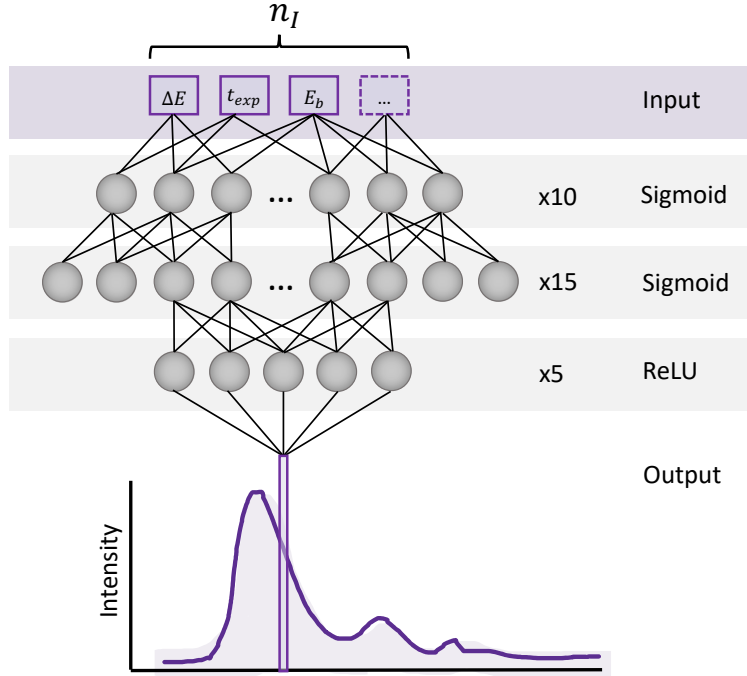


**Figure 5.1.** Schematic representation of our neural network parametrisation of the ZLP. The input is an  $n_I$ -dimensional array containing  $\Delta E$  and other operation variables of the microscope such as  $E_b$  and  $t_{\text{exp}}$ . The output is the predicted value of the intensity of the zero-loss peak distribution associated to those specific input variables. The architecture is chosen to be  $n_I$ -10-15-5-1, with sigmoid activation functions in all layers except for a ReLU in the output neuron.

A schematic representation of this model is displayed in Fig. 5.1. The  $n_I$  inputs are passed through the network and the output is the value of the intensity of the ZLP distribution associated to those inputs. We use a sigmoid activation function for the three hidden layers and a ReLU for the final one. The choice of ReLU for the final layer guarantees that our model for the ZLP is positive-definite, as required by general physical considerations: the intensity count can never be smaller than zero.

We have adopted a redundant architecture to ensure that the ZLP parametrisation is sufficiently flexible, which means that this way we guarantee that the network can over-fit on the training inputs. However, the final results should be evaluated before the network starts overfitting, as described in Sect. 4. This means that we need to define a suitable regularisation strategy, which will be explained later onwards in Sect. 5.3.

## 5.2 Uncertainty propagation

We discussed in Sect. 3 how even for EEL spectra taken at identical operating conditions of the microscope, in general the resulting ZLP intensity profiles will be different. Also, the input data can be described by a large number of different neural network configurations, each with a different functional form of  $I_{\text{ZLP}}^{(\text{mod})}$  but representing the data equally well. The Monte Carlo replica method can be used to estimate these two sources of uncertainties, introduced by the experimental data and the methodology, and to propagate them to physical predictions. The basic idea is twofold: first, it is useful to represent problems with a possibility of non-gaussian errors through the use of their central values and uncertainties, which are obtained from a Monte Carlo sample as their averages and standard deviations. Second, when a problem requires a reconstruction of discrete sampling without making assumptions on its functional form, neural networks are useful to

work as unbiased interpolators. It is the combination of both techniques that explains the use of neural networks to separate a smooth signal from background signals, while the MC samples handles the fluctuations within the data.

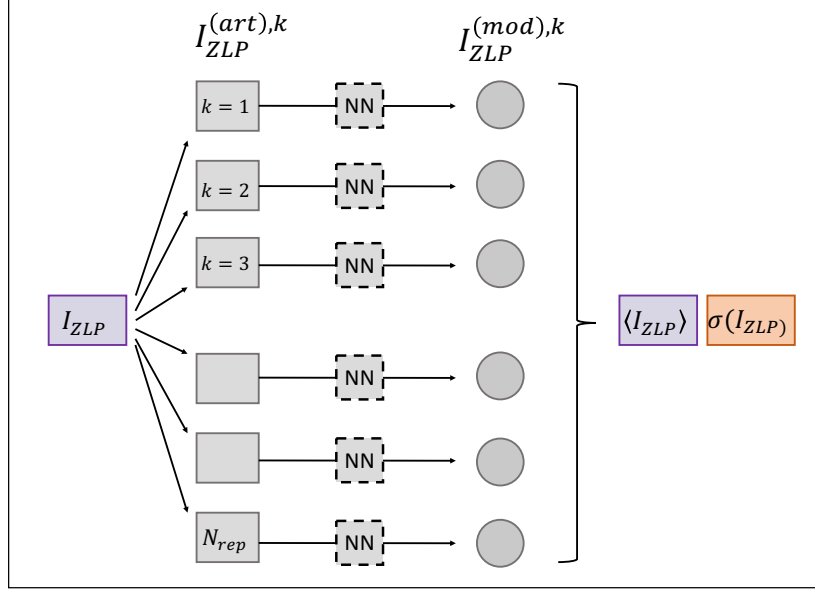


**Figure 5.2.** Representation of the Monte Carlo replica strategy. From the original set of training data, an ensemble of replicas is created from the experimental central values and uncertainties. On each replica, an individual neural network is trained and a ZLP parametrisation is obtained. The total set of predictions is then used to calculate physical observables from the corresponding central values and uncertainties.

The MC strategy is schematically summarized in figure 5.2 and it involves two stages. In the first, we generate an ensemble of replicas of the original training set using the experimental central values and errors. Then, each replica is used to train an individual neural network, which thereby outputs a prediction of the ZLP. Any physical observables can be calculated over the set of computed ZLP distributions.

If we assume that we have  $n_{\text{dat}}$  independent measurements of the ZLP intensity, our training dataset contains  $n_{\text{dat}}$  data points, all with different combinations of input parameters. The collective of inputs is given as  $\{\text{input}_i\}$  and the corresponding ZLP intensity depends on this set of inputs:

$$I_{\text{ZLP},i}^{(\text{exp})}(\{\text{input}_i\}) = I_{\text{ZLP},i}^{(\text{exp})}(\Delta E_i, E_{b,i}, t_{\text{exp},i}, \dots), \quad i = 1, \dots, n_{\text{dat}}. \quad (5.5)$$

The Monte Carlo method is based on the generation of a large number  $N_{\text{rep}}$  of Monte Carlo replicas of these original data points, where we use the central values from the input measurements. The strategy of the generation of Monte Carlo replicas goes as follows: we create for each original data point ( $I_{\text{ZLP},i}^{(\text{exp})}$ ) an ensemble of artificial pseudo points (replicas):

$$I_{\text{ZLP},i}^{(\text{art})(k)} = I_{\text{ZLP},i}^{(\text{exp})} + r_i^{(\text{stat},k)} \sigma_i^{(\text{stat})} + \sum_{j=1}^{n_{\text{sys}}} r_{i,j}^{(\text{sys},k)} \sigma_{i,j}^{(\text{sys})}, \quad \forall i, \quad k = 1, \dots, N_{\text{rep}}. \quad (5.6)$$

where  $\sigma_i^{(\text{stat})}$  and  $\sigma_{i,j}^{(\text{sys})}$  express the statistical and the systematic uncertainties. The latter denotes the correlation between the uncertainties in different points.  $\{r_i^{(k)}\}$  are gaussian random numbers, used to generate the fluctuations of the pseudo data around the central values of the experimental data. In the end, each  $k$ -th replica contains exactly as many data points as the original set.

In our case we have no information on experimental correlations between the measurements and for this reason we assume that there is only one single source of uncorrelated systematic uncertainty. Should in the future correlations became available, it would be straightforward to extend our model to that case.

In other words, to each data point we associate an individual uncertainty and we discard covariances between datapoints, which means that we drop the last term in Eq. (5.6) and it reduces to

$$I_{\text{ZLP},i}^{(\text{art})(k)} = I_{\text{ZLP},i}^{(\text{exp})} + r_i^{(\text{stat},k)} \sigma_i^{(\text{stat})}, \quad k = 1, \dots, N_{\text{rep}}. \quad (5.7)$$

The statistical errors on the training data can be derived by means of what is called equal width discretization (EWD) and it works as follows. The input measurements will be composed in general on subsets of EEL spectra taken with identical operating conditions. For example, we have one specific set of  $N_{\text{sp}}$  spectra all recorded with the same exposure time and beam energy. Since the range of  $\Delta E$  over which the spectra have been recorded is usually not the same in each case, first of we uniformise a common binning in  $\Delta E$  with  $n_{\text{dat}}$  entries. Then we evaluate the total experimental uncertainty in one of these bins as

$$\sigma_i^{(\text{exp})} = \left( \frac{1}{N_{\text{sp}} - 1} \sum_{l=1}^{N_{\text{sp}}} \left( I_{\text{ZLP},i}^{(\text{exp}),l} - \left\langle I_{\text{ZLP},i}^{(\text{exp})} \right\rangle_{N_{\text{sp}}} \right)^2 \right)^{1/2}, \quad i = 1, \dots, n_{\text{dat}}, \quad (5.8)$$

that is,  $\sigma_i^{(\text{exp})}$  is the standard deviation in bin  $i$  calculated over the  $N_{\text{sp}}$  spectra. This uncertainty is separately evaluated for each set of microscope operation conditions for which data is available. A schematic representation of EWD can be observed in Fig. 5.3, where the number of bins is taken low on purpose for better visualization.

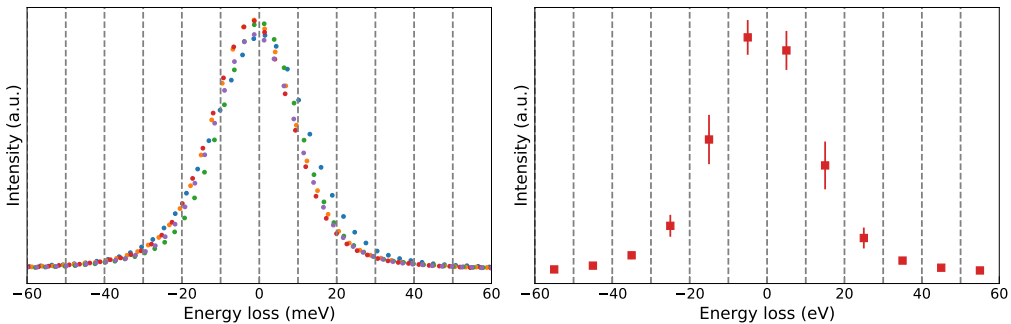


**Figure 5.3.** Schematic representation of equal width discretization (EWD), where the energy loss is divided into bins of equal width and the uncertainty in each of these bins is calculated by means of Eq. (5.8).

Now that each experimental data point has an associated uncertainty, we can generate the set of Monte Carlo replicas by means of Eq. (5.7). The value of the number of generated

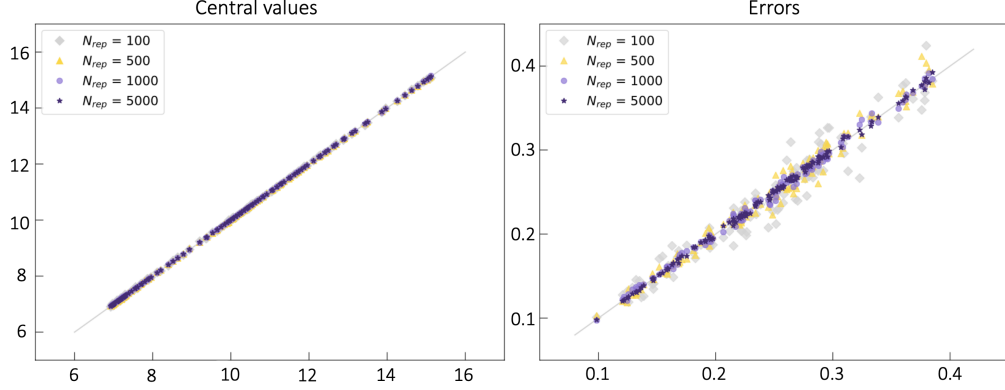


**Figure 5.4.** Comparison between the original experimental central values  $I_{\text{ZLP},i}^{\text{exp}}$  (left panel) and the corresponding statistical uncertainties  $\sigma_i^{(\text{stat})}$  with the results of averaging over a sample of  $N_{\text{rep}}$  Monte Carlo replicas generated by means of Eq. (5.6), for different values of  $N_{\text{rep}}$ .

MC replicas,  $N_{\text{rep}}$ , should be chosen such that the set of replicas models accurately the probability distribution of the original training data.

To verify that this is the case, Fig. 5.4 shows the original experimental central values  $I_{\text{ZLP},i}^{\text{(exp)}}$  (left) and the corresponding total uncertainties  $\sigma_i^{\text{(exp)}}$  (right panel), plotted against the results of averaging over a sample of  $N_{\text{rep}}$  Monte Carlo replicas generated by means of Eq. (5.6) for different numbers of replicas. We find that  $N_{\text{rep}} = 500$  is a value that ensures that both the central values and uncertainties are reasonably well reproduced, and we adopt it in what follows.

### 5.3 Training strategy

The training of the neural-network model for the ZLP peak differs between the cases of EEL spectra taken on vacuum, where by construction  $I_{\text{EEL}}(\Delta E) = I_{\text{ZLP}}^{\text{(mod)}}(\Delta E)$ , and for spectra taken on samples. In the case of spectra recorded on specimens, we need to find a training strategy to make predictions on the ZLP distribution in the low-loss regime, while we can not directly train on data in this region, since inelastic scattering contributions are also present. In this section we will describe the training strategy that is used in both cases.

#### Training of vacuum spectra

For each of the  $N_{\text{rep}}$  generated Monte Carlo replicas, we train an independent neural network as described in Sect. 5.1. Fitting the neural networks parameters to the data is performed by minimisation of a figure of merit (error function), defined as:

$$E^{(k)} (\{\theta^{(k)}\}) = \frac{1}{n_{\text{dat}}} \sum_{i=1}^{n_{\text{dat}}} \left( \frac{I_{\text{ZLP},i}^{\text{(art)}(k)} - I_{\text{ZLP},i}^{\text{(mod)}} (\{\theta^{(k)}\})}{\sigma_i^{\text{(exp)}}} \right)^2, \quad (5.9)$$

which is the  $\chi^2$  per data point computed for each MC pseudo replica compared with the corresponding model prediction. In this expression  $E^{(k)} (\{\theta^{(k)}\})$  is the error for the specific values  $\{\theta^{(k)}\}$ , representing the network weights and thresholds;  $I_{\text{ZLP},i}^{\text{(art)}(k)}$  is the  $k$ -th replica for the ZLP intensity and  $I_{\text{ZLP},i}^{\text{(mod)}}$  is the model prediction on this replica; and  $\sigma_i^{\text{(exp)}}$

again represents the error associated to this experimental data point.

The chi-squared method is the cornerstone of almost all fitting, as it is an intuitively reasonable measure of how well the predictions fit the data. If the model predictions are all within one standard deviation from the data, then the  $\chi^2$  per data point takes a value roughly equal to 1. In general, if  $\chi^2/n_{dat}$  is of the order 1, we can say that the fit is a good approximation to the real data.

To speed up the neural network training process, prior to the optimisation all inputs and outputs are scaled to lie between [0.1, 0.9] before being passed to the network. This preprocessing step facilitates that the neuron activation states will typically lie close to the linear region of the sigmoid activation function, which can be observed from Fig. 4.2.

In order to make sure that the model predictions are physically correct, it is often necessary to impose certain constraints to the model. In this case, our model for the ZLP should satisfy the restriction that the ZLP intensity disappears at very high energy loss, since in this region the ZLP contribution can be completely neglected:

$$I_{ZLP}(\Delta E) \rightarrow 0 \text{ for } |\Delta E| \rightarrow \infty.$$

We need to complement the figure of merit with the contribution coming from this theoretical constraint. This can be achieved by adding  $n_{pd}$  pseudo-data points to the training dataset "far" away from the ZLP and modifying the cost function Eq. (5.9) accordingly,

$$E^{(k)}(\{\theta^{(k)}\}) \rightarrow E^{(k)}(\{\theta^{(k)}\}) + E_{pd}^{(k)}(\{\theta^{(k)}\}) \quad (5.10)$$

where  $E_{pd}^{(k)}$  is the contribution to the cost function coming from the pseudo data points. By adding this extra term, we make sure that the optimization of the error function also takes into account the fact that at higher losses the intensity should vanish. However, when calculating the overall fit quality after training, we do not include the second term on the right-hand side of Eq. (5.10) in the evaluation of the figure of merit, as these "fake" datapoints do not give any physical information about the original dataset whatsoever.

The pseudo-data points are added in the region  $[\Delta E_{pd}^{(\min)}, \Delta E_{pd}^{(\max)}]$ , and symmetrically for negative energy losses. Since the aim of these pseudo points is to impose the restriction that  $I_{ZLP} \rightarrow 0$ , we need to make sure to choose the regime such that the ZLP intensity is indeed negligible in this limit. This can be achieved by looking at the ratio between the central experimental intensity and the total uncertainty in each data point:

$$\mathcal{R}_{sig}(\Delta E_i) \equiv \frac{I_{ZLP}^{(\exp)}(\Delta E_i)}{\sigma^{(\exp)}(\Delta E_i)}. \quad (5.11)$$

This ratio in fact denotes the significance for the  $i$ -th bin of  $\Delta E$  to differ from the null hypothesis (zero intensity) with respect to the experimental uncertainties.

The value of  $\Delta E_{pd}^{(\min)}$  can be determined automatically by evaluation of this ratio. For sufficiently large energy loss,  $\mathcal{R}_{sig}$  approaches 1, which indicates that we are essentially fitting statistical noise. In order to avoid this and only fit data that is different from zero within errors, we determine the value of  $\Delta E_{pd}^{(\min)}$  from the condition that  $\mathcal{R}_{sig}(\Delta E_i) \simeq 1$ . We keep the training data in the region  $\Delta E \leq \Delta E_{pd}^{(\min)}$  and the pseudo-data points are added for  $[\Delta E_{pd}^{(\min)}, \Delta E_{pd}^{(\max)}]$ . The value of  $\Delta E_{pd}^{(\max)}$  can be chosen arbitrarily and can

be as large as necessary to ensure that  $I_{\text{ZLP}}(\Delta E) \rightarrow 0$  as  $|\Delta E| \rightarrow \infty$ .

We note that another important physical condition on the ZLP model is its absolute positivity, since in EEL spectra the intensity is just a measure of the number of counts in the detector for a given value of the energy loss. This condition is automatically satisfied since we use a ReLU activation function for the last layer.

A further obvious requirement is that the best fit is independent of any assumptions made about the ZLP distribution. This requirement can be met by making sure the parametrisation is redundant: the size of the neural network used, and therefore the number of optimizable parameters, is much larger than the minimum required in order to reproduce the data. This redundancy can be verified *a posteriori*, by making sure that results are independent of the size and architecture of the neural network.

In this work we adopt the `TensorFlow` machine learning library to assemble the architecture illustrated in Fig. 5.1. Before training, all weights and biases are initialized in a non-deterministic order by the built-in global variable initializer. The optimisation of the cost function Eq. (5.10) is carried out by means of stochastic gradient descent (SGD) combined with backpropagation. The specific SGD optimizer used is the Adam algorithm. The hyper-parameters of the optimisation algorithm such as the learning rate have been adjusted to ensure proper learning is reached in the shortest amount of time possible.

Given that we have an extremely flexible parametrisation, one should be careful to avoid overlearning the input data. Here over-fitting is avoided by means of a cross-validation stopping criterion called look-back stopping, which has been explained briefly before in Sect. 4. We separate the input data into training and validation subsets, with a 80%/20% splitting which partition varies randomly for each Monte Carlo replica. We then run the optimiser for a very large number of iterations and store both the state of the network and the value of the figure of merit Eq. (5.9) for both the training and validation dataset. At the optimal stopping point, the network reproduces the information contained in the dataset, but not its statistical fluctuations. This point can be determined by the formulation of a stopping criterion, making it possible to, once the network completed the training, choose the parametrization of the network weights right before it entered the overlearning regime. The optimal stopping point is determined for each replica by keeping track of the figure of merit, which typically evolves as depicted in Fig. 4.3. The specific network configuration that leads to the deepest minimum of  $E_{\text{val}}^{(k)}$  is chosen after training, which why it is called look-back stopping, a method that has been widely used in the context of neural networks.

The number of epochs should be chosen high enough to reach for each replica the absolute minimum of  $E_{\text{val}}^{(k)}$ , rather than a local minimum. For this work we need approximately 40,000 epochs to guarantee overlearning. This corresponds to a serial running time of 60 seconds per replica when running the optimization on a single CPU for a set of 500 datapoints.

Once the training of all the  $N_{\text{rep}}$  neural network models for the ZLP has been carried out as specified above, we assess the overall fit quality of the model by computing the

average  $\chi^2$  per data point, defined as

$$\chi^2 = \frac{1}{n_{\text{dat}}} \sum_{i=1}^{n_{\text{dat}}} \left( \frac{I_{\text{ZLP},i}^{(\text{exp})} - \langle I_{\text{ZLP},i}^{(\text{mod})} \rangle_{\text{rep}}}{\sigma_i^{(\text{exp})}} \right)^2, \quad (5.12)$$

which is in fact similar to Eq. (5.9) now comparing the average model prediction to the original experimental data values. Note that here we do not include the contribution coming from the pseudo data points.

A value  $\chi^2 \simeq 1$  indicates that a satisfactory description of the experimental data, within the corresponding uncertainties, has been achieved. Note that in realistic scenarios  $\chi^2$  can be different from unity, for instance when some source of correlation between the experimental uncertainties has been neglected or when the errors on the data points have been over- or underestimated.

### Training of sample spectra

In the previous section, in absence of a specimen the total intensity profile is composed of only the ZLP contribution. The training strategy in the case of EEL spectra taken on samples must be adjusted to account for the fact that the total intensity, Eq. (5.1), receives contributions both from the ZLP and from inelastic interactions. To avoid biasing the ZLP model, we should make sure to pre-process the sample data sets, to guarantee that only the contribution coming from the ZLP is included in the training data. Else, if we were to train the neural network on data that contains also inelastic contributions, subsequent subtraction to the EEL spectra would make us lose important information.

The question at hand is how to find the value below which we have to drop the training data, in other words, how can we be sure that we are fitting only the ZLP contribution. In order to answer this question, we use a simplified model for the low-loss region of the spectra, which we display in Fig 5.5.

This figure illustrates how the total intensity is the sum of the two separate contributions, with the inset showing the values of the corresponding derivatives,  $dI/d\Delta E$ . The first contribution is coming from the ZLP, for which we use a general assumption that it can be described by a Gaussian distribution, centered around zero and with a standard deviation of  $\sigma_{\text{ZLP}} = 0.3$  eV. The inelastic interaction can in the low-loss regime be approximated by  $I_{\text{inel}}(\Delta E) \propto (\Delta E - E_{\text{bg}})^b$ , with  $E_{\text{bg}} = 1.5$  and  $b = 0.5$ . The motivation for this choice will be explained in Sect. 7.

From the simplified model in Fig. 5.5, we can draw a number of useful observations:

- The ZLP intensity,  $I_{\text{ZLP}}(\Delta E)$ , is monotonically decreasing and thus its derivative is always negative.
- The derivative of the total spectrum however,  $dI_{\text{EELS}}/d\Delta E|_{\Delta E_{\min}} = 0$ , crosses zero at a certain energy loss. This point corresponds to the first local minimum of  $I_{\text{EEL}}$ , and it marks the energy loss ( $\Delta E_{\min}$ ) for which the contribution from the inelastic emissions is really evident.
- In the low-loss regime, the derivatives of in-vacuum and in-sample spectra behave very similar, but they start to differ gradually at the point where the inelastic interactions start to contribute to the spectrum.

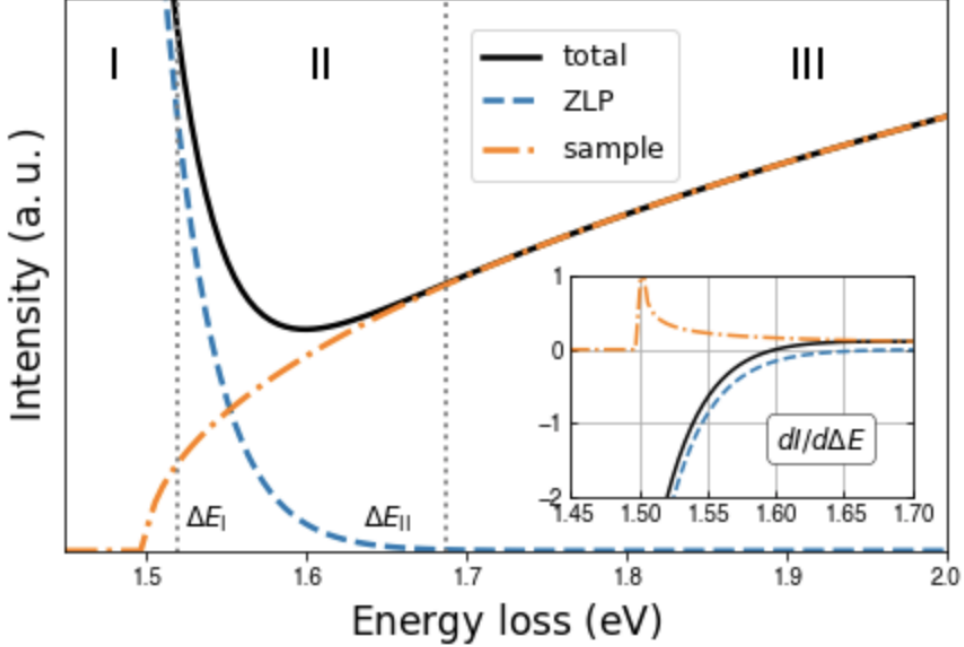


**Figure 5.5.** A toy model for a generic EEL spectrum and its derivatives (in the inset). We show the separate contributions from  $I_{\text{ZLP}}$  and  $I_{\text{inel}}$  as well as their sum. We indicate the two regions used for the model training (*I* and *III*), while the trained model is interpolated to region *II*, defined for  $\Delta E_I \leq \Delta E \leq \Delta E_{II}$ .

These considerations suggest that when training the machine learning model on EEL spectra taken on samples, we should consider three different regions, as indicated in Fig. 5.5.

#### Region I. ( $\Delta E \leq \Delta E_I$ )

For very low energy loss, the inelastic scattering contributions do not constitute (noticeably) to the total spectrum. This corresponds to the ZLP-regime and we can use the training points in this region for training the model, which proceeds in the same way as for the vacuum case via the minimisation of Eq. (5.9).

#### Region II. ( $\Delta E_I \leq \Delta E \leq \Delta E_{II}$ )

In this intermediate regime, the contribution coming from the inelastic interactions is already significant. Since we only want predictions on ZLP data and exclude all inelastic scattering, we exclude the EELS data between  $\Delta E_I$  and  $\Delta E_{II}$  from the training dataset. The ZLP predictions here will be an interpolation between predictions made on regime I and III.

#### Region III. ( $\Delta E \geq \Delta E_{II}$ )

For high energy loss, we are sure that the ZLP intensity is negligible:  $I_{\text{inel}} \gg I_{\text{ZLP}}$ . In this regime, we fit only the pseudo data points and we drop the experimental data. Therefore, the only information that region III provides on the model is from the constraint that  $I_{\text{ZLP}}(\Delta E \rightarrow \infty) \rightarrow 0$ .

This classification introduces two new hyper-parameters to our model,  $\Delta E_I$  and  $\Delta E_{II}$ , that need to be specified before training. They should satisfy  $\Delta E_I \leq \Delta E_{\min}$  and  $\Delta E_{II} \geq$

$\Delta E_{\min}$ , with  $\Delta E_{\min}$  being the position of the first local minimum of  $I_{\text{EEL}}$ . Let us interpret this physically:  $\Delta E_{\min}$  is the first local minimum, which means that the inelastic contributions are significantly present. Training on data with energy loss higher than this value, we are sure that our training data includes at least some amount of inelastic scatterings. Therefore, it is certain that we need to cut the training data already at a lower energy loss, so  $\Delta E_I \leq \Delta E_{\min}$ . As indicated by the toy spectra of Fig. 5.5, a suitable value for  $\Delta E_I$  would be somewhat above the onset of the inelastic contributions: this way we maximise the amount of training data while ensuring that  $I_{\text{EEL}}$  is still dominated by  $I_{\text{ZLP}}$ .

We can use the derivatives of the spectra,  $dI_{\text{EEL}}/d\Delta E$ , to automatically select suitable minimum and maximum values for  $\Delta E_I$ . Using first and second derivatives is an often-used feature extraction method to achieve a relatively high accuracy with a low computational complexity. In an ideal microscope the electron beam would be perfectly monochromatic, correspondingly the ZLP would appear as a delta function in an EEL spectrum [14]. In practice the ZLP has a finite width defining the energy resolution of the system.

The minimum possible value for  $\Delta E_I$  is selected as the value where the derivative taken on the sample data start to differ significantly as compared to those spectra taken on vacuum. In order to decide when these derivatives start to deviate, we look at the ratio of the one over the other:

$$R_{dI/d\Delta E} = \left( \frac{dI_{\text{ZLP}}/d\Delta E}{dI_{\text{EEL}}/d\Delta E} \right). \quad (5.13)$$

At energy loss  $\Delta E_{I,\min}$  the sample spectrum stops monotonically decreasing and the ratio deviates from 1; it is this point where the contributions from the sample start to change the shape of the ZLP distribution and we can use this measure to mark the transition from regime I to regime II in Fig. 5.5. Knowing that  $\Delta E_I \geq \Delta E_{I,\min}$  and  $\Delta E_I \leq \Delta E_{\min}$ , we now have a range of possible  $\Delta E_I$  values to train the neural network. Note that this corresponds to the region where  $R_{dI/d\Delta E} \neq 1$  and  $R_{dI/d\Delta E} \geq 0$ . The training will be done on a range of different  $\Delta E_I$  values within this interval and the optimal choice will be determined afterwards. Also, generating results for different values of  $\Delta E_I$  enables us to cross-validate on the stability of our results regardless of the exact choice of this hyperparameter.

Now that we have laid out a strategy to determine  $\Delta E_I$ , we yet have to define the value of  $\Delta E_{II}$ , whose minimum value should mark the region where  $I_{\text{ZLP}}(\Delta E \rightarrow \infty) \rightarrow 0$ . It is the value where we start adding pseudo-data, so  $\Delta E_{II} = \Delta E_{\text{pd,min}}$ . In order to implement this constraint, similar to the previous section (Eq. (5.11)) we look at the ratio  $\mathcal{R}_{\text{sig}}(\Delta E_i)$  to determine the energy loss  $\Delta E_{\text{pd}}$  at which the contributions from the vacuum-recorded ZLP vanish. As a measure, we use the energy loss value where the ratio  $\mathcal{R}_{\text{sig}}(\Delta E_i)$  drops below 1, as in this regime we would be fitting statistical noise. We set the value of  $\Delta E_{II}$  equal to this energy loss and add pseudo-data points for  $\Delta E \geq \Delta E_{II}$ . Note that in this region the intensity of the ZLP is several orders of magnitude smaller than the intensity of the inelastic emissions and therefore the exact choice of  $\Delta E_{II}$  is not too delicate.

Now that we have determined our strategy for the parametrisation of the ZLP, we move on to present the results, first on vacuum recorded data and afterwards on specimen data.

## 6 Results I. Vacuum spectra

In this section we present the application of the previously presented strategy to the parametrisation of ZLP spectra acquired in vacuum. Applying our model to this case has a two-fold motivation. First of all, we aim to demonstrate that our model is flexible enough to effectively reproduce the input EELS measurements for a range of variations of the operation parameters of the microscope. Herefore, we modify the input parameters beyond those included in the training set and see how the model is able to interpolate and extrapolate on its inputs.

Second, it will allow us to provide a calibration prediction useful for the case of the in-sample measurements. Such calibration is necessary since, as explained in Sect. 5.3, some of the model hyper-parameters are determined by the comparison of the intensity derivatives between spectra taken in vacuum and those in sample.

In this section, first of all we present the input dataset and motivate the choice of training settings and model hyperparameters. Then we validate the model training by assessing the fit quality. Afterwards, we study the dependence of the model predictions in its various input variables, and study the dependence of the model uncertainties upon the removal of a subset of the training dataset. Lastly, we perform some checks to assess the reliance and stability of our results.

### 6.1 Training initialization

In Table 6.1 we collect the main properties of the EELS spectra acquired in vacuum to train the neural network model. For each set of spectra, we indicate the exposure time  $t_{\text{exp}}$ , the beam energy  $E_b$ , the number of spectra  $N_{\text{sp}}$  recorded for these operation conditions, the number  $N_{\text{dat}}$  of bins in each spectrum, the range in electron energy loss  $\Delta E$ , and the average full width at half maximum (FWHM) evaluated over the  $N_{\text{sp}}$  spectra with the corresponding variance. We point out that since here we are interested in the low-loss region,  $\Delta E_{\text{max}}$  does not need to be too large, and in any case the large  $\Delta E$  behaviour of the model is fixed by the constraint implemented by Eq. (5.10).

Set	$t_{\text{exp}}$ (ms)	$E_b$ (keV)	$N_{\text{sp}}$	$N_{\text{dat}}$	$\Delta E_{\text{min}}$ (eV)	$\Delta E_{\text{max}}$ (eV)	FWHM (meV)
1	100	200	15	2048	-0.96	8.51	$47 \pm 7$
2	100	60	7	2048	-0.54	5.59	$50 \pm 4$
3	10	200	6	2048	-0.75	5.18	$26 \pm 3$
4	10	60	6	2048	-0.40	4.78	$34 \pm 2$

**Table 6.1.** Summary of the main properties of the EELS spectra acquired in vacuum to train the neural network model. For each set of spectra, we indicate the exposure time  $t_{\text{exp}}$ , the beam energy  $E_b$ , the number of spectra  $N_{\text{sp}}$  recorded for these operation conditions, the number  $N_{\text{dat}}$  of bins in each spectrum, the range in electron energy loss  $\Delta E$ , and the average FWHM evaluated over the  $N_{\text{sp}}$  spectra with the corresponding standard deviation

The energy resolution of these spectra, quantified by the value of their FWHM, ranges from 26 meV to 50 meV depending on the specific operating conditions of the microscope,

with a standard deviation between 2 and 7 meV. The value of the FWHM varies only slightly with the value of the beam energy  $E_b$  but grows by around a factor two for spectra collected at larger exposure times  $t_{\text{exp}}$ . A total of almost  $7 \times 10^4$  independent measurements will be used for the ZLP model training on the vacuum spectra. As will be highlighted in Sects. 6.3 and 6.4, one of the advantages of our ZLP model is that it can extrapolate its predictions to other operation conditions beyond those used for the training.

Following the strategy presented in Sect. 5, first of all we combine the  $N_{\text{sp}}$  spectra corresponding to each of the four sets of operation conditions and determine the statistical uncertainty associated to each energy loss bin by means of Eq. (5.8). The resulting set of training points can be observed in Fig. 6.1. Note that the intensities of each set have been normalized by the corresponding maximum intensity.

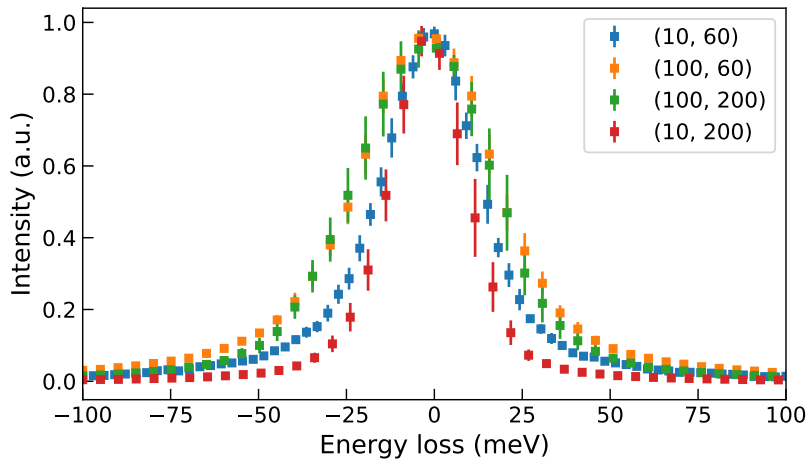


**Figure 6.1.** Graphical representation of the four sets of training inputs that have been calculated as the central experimental value of the total EELS intensity,  $I_{\text{EEL},i}^{(\text{exp})}$ , and the corresponding total uncertainty defined in Eq. (5.8). Each set is represented by its operating conditions ( $t_{\text{exp}}$ ,  $E_b$ ) given in ms and keV respectively. Note that the intensities of each set have been normalized by the maximum intensity.

For each of the training sets, we need to determine the value of  $\Delta E_{\text{pd}}^{(\min)}$  that defines the lower limit of the range for which we add the pseudo-data that imposes the correct  $\Delta E \rightarrow \infty$  limit of the model. This value is determined by inspecting the ratio between the central experimental value of the total EELS intensity,  $I_{\text{EEL},i}^{(\text{exp})}$ , and its corresponding total uncertainty defined in Eq. (5.8).

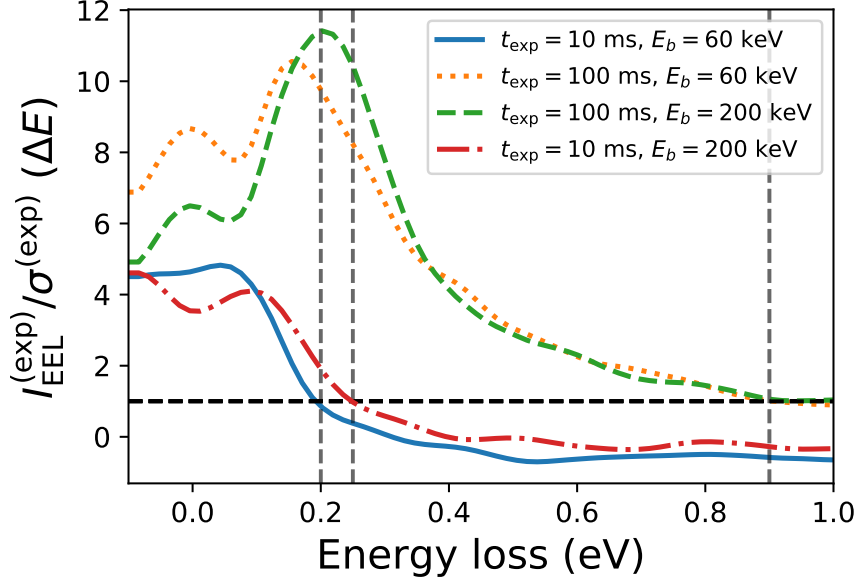


**Figure 6.2.** The ratio between the central experimental value of the total EELS intensity,  $I_{\text{EEL},i}^{(\text{exp})}$ , and the corresponding total uncertainty defined in Eq. (5.8). Results are shown for the four combinations of  $t_{\text{exp}}$  and  $E_b$  listed in Table 6.1. The vertical dashed lines mark the values of  $\Delta E$  for which this ratio becomes smaller than unity, which indicates when the input data starts to be dominated by the statistical noise.

Fig. 6.2 displays this ratio for the four combinations of  $t_{\text{exp}}$  and  $E_b$  listed in Table 6.1. The vertical dashed lines indicate the values of  $\Delta E$  for which this ratio becomes smaller than unity. For larger  $\Delta E$ , the EELS spectra become consistent with zero within uncertainties and can thus be discarded and replaced by the pseudo-data constraints. Thus the cross-over value of  $\Delta E$  where the ratio satisfies  $I/\sigma \simeq 1$  is a reasonable choice for  $\Delta E_{\text{pd}}^{(\text{min})}$ . We note from Fig. 6.2 that  $\Delta E_{\text{pd}}^{(\text{min})}$  will depend on general on the operation conditions. We find that for our training samples  $\Delta E_{\text{pd}}^{(\text{min})} \simeq 200$  meV for  $t_{\text{exp}} = 10$  ms and  $\simeq 900$  meV for 100 ms, roughly independent on the value of  $E_b$ .

The total uncertainty of the pseudo-data points is chosen to be

$$\sigma_j^{(\text{pd})} = \frac{1}{10} I_{\text{EEL}}^{(\text{exp})} \left( \Delta E = \Delta E_{\text{pd}}^{(\text{min})} \right), \quad j = 1, \dots, N_{\text{pd}}. \quad (6.1)$$

The factor of 1/10 is found to be suitable to ensure that the constraint is enforced without distorting the training to the experimental data.

The input experimental measurements listed in Table 6.1 are used to generate a sample of  $N_{\text{rep}} = 500$  Monte Carlo replicas and train an individual neural network model to each of these replicas. The end result of the procedure is a set of model replicas,

$$I_{\text{ZLP}}^{(\text{mod})(k)}(\Delta E, E_b, t_{\text{exp}}), \quad k = 1, \dots, N_{\text{rep}}, \quad (6.2)$$

which can be used to provide a prediction for the intensity of the ZLP for arbitrary values of  $\Delta E$ ,  $E_b$ , and  $t_{\text{exp}}$ . Eq (6.2) provides the desired representation of the probability density in the space of ZLP models.

From the ensemble of replicas one can evaluate statistical estimators such as averages and variances by means of the usual expressions:

$$\left\langle I_{\text{ZLP}}^{(\text{mod})}(\{\text{input}_i\}) \right\rangle = \frac{1}{N_{\text{rep}}} \sum_{k=1}^{N_{\text{rep}}} I_{\text{ZLP}}^{(\text{mod})(k)}(\{\text{input}_i\}), \quad (6.3)$$

$$\sigma_{I_{\text{ZLP}}^{(\text{mod})}}(\{\text{input}_i\}) = \left( \frac{1}{N_{\text{rep}} - 1} \sum_{k=1}^{N_{\text{rep}}} \left( I_{\text{ZLP}}^{(\text{mod})(k)} - \left\langle I_{\text{ZLP}}^{(\text{mod})} \right\rangle \right) \right)^{1/2}, \quad (6.4)$$

where  $\{\text{input}_i\}$  is a set of input parameters ( $\Delta E_i, E_{\text{b},i}, t_{\text{exp},i}$ ).

## 6.2 Fit quality

We now discuss some of features of this ZLP vacuum model. To begin with, we would like to quantify the overall fit quality of the model and demonstrate that it is flexible enough to describe all the available input datasets. In Table 6.2 we indicate the values of the final  $\chi^2$  per data point, Eq. (5.12), as well as the average values of the error Eq. (5.9) over the training and validation subsets, for each of the four sets of spectra listed in Table 6.1 as well as for the total dataset. We recall that for a satisfactory training one expects  $\chi^2 \simeq 1$  and  $\langle E_{\text{tr}} \rangle \simeq \langle E_{\text{val}} \rangle \simeq 2$  [66]. From the results of this table we find that, while our values are consistent with a reasonably good training, somewhat lower values than expected are obtained, for instance  $\chi_{\text{tot}}^2 \simeq 0.8$  for the total dataset. This suggests that correlations between the input data points might be partially missing, since neglecting them often results into a moderate overestimate of the experimental uncertainties.

Set	$\chi^2$	$\langle E_{\text{tr}} \rangle$	$\langle E_{\text{val}} \rangle$
1	0.998	1.702	1.970
2	0.733	1.408	1.767
3	0.697	1.391	1.800
4	0.593	1.201	1.761
Total	0.771	1.470	1.853

**Table 6.2.** The values of the final  $\chi^2$  per data point, Eq. (5.12), as well as the average values of the error Eq. (5.9) over the training and validation subsets, for each of the four sets of spectra listed in Table 6.1 as well as for the total dataset.

The left panel in Fig. 6.3 shows the  $\chi^2$  distributions evaluated for the training and validation sets of the  $N_{\text{rep}} = 500$  replicas of the sample trained on the spectra listed in Table 6.1. Note that the training/validation partition differs at random for each replica. The  $\chi_{\text{tr}}^2$  distribution peaks at  $\chi_{\text{tr}}^2 \simeq 0.7$ , indicating that a satisfactory model training has been achieved, but also that the errors on the input data points might have been slightly overestimated. We emphasize that the stopping criterion for the neural net training adopted here never considers the numerical values of the error function and determines proper learning entirely from the global minima of  $E_{\text{val}}^{(k)}$ . From Fig. 6.3 we also observed

that  $\chi^2_{\text{tr}}$  distribution peaks at a slightly higher value,  $\simeq 1$ , and is broader than its corresponding training counterpart. These results confirm both that a satisfactory model training that prevents overlearning has been achieved as well as an appropriate estimate of the statistical uncertainties affecting the original EEL spectra.

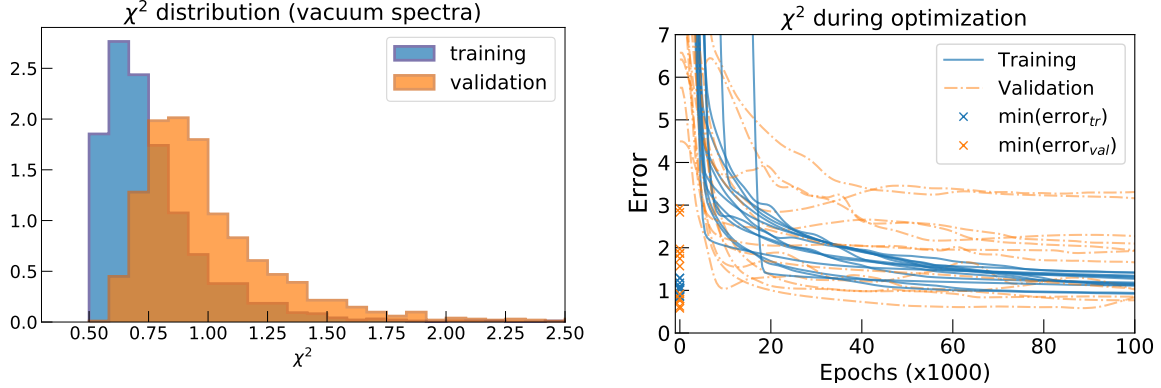


**Figure 6.3.** Left panel: The  $\chi^2$  (per data point) distribution evaluated for the training and validation sets of the  $N_{\text{rep}} = 500$  replicas of the sample trained on the spectra listed in Table 6.1. Right: the progress of the training and validation error over the course of the optimization. Number of replicas is taken small for clarity. The final  $\chi^2$  is marked on the y-axis and shows how the distribution of training errors is more narrow and centered at a lower value compared to the validation errors.

From Table 6.2 we observe that the  $\chi^2$  of the central fit is about half the size of the error, which measures the quality of the fit for each MC replica. This is what we would expect for a fit that correctly represents the fluctuations of the underlying set of experimental data: given that replicas fluctuate about the experimental measurements, these measurements themselves fluctuate about their "true" underlying values.

The right panel in Fig. 6.3 displays the evolution of the training and validation error over the course of the optimization, and the ultimate  $\chi^2_{\text{tr}}$  and  $\chi^2_{\text{val}}$  outcomes on the vertical axis. It can be observed that the collection of  $\chi^2_{\text{tr}}$  values end up closer to each other and centered around a lower value than  $\chi^2_{\text{val}}$ , which visualizes the origin of the difference between the two histogram given in the left panel of the same figure. Note that the amount of replicas is greatly reduced here ( $N_{\text{rep}} = 10$ ) for better visualization.

### 6.3 Dependence on the electron energy loss

Having demonstrated that our neural network model provides a satisfactory description of all the input EEL spectra, we now present its predictions for specific choices of the input parameters. First of all, we investigate the dependence of the results as a function of the electron energy loss  $\Delta E$ . Fig. 6.4 displays the central value and 68% confidence level uncertainty band for the ZLP model as a function of electron energy loss  $\Delta E$  evaluated using Eqns. (6.3) and (6.4). We display results corresponding to three different values of  $E_b$  and for both  $t_{\text{exp}} = 10$  ms (left) and  $t_{\text{exp}} = 100$  ms (right panel). We emphasize that only beam energies of 60 and 200 keV were included in the dataset, so the network is trained on these data. It has never seen data with  $E_b = 120$  keV, and thus our prediction in this case arises purely from the model interpolation. It is interesting to note how both the overall normalisation and the shape of the predicted ZLP depend on the specific operation conditions.

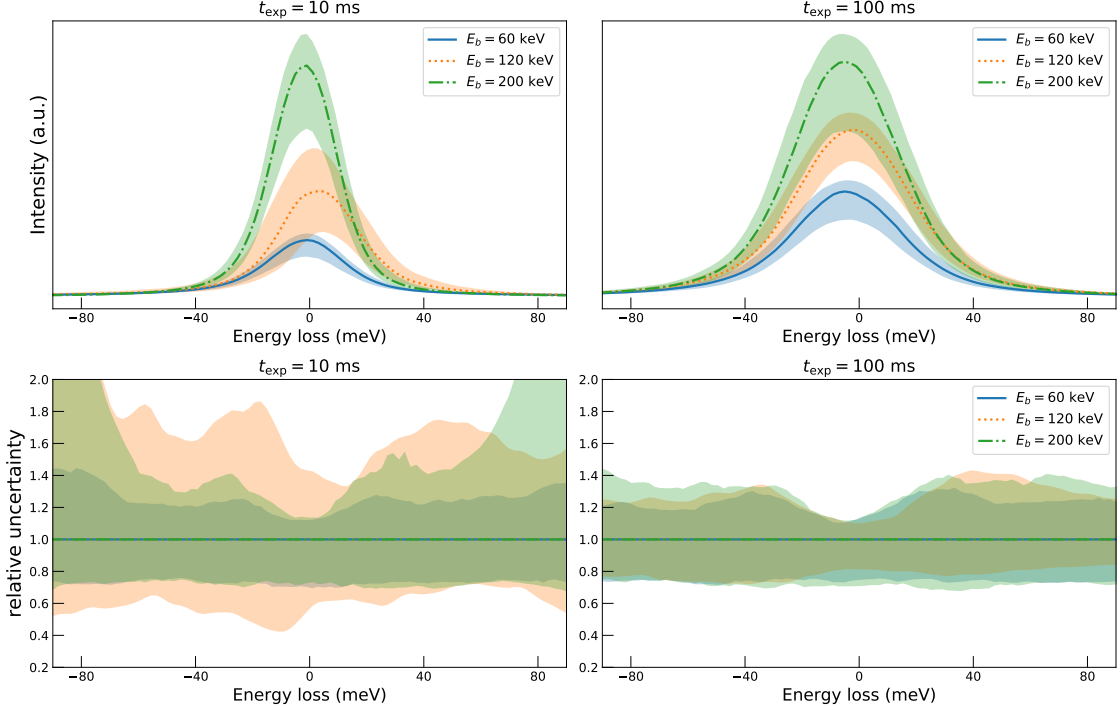


**Figure 6.4.** Top: the central value and 68% confidence level uncertainty band for the ZLP model as a function of electron energy loss  $\Delta E$  evaluated using Eqns. (6.3) and (6.4). We display results corresponding to three different values of  $E_b$  and for both  $t_{\text{exp}} = 10 \text{ ms}$  (left) and  $t_{\text{exp}} = 100 \text{ ms}$  (right panel). Note that no training data with  $E_b = 120 \text{ keV}$  has been used and thus our prediction in that case arises purely from the model interpolation. Bottom: the corresponding relative uncertainty as a function of  $\Delta E$  for each of the three values of  $E_b$ .

In the bottom panel of Fig. 6.4 we show the corresponding relative uncertainty as a function of  $\Delta E$  for each of the three values of  $E_b$ . The relative uncertainty is calculated as the absolute error in each point divided by the predicted intensity. Recall that in this work we allow for non-Gaussian distributions and thus the central value is the mean of the distribution while the error band in general will be asymmetric. Looking at the predictions for  $t_{\text{exp}} = 10 \text{ ms}$ , we see how the model prediction at  $E_b = 120 \text{ keV}$  typically exhibits larger uncertainties and is therefore less stable than the predictions for the two values of  $E_b$  for which we have training data. In the case of  $t_{\text{exp}} = 100 \text{ ms}$  instead, the model predictions exhibit very similar uncertainties for the three values of  $E_b$ , which furthermore depend only mildly on  $\Delta E$ . From these outcomes we can conclude that the network is well able to make predictions on inputs it has never seen before.

It is interesting to assess how the model results change once a subset of the data points is excluded from the fit. In other words, we remove data points in a certain region  $[\Delta E_{\text{cut}}^{(\text{min})}, \Delta E_{\text{cut}}^{(\text{max})}]$  and train the model on the resulting dataset. Afterwards, we let the model make predictions on the full energy range and see what the effect of such a cut is. The reason to do this goes hand in hand with the fact that we will need this model later onwards for the prediction on sample data. As explained in Sect. 5 and as illustrated in Fig. 5.5, when training the model on sample spectra, a region with  $\Delta E_I \leq \Delta E \leq \Delta E_{II}$  will be removed from the training dataset to avoid the contamination from the inelastic contributions. Fig. 6.5 displays the predicted central value and uncertainty in the model predictions for  $I_{\text{ZLP}}(\Delta E)$  as a function of the energy loss for  $E_b = 200 \text{ keV}$  and  $t_{\text{exp}} = 10$

ms (left) and 100 ms (right panel). We show results for three different sets of training: first of all, one without any cut in the training dataset, and then for the case where the data points with  $\Delta E \geq \Delta E_{\text{cut}}$  are removed from the training dataset. We consider two values of  $\Delta E_{\text{cut}}$ , namely 50 meV and 100 meV, indicated with vertical dash-dotted lines. In both cases, data points are removed up until  $\Delta E = 800$  meV. The pseudo-data points that enforce  $I_{\text{EEL}}(\Delta E) \rightarrow 0$  are present in all three cases in the region  $800 \text{ meV} \leq \Delta E \leq 1 \text{ eV}$ .

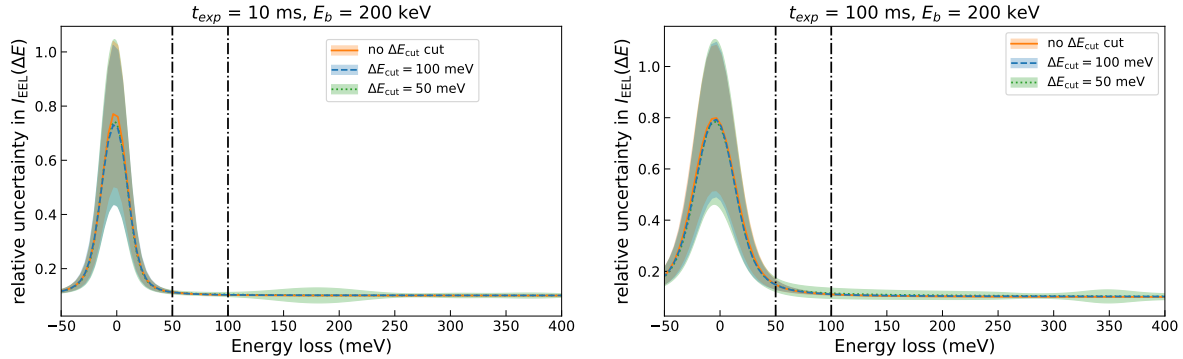


**Figure 6.5.** The central values and 68% uncertainty bands in the model predictions for  $I_{\text{EEL}}(\Delta E)$  as a function of the energy loss for  $E_b = 200$  keV and  $t_{\text{exp}} = 10$  ms (left) and 100 ms (right panel). We show results for three different sets of trainings: without any cut in the training dataset, and for the case where the data points with  $\Delta E \geq \Delta E_{\text{cut}}$  are removed from the training dataset for two different values of  $\Delta E_{\text{cut}}$ . Note that the same pseudo-data points that enforce  $I_{\text{EEL}}(\Delta E) \rightarrow 0$  are present in all three cases.

At first sight, the removal of data from the training dataset does not introduce large uncertainties for the ZLP predictions: they are little noticed when the data is cut at 50 meV, and for 100 meV the predictions seem identical to the full range training. To emulate the effects of such cut, one needs to look at the *relative* uncertainty rather than the absolute, that is, normalizing the uncertainty in each point to the predicted intensity. The results can be observed in Fig. 6.6. We show the relative uncertainty in the model predictions using two different x and y scales, to visualize the results as clearly as possible.

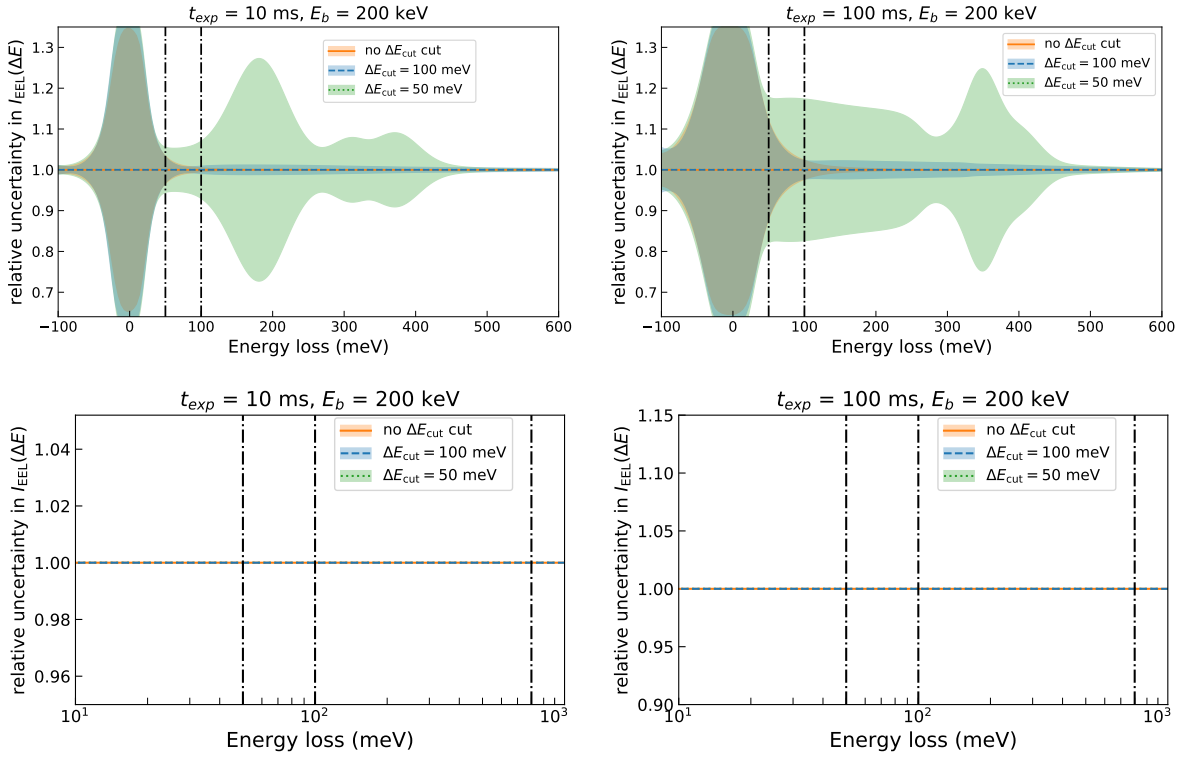


**Figure 6.6.** Top: The relative uncertainty in the model predictions for  $I_{\text{EEL}}(\Delta E)$  as a function of the energy loss for  $E_b = 200$  keV and  $t_{\text{exp}} = 10$  ms (left) and 100 ms (right panel). Bottom: same results with different x and y scales for better visualization of the differences in relative uncertainties.

From this comparison we can observe how the model predictions become significantly more unstable once a subset of the training data is cut away, as expected due to the effect of the information loss. While for the cut  $\Delta E_{\text{cut}} = 100$  meV the increase in model uncertainty is only moderate as compared with the baseline fit where no cut is performed (since for this value of  $\Delta E$  uncertainties are small to begin with), more dramatic effects are observed when datapoints are removed after  $\Delta E_{\text{cut}} = 50$  meV. This comparison highlights how ideally we would like to keep as many data points in the training set for the ZLP model, provided of course we can verify that the possible contributions to the spectra related to inelastic scatterings from the sample can be neglected.

## 6.4 Dependence on beam energy and exposure time

As indicated in Table 6.1, the training dataset contains spectra taken at two values of the electron beam energy,  $E_b = 60$  keV and 200 keV. The multi-dimensionality of our model allows for the interpolation and extrapolation between these settings, and in this section we evaluate how the FWHM of the model predictions varies for different values of  $E_b$ . The left panel of Fig. 6.7 displays model predictions for the FWHM of the zero-loss peak (and its corresponding uncertainty) as a function of the beam energy  $E_b$  for two values of the exposure time,  $t_{\text{exp}} = 10$  ms and 100 ms. The vertical dashed lines indicate the values of  $E_b$  for which training data is available. This comparison illustrates how the model uncertainty vary in the data region (near  $E_b = 60$  keV and 200 keV), the interpolation region (for  $E_b$  between 60 and 200 keV), and the extrapolation regions (for  $E_b$  below 60 keV and above 200 keV). For  $t_{\text{exp}} = 100$  ms, we observe that the model interpolates

reasonably well between the measured values of  $E_b$  and that uncertainties start increasing in the extrapolation region above  $E_b = 200$  keV.

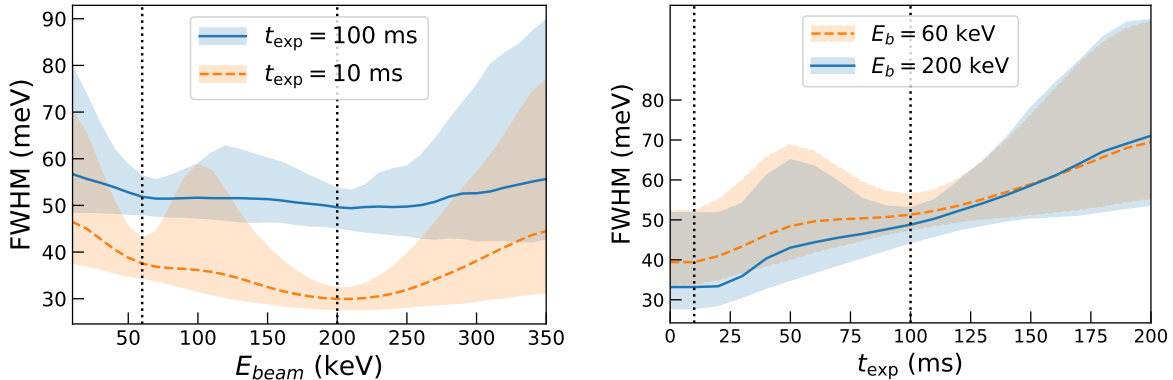


**Figure 6.7.** The model predictions for the FWHM of the zero-loss peak (and its corresponding uncertainty) as a function of the beam energy  $E_b$  for two values of the exposure time (left panel) and as a function of  $t_{\text{exp}}$  for two values of  $E_b$  (right panel). The vertical dashed lines indicate the values of the corresponding parameter for which training data is available.

For this comparison one can observe that - as expected - the uncertainty in the prediction for FWHM of the ZLP is the smallest close to the values of  $E_b$  for which one has training data. The uncertainties increase but only in a moderate way in the interpolation region, indicating that the model can be applied to reliably predict the features of the ZLP for other values of the electron beam energy (assuming that all other operating conditions of the microscope are unchanged). The errors increase rapidly in the extrapolation region, which is a characteristic feature of these neural network models. Indeed, as soon as the model departs from the data region there exist a very large number of different functional form models for  $I_{\text{ZLP}}(\Delta E)$  that can describe equally well the training dataset, and hence a blow up of the extrapolation uncertainties is generically expected.

The network was trained on data with exposure times of 10 and 100 ms, so also for this input variable interpolation and extrapolation is possible. Similar to the predictions for varying beam energy, also for exposure time the uncertainties grow bigger as the value deviates more from the training inputs. The right panel of Fig. 6.7 displays a similar model comparison as in the left panel but now as a function of  $t_{\text{exp}}$  for two values of  $E_b$ . We observe that the FWHM increases almost linearly with the exposure time, indicating (deservedly!) that lower values of  $t_{\text{exp}}$  allow for an improved spectral resolution. Also in this case we find that the model uncertainties grow rapidly in the extrapolation region beyond those covered in the training dataset.

## 6.5 Stability and reliability checks

In this section, we assess the stability of the results and the reliability of the error estimate regarding the neural network parametrisation.

To begin with, we study the dependence on the architecture of the neural networks. As previously mentioned, we have chosen a redundant architecture as to assure that the network is sufficiently large to parametrise the ZLP. In order to check that this is indeed

the case, we have both increased and decreased the number of neurons, so that we can assess the stability of results for both cases. Throughout this work, the default architecture has been 3-10-15-5-1. The "big" architecture was chosen as a 3-15-25-10-1, increasing the number of free parameters from 289 to 731. The "small" network corresponds to an architecture of 3-5-8-5-1, which brings only 119 free parameters to be optimised.

We have followed a similar procedure as presented in Sect. 6.3 to investigate the dependence of the results as a function of the energy loss, corresponding to  $E_b = 60$ , 120 and 200 keV. The central value and 68% confidence level band for the predicted ZLP distributions can be observed in Fig. 6.8 below, which can be directly compared to Fig. 6.4 for the default network.

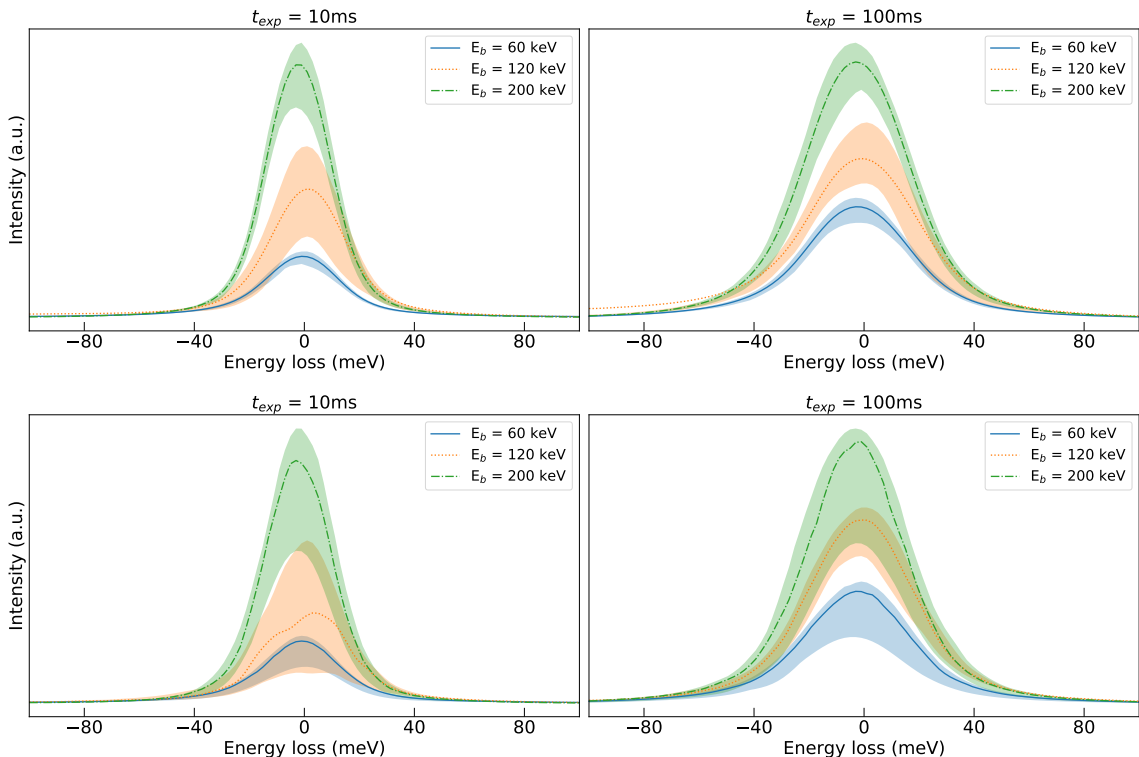


**Figure 6.8.** Similar to Fig. 6.4 but now for a network with twice (up) and half (down) the architecture. We see that when doubling the network, predictions are almost identical, except that uncertainty bands are slightly smaller. However, decreasing the network by a factor of 2 results in predictions that are a bit off from our default network. Note that the predictions made for  $E_b=120$  keV are purely interpolation results; the training set contains only data for beam energies of 60 and 200 keV.

It can be observed that results are well reproduced for both smaller and bigger graphs. Particularly for the large network, both the central values and the uncertainty bands are in almost perfect correspondence with the results presented in Sect. 6.3. This confirms the fact that our default network is sufficiently large and flexible to parametrise the ZLP: since increasing the size does not affect the obtained results, the number of optimizable parameters is much larger than the minimum required in order to reproduce the data.

This becomes more evident when we substantially decrease the size of the neural network. Predictions on the training data ( $E_b=60$  and 200 keV) are still consistent, however the uncertainty bands have grown remarkably bigger, indicating that the neural network outcomes are less stable than before. Also, using the smaller architecture, the network

needs a significantly longer computation time to come to the lowest value of  $\chi^2_{\text{val}}$ . When we look at the prediction for the interpolation ( $E_b=120$  keV), the central values differ (however only moderately) from the ones obtained on bigger networks. This difference indicates that the predicted outcomes indeed depend on the size of the network, and simultaneously it confirms the sufficient redundancy of the architecture used as default.

Next, we check that the results are stable among different subsets of 100 out of the total of 500 Monte Carlo replicas. The results can be observed in Fig. 6.9. We find remarkable stability: the two sets yield to almost identical representations, both for the training data as for the interpolation regime.

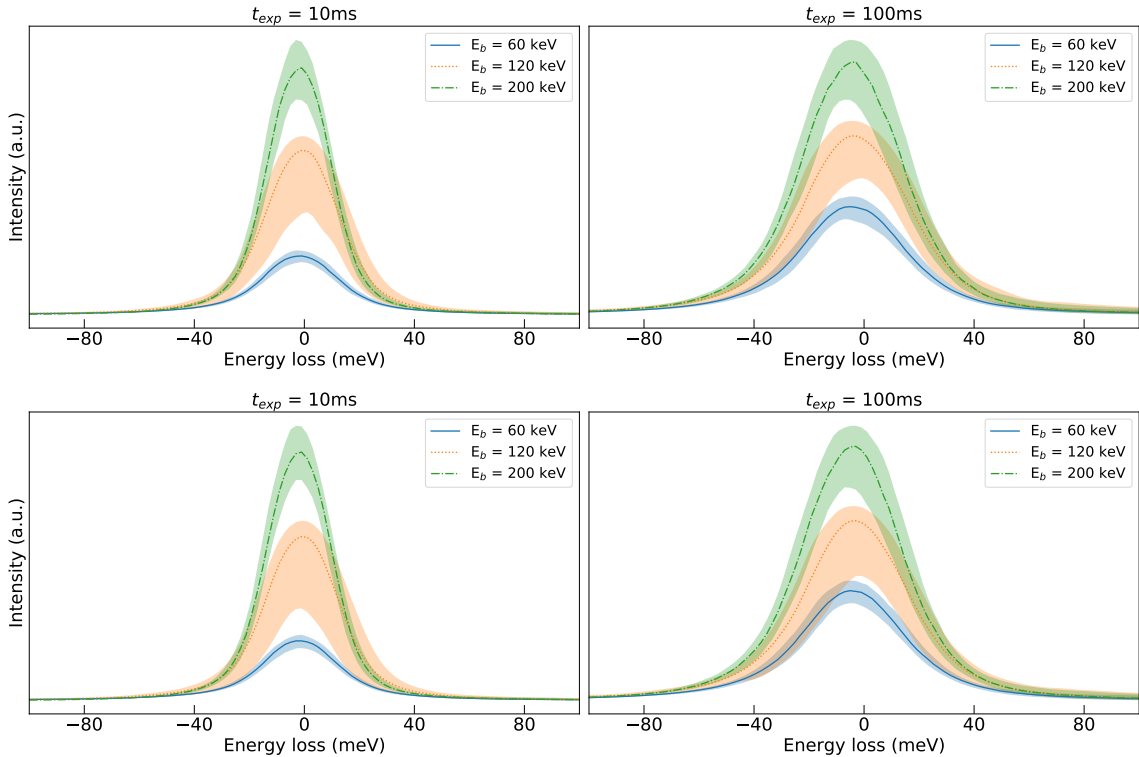


**Figure 6.9.** Similar to Fig. 6.4 but now for two subsets of 100 replicas instead of the full set of 500 replicas.

A final check is to see how uncertainties change with the number of replicas. We have produced the same plot but now based on three different sizes of MC ensembles:  $N_{\text{rep}}=25$ , 100 and 400. Again, we have created plots similar to the ones before, now using each time a different size of replicas. We would expect that using a small subset introduces larger errors compared to large ensembles of replicas. It is clear that for the smallest subset ( $N_{\text{rep}}=25$ ), in the peaks the predictions are already well produced, however uncertainties in the tails are significantly larger. The difference between using either 100 or 400 replicas is hardly noticeable, which confirms our statement given in Sect. 5.2 that 500 replicas is (more than) enough to obtain a faithful representation.

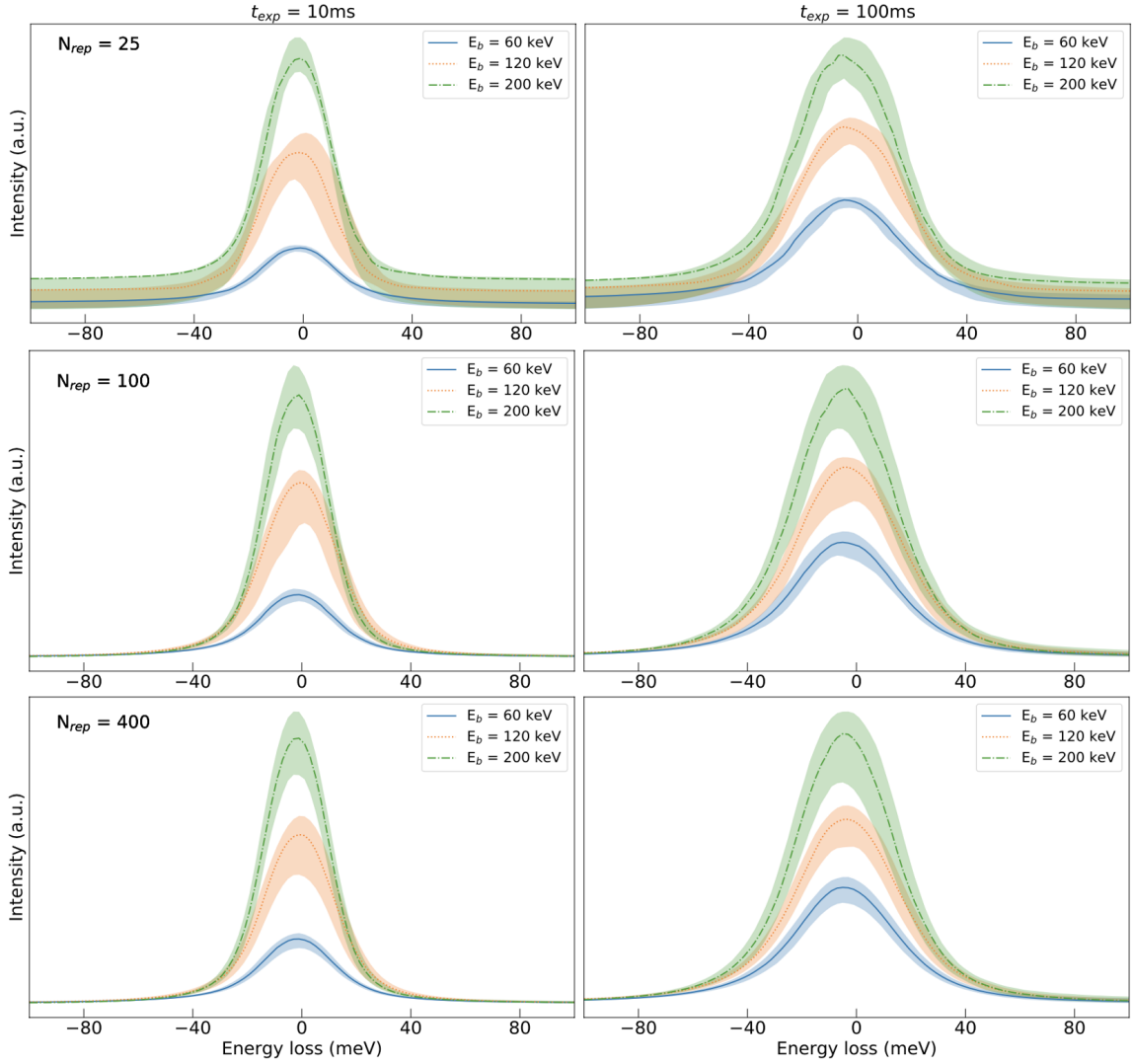


**Figure 6.10.** Predictions for three three different sizes of MC ensembles:  $N_{rep}=25$ , 100 and 400. For the smallest subset ( $N_{rep}=25$ ), uncertainties in the tails are significantly larger, but the difference between using either 100 or 400 replicas is hardly noticeable.

## 7 Results II. Sample spectra

Following the discussion of the vacuum ZLP analysis, we now present the application of our machine learning strategy to parametrise the ZLP arising in spectra recorded on specimens, specifically for EELS measurements acquired in different regions of the WS<sub>2</sub> nanoflowers presented in Sect. 2. The resulting ZLP parametrisation will be applied to isolate the inelastic contribution in each spectrum. We will use these subtracted spectra first to determine the bandgap type and energy value from the behaviour of the onset region and second to study features in the very-low-loss region.

We start this section by presenting the training dataset, which consists of two groups of EEL spectra recorded in thick and thin regions of the WS<sub>2</sub> nanoflowers respectively. Then we discuss the subtraction procedure, the choice of hyper-parameters, and the error propagation to the physical predictions. The resulting subtracted spectra provide the information required to extract the value and type of the bandgap and to characterise excitonic transitions for different regions of these polytypic WS<sub>2</sub> nanostructures.

### 7.1 Training dataset

Low-magnification TEM images and the corresponding spectral images of two representative regions of the WS<sub>2</sub> nanoflowers, denoted as sample A and B respectively, are displayed in Fig. 7.1. These spectral images have been recorded in the regions marked by a green square in the associated TEM images, and contain an individual EEL spectrum in each pixel. We indicate the specific locations where EEL spectra have been recorded, including the in-vacuum measurements acquired for calibration purposes. Note that in sample B the differences in contrast are related to the material thickness, with higher contrast corresponding to thinner regions.

These two samples are characterised by rather different structural morphologies. While sample A is a relatively thick region of WS<sub>2</sub>, sample B corresponds to a region composed of thin petals, which is only one or a few monolayers thick. In other words, sample A is composed by bulk WS<sub>2</sub> while in sample B some specific regions are much thinner, down to the a few or single monolayer level. This thickness information has been determined by means of the **Digital Micrograph** software.

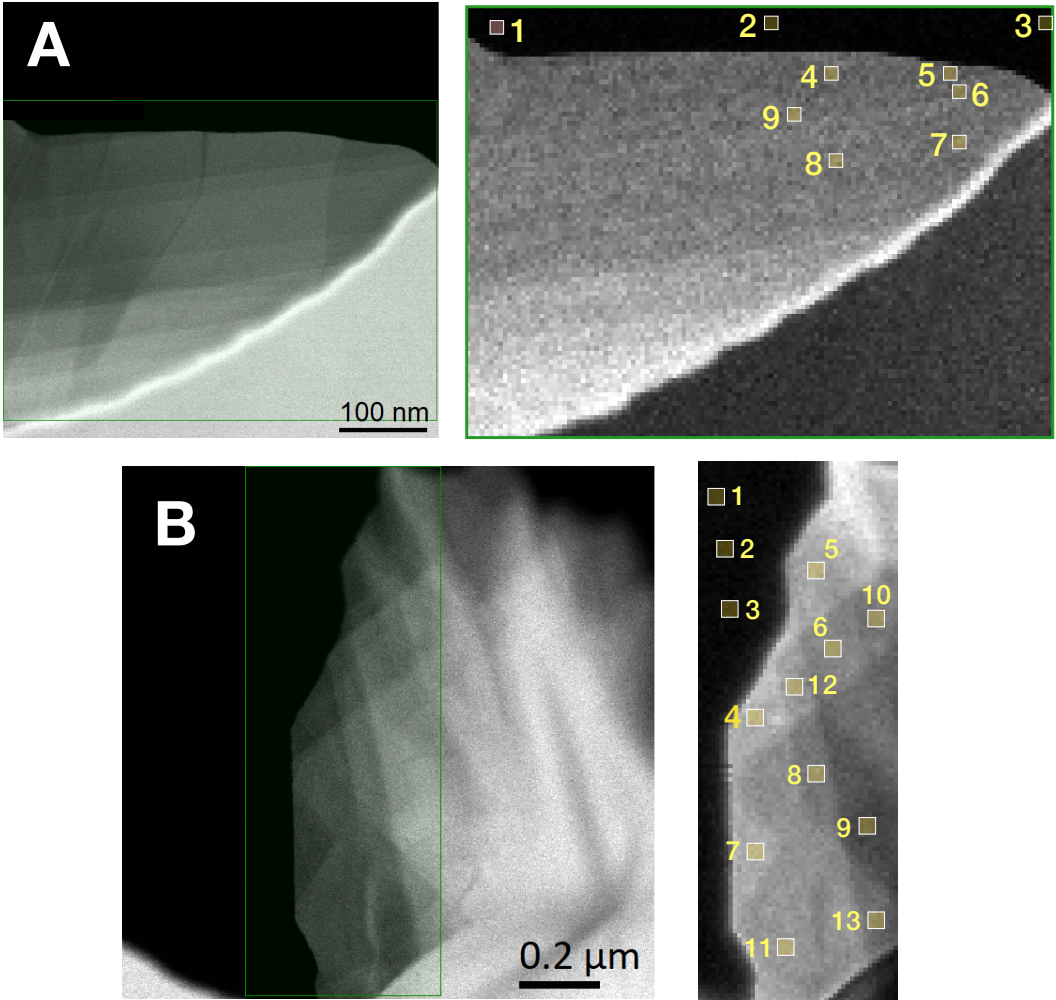


**Figure 7.1.** Low-magnification TEM images (left) and the corresponding spectral images (right panels) of two different regions of the WS<sub>2</sub> nanoflowers, denoted as sample A (upper) and sample B (lower panels) respectively. The spectral images have been recorded in the regions marked by a green square in the associated TEM images, and contain an individual EEL spectrum in each pixel. We indicate the locations where representative EEL spectra have been selected. In the left panel of sample B, the difference in contrast is correlated to the material thickness, with higher contrast indicating thinner regions of the nanostructure. The morphological differences between the two samples are discussed in the text.

One of the main goals of this study is demonstrating that our ZLP-subtraction method leads to a satisfactory performance for spectra recorded with different microscopes and operating conditions. With this motivation, the EELS measurements acquired on specimens A and B have been obtained varying both the microscopes and their settings. The TEM and EELS measurements acquired in specimen A are based on a JEOL 2100F microscope with a cold field-emission gun and equipped with an aberration corrector, operated at 60 kV. A Gatan GIF Quantum energy filter was used for the EELS analysis. The corresponding measurements on specimen B were recorded instead using a JEM ARM200F monochromated microscope operated at 60 kV, equipped with a GIF quantum ERS filter. See the Methods section at the end of this work for more details.

In Table 7.1 we collect the most relevant properties of the spectra collected in the locations indicated in Fig. 7.1 using the same format as in Table 6.1. Note that since the

spectra from samples A and B have been acquired with different microscopes, features of the ZLP such as the FWHM are expected to be different. From this table one can observe how the ZLP for the spectra acquired on sample A exhibit a FWHM about five times larger as compared to those of sample B. This difference in resolution can be understood from the fact that the EELS spectra from sample B, unlike those from sample A, were recorded with a TEM equipped with a monochromator.

Set	$t_{\text{exp}}$ (ms)	$E_b$ (keV)	$N_{\text{sp}}$	$N_{\text{dat}}$	$\Delta E_{\text{min}}$ (eV)	$\Delta E_{\text{max}}$ (eV)	FWHM (meV)
A	1	60	6	1918	-4.1	45.5	$470 \pm 10$
B	190	60	10	2000	-0.9	9.1	$87 \pm 5$

**Table 7.1.** Same as Table 6.1 now for the EEL spectra taken on specimens A and B. Note that the location on the WS<sub>2</sub> nanoflowers where each spectra has been recorded was indicated in Fig. 7.1.

In the following we will present the results for spectra that are representative for each of the two samples. The full set of spectra is available together with `EELSfitter`, the code used to produce the results of this analysis, whose installation and usage instructions are presented in Appendix A.

## 7.2 Subtraction procedure

Following the strategy presented in Sect. 5, again we combine the  $N_{\text{sp}}$  spectra recorded over each sample and we determine the experimental central values and uncertainties for the training points. Next, we need to determine the choice for hyperparameters  $\Delta E_I$  and  $\Delta E_{II}$ , as we only want to train on data that is different from zero within uncertainties. As explained in Sect. 5.3, we need the location of the first local minimum on all the spectra to set a bound for  $\Delta E_I$  and  $\Delta E_{II}$ . The representative plots can be observed in Fig. 7.2 and here it becomes clear how much information is contained within the intensity derivatives of the spectra. One can observe how the derivatives recorded in vacuum (corresponding to locations #1, #2, and #3 for both samples) are monotonically decreasing and slowly converge towards zero, whereas the derivatives recorded on different positions over a specimen behave very similar, capturing fluctuations that are typical for the corresponding sample.

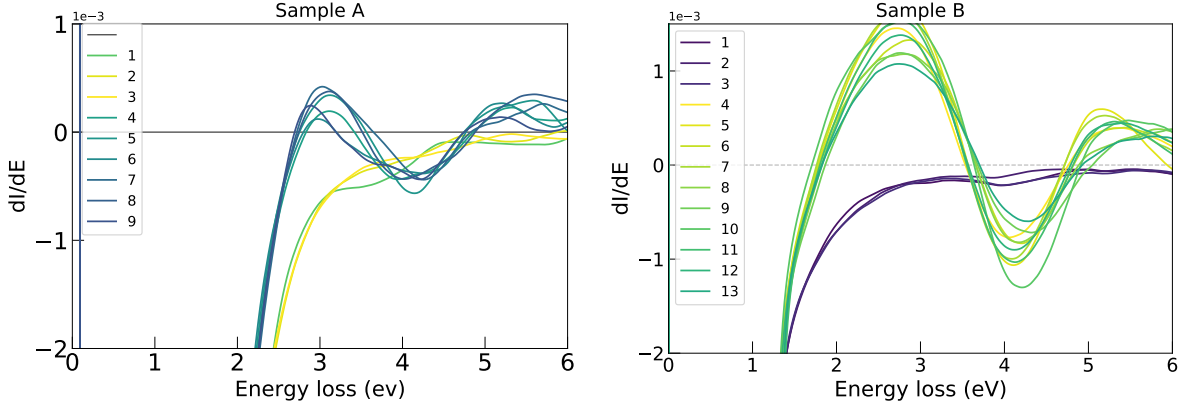


**Figure 7.2.** Plot of the first derivatives of the intensity profile over the energy loss, corresponding to the spectra recorded over Sample A (left) and B (right) at the locations indicated in Fig. 7.1. The derivatives have been normalized to the corresponding intensity in order to capture the relative size of the fluctuations.

Set	$\Delta E _{\min}$ (eV)	$\Delta E_I$ (eV)	$\Delta E_{II}$ (eV)
A	$2.70 \pm 0.06$	1.8	12
B	$1.80 \pm 0.04$	1.4	6

**Table 7.2.** The mean value and uncertainty of the first local minima,  $\Delta E|_{\min}$ , averaged over the spectra corresponding to samples A and B from Fig. 7.1. We also indicate the corresponding values of the hyper-parameters  $\Delta E_I$  and  $\Delta E_{II}$  defined in Fig. 5.5 used for the training of the neural network model.

In Table 7.2 we have collected the mean value and uncertainty of the first local minimum,  $\Delta E|_{\min}$ , averaged over the spectra corresponding to samples A and B from Fig. 7.1. From the uncertainties in  $\Delta E|_{\min}$ , we see that the location of the first minimum is relatively stable among all the spectra belonging to a given set. This indicates that the onset of the inelastic contributions  $I_{\text{inel}}$  does not change significantly as we move to different regions of the sample. We also indicate the corresponding values of the hyper-parameters  $\Delta E_I$  and  $\Delta E_{II}$  defined in Fig. 5.5. Recall that only the data points with  $\Delta E \leq \Delta E_I$  are used for training the neural network model. For  $\Delta E \geq \Delta E_{II}$  instead, the training set includes only the pseudo-data that implements the  $I_{\text{ZLP}}(\Delta E) \rightarrow 0$  constraint. The values for  $\Delta E_{II}$  were determined from the vacuum recorded spectra following the same procedure as explained in Sect. 6 and a plot similar to Fig. 6.2 can be observed in Fig. 7.3, where we show the ratio between the central experimental value of the vacuum EEL intensity and their corresponding uncertainty.

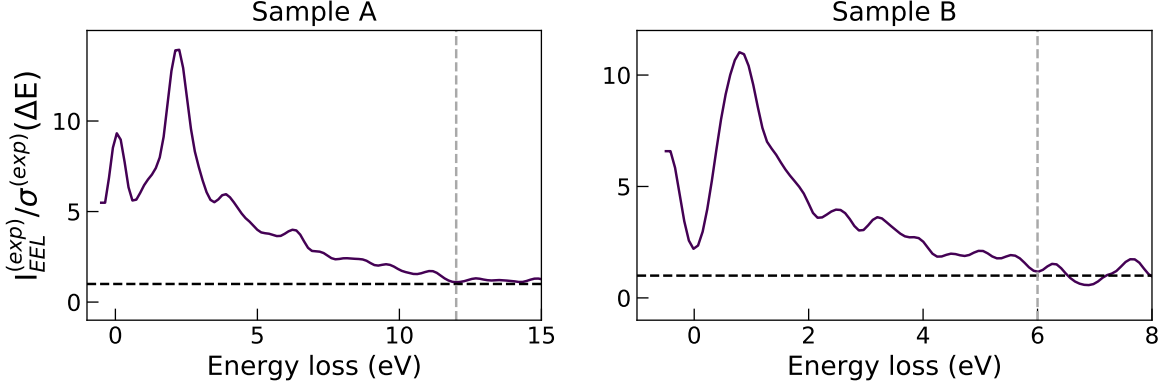


**Figure 7.3.** The ratio between the central experimental value of the total EELS intensity of the vacuum recorded peaks,  $I_{vac}^{(exp)}$ , and their corresponding uncertainty defined in Eq. 5.11. Results are shown for the mean of the spectra recorded over Sample A (left) and B (right). For both samples, spectrum positions #1, #2 and #3 in Fig. 7.1 were used to construct the vacuum central values. The vertical dashed lines mark the values of  $\Delta E$  for which this ratio becomes smaller than unity, which indicates when the input data starts to be dominated by the statistical noise.

We note that the values of  $\Delta E_{II}$  for this part are significantly higher than the ones found in Fig. 6.2. This could be ascribed to the fact that the vacuum spectra from sample A and B are recorded in proximity to a sample, and therefore effects from the sample are still present, although at a reduced rate.

The model training is performed for a range of  $\Delta E_I$  values subject to the condition that  $\Delta E_I \leq \Delta E_{min}$ . The optimal values of  $\Delta E_I$  listed in Table 7.2 are determined as follows. We evaluate the ratio between the derivative of the intensity distribution acquired on the specimen over the same quantity recorded in vacuum,

$$\mathcal{R}_{der}^{(j)}(\Delta E) \equiv \left\langle \frac{dI_{EEL}^{(exp)(j)}(\Delta E)/d\Delta E}{dI_{EEL}^{(exp)(j')}\Delta E)/d\Delta E} \right\rangle_{N'_{sp}}, \quad (7.1)$$

where  $j'$  labels one of the  $N'_{sp}$  vacuum spectra and the average is taken over all available values of  $j'$ . This ratio allows to identify a suitable value of  $\Delta E_I$  by establishing for which energy losses the shape (rather than the absolute value) of the intensity distributions recorded on the specimen starts to differ significantly from their vacuum counterparts. A sensible choice of  $\Delta E_I$  could for instance be given by  $\mathcal{R}_{der}(\Delta E_I) \simeq 0.9$ , for which derivatives differ at the 10% level. Note also that the value of the energy loss satisfying  $\mathcal{R}_{der}(\Delta E) = 0$  in Eq. (7.1) corresponds to the position of the first local minimum of the spectrum.

For both Sample A and B, the ratios calculated by means of Eq. (7.1) can be observed in Fig. 7.4 for two representative spectrum locations: we have used position #4 in both cases. Similar results are obtained for different positions.

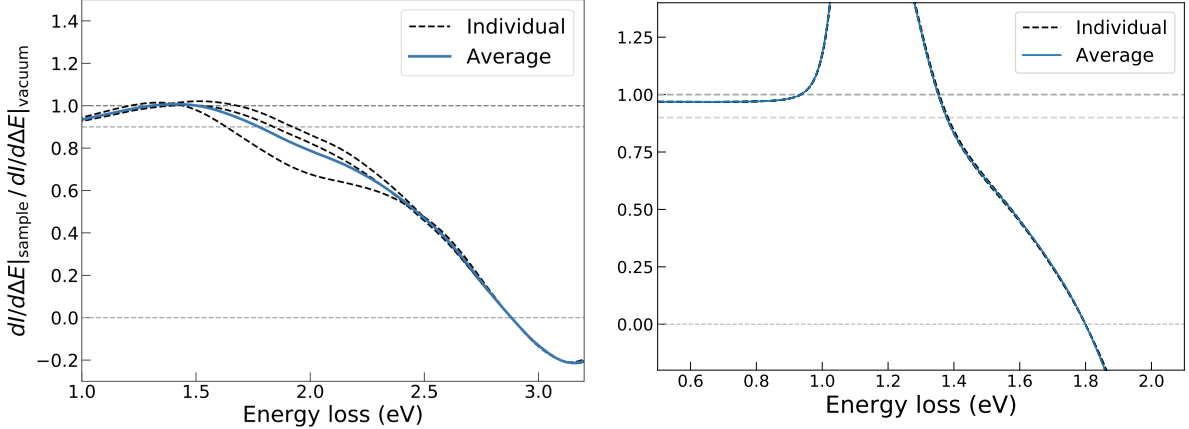


**Figure 7.4.** Plot of the ratio between the derivative of the intensity distribution acquired on the specimen over the same quantity recorded in vacuum, for spectrum position #4 in Sample A (left) and #4 in Sample B (right), indicated in Fig. 7.1.

In specimen A it is straightforward to find that  $\mathcal{R}_{\text{der}}(\Delta E_I) \simeq 0.9$  at an energy loss of 1.8 eV. For specimen B,  $\mathcal{R}_{\text{der}} \simeq 0.9$  at  $\Delta E = 1.4$  eV. In this case however, the ratio first starts to increase before it decreases again. This happens consistently for all three vacuum spectra: the three individual ratios can hardly be distinguished. It should be noted that the derivatives also differ at the 10% level when  $\mathcal{R}_{\text{der}} \simeq 1.1$ , which corresponds to  $\Delta E = 1$  eV. Still, we use the point where  $\mathcal{R}_{\text{der}} \simeq 0.9$  for the determination of  $\Delta E_I$ . The reason to favor this choice over  $\mathcal{R}_{\text{der}}(\Delta E_I) \simeq 1.1$  is from the physical interpretation: after this point, the derivative of the intensity distributions acquired on samples starts to approximate zero much faster than the derivatives in vacuum. When the effect of the sample kicks in, the intensity profile should flatten or increase rather than continue decreasing, which means the derivatives ratio should be *smaller* than unity. For this reason we choose  $\Delta E_I = 1.4$  eV as hyper-parameter for specimen B. Note that the validity of this choice will be checked later on.

Now that we have verified our choices of  $\Delta E_I$  and  $\Delta E_{II}$  for both samples, we can move to the results of the training sessions. The end result of the neural network training is a set of  $N_{\text{rep}} = 500$  replicas parametrising the ZLP,  $I_{\text{ZLP}}^{(\text{mod})(k)}(\Delta E)$ . Taking into account that we have  $N_{\text{sp}}$  individual spectra in each sample, the ZLP subtraction is performed individually for each Monte Carlo replica,

$$I_{\text{inel}}^{(\text{exp})(j,k)}(\Delta E) \equiv I_{\text{EELS}}^{(\text{exp})(j)}(\Delta E) - I_{\text{ZLP}}^{(\text{mod})(k)}(\Delta E), \quad \forall N_{\text{rep}}, \quad j = 1, \dots, N_{\text{sp}}, \quad (7.2)$$

from which statistical estimators can be evaluated as usual. For instance, the mean value for our model prediction for the  $j$ -th spectrum can be evaluated by averaging over the set of replicas,

$$\left\langle I_{\text{inel}}^{(\text{exp})(\text{(exp)}j)} \right\rangle (\Delta E) = \frac{1}{N_{\text{rep}}} \sum_{k=1}^{N_{\text{rep}}} I_{\text{inel}}^{(\text{mod})(j,k)}(\Delta E), \quad j = 1, \dots, N_{\text{sp}}, \quad (7.3)$$

and likewise for the corresponding uncertainties or correlations. For large values of  $\Delta E$  the model prediction reduces to the original spectra, since in that region the ZLP contribution vanishes,

$$I_{\text{inel}}^{(\text{exp})(j,k)}(\Delta E \gg \Delta E_I) \rightarrow I_{\text{EEL}}^{(\text{exp})(j)}(\Delta E), \quad \forall j, k. \quad (7.4)$$

For very small values of the energy loss, the contribution to the total spectra from inelastic scatterings is negligible and thus the subtracted model prediction Eq. (7.2) should be zero. However, this will not be the case in practice since the neural-net model is trained on the  $N_{\text{sp}}$  ensemble of spectra, rather than just on individual ones, and thus the expected  $\Delta E \rightarrow 0$  behaviour will only be achieved within uncertainties rather than at the level of central values. Therefore, in the zero-loss regime the subtracted spectrum will not vanish completely. To achieve the desired  $\Delta E \rightarrow 0$  limit, we apply a matching procedure as follows. We introduce another hyper-parameter,  $\Delta E_0 < \Delta E_1$ , such that one has for the  $k$ -th ZLP replica associated to the  $j$ -th spectrum the following behaviour:

$$\begin{aligned} I_{\text{ZLP}}^{(\text{mod})(j,k)}(\Delta E) &= I_{\text{EELS}}^{(\text{exp})(j)}(\Delta E), \quad \Delta E < \Delta E_0, \\ I_{\text{ZLP}}^{(\text{mod})(j,k)}(\Delta E) &= I_{\text{EELS}}^{(\text{exp})(j)} + \left( \xi_1^{(n_l)(k)}(\Delta E) - I_{\text{EELS}}^{(\text{exp})(j)}(\Delta E) \right) \times \mathcal{F}, \quad \Delta E_0 < \Delta E \leq \Delta E_1, \\ \mathcal{F} &= \exp \left( -\frac{(\Delta E - \Delta E_1)^2}{(\Delta E_0 - \Delta E_1)^2 \delta^2} \right), \\ I_{\text{ZLP}}^{(\text{mod})(j,k)}(\Delta E) &= \xi_1^{(n_l)(k)}(\Delta E), \quad \Delta E > \Delta E_1. \end{aligned} \quad (7.5)$$

In Eq. (7.5),  $\xi_1^{(n_l)(k)}$  indicates the output of the  $k$ -th neural network that parametrises the ZLP and  $\delta$  is a dimensionless tunable parameter. This matching procedure might look complex at first sight, however it states just the following:

- For  $\Delta E < \Delta E_0$ , the modeled ZLP is exactly the same as the original spectrum.
- Between  $\Delta E_0$  and  $\Delta E_1$ , the transition sets in to the ZLP model prediction.  $\mathcal{F}(\Delta E)$  represents a matching factor that ensures that the ZLP model prediction smoothly interpolates between  $\Delta E = \Delta E_0$  (where  $\mathcal{F} \ll 1$  and the original spectrum should be reproduced) and  $\Delta E = \Delta E_1$  (where  $\mathcal{F} = 1$  leaving the neural network output unaffected).
- At energy loss higher than  $\Delta E_1$ , the modeled ZLP is exactly the network prediction.

Here we adopt  $\Delta E_0 = \Delta E_1 - 0.5 \text{ eV}$ , having verified that results are fairly independent of this choice. Taking into account the matching procedure, we can slightly modify Eq. (7.2) to

$$I_{\text{inel}}^{(\text{mod})(j,k)}(\Delta E) \equiv I_{\text{EELS}}^{(\text{exp})(j)}(\Delta E) - I_{\text{ZLP}}^{(\text{mod})(j,k)}(\Delta E), \quad \forall N_{\text{rep}}, \quad j = 1, \dots, N_{\text{sp}}. \quad (7.6)$$

The ensemble of ZLP-subtracted spectra  $\{I_{\text{inel}}^{(\text{mod})(j,k)}\}$  can then be used to estimate the bandgap of the specimen in the region where they were acquired. Different approaches have been put forward to estimate the value of the bandgap from subtracted EEL spectra, *e.g.* by means of the inflection point of the rising intensity or a linear fit to the maximum positive slope [67]. Here we will adopt the approach of [14] where the behaviour of  $I_{\text{inel}}(\Delta E)$  in the onset region is modeled as

$$I_{\text{inel}}(\Delta E) \simeq A (\Delta E - E_{\text{BG}})^b, \quad \Delta E \geq E_{\text{BG}}, \quad (7.7)$$

and vanishes for  $E < E_{\text{BG}}$ , where both the bandgap value  $E_{\text{BG}}$  as well as the parameters  $A$  and  $b$  are extracted from the fit. The exponent  $b$  is expected to be  $b \simeq 1/2$  ( $3/2$ ) for a semiconductor material characterised by a direct (indirect) bandgap. For each of the  $N_{\text{sp}}$  spectra and the  $N_{\text{rep}}$  replicas we fit to Eq. (7.6) the model Eq. (7.7) within a range

taken to be  $[\Delta E_I - 0.5 \text{ eV}, \Delta E_I + 0.7 \text{ eV}]$ . One ends up with  $N_{\text{rep}}$  values for the bandgap energy and fit exponent for each spectra,

$$\left\{ E_{\text{BG}}^{(j,k)}, b^{(j,k)} \right\}, \quad k = 1, \dots, N_{\text{rep}}, \quad j = 1, \dots, N_{\text{sp}}, \quad (7.8)$$

from which again one can readily evaluate their statistical estimators. In the following, we will display the median and the 68% confidence level intervals for these parameters to account for the fact that their distribution will be in general non-Gaussian.

### 7.3 Bandgap analysis of sample A

We present first the results of the bandgap analysis of sample A, taking location #4 and #5 in Fig. 7.1 as representative spectra; compatible results are found for the remaining locations. As mentioned above, this region is characterised by a sizable thickness where WS<sub>2</sub> is expected to behave as a bulk material. Fig. 7.5 displays the original and subtracted EEL spectra together with the predictions of the ZLP model, where the bands indicate the 68% confidence level uncertainties and the central value is the median of the distribution. The inset shows the result of the polynomial fits using Eq. (7.7) to the subtracted spectrum together with the corresponding uncertainty bands.

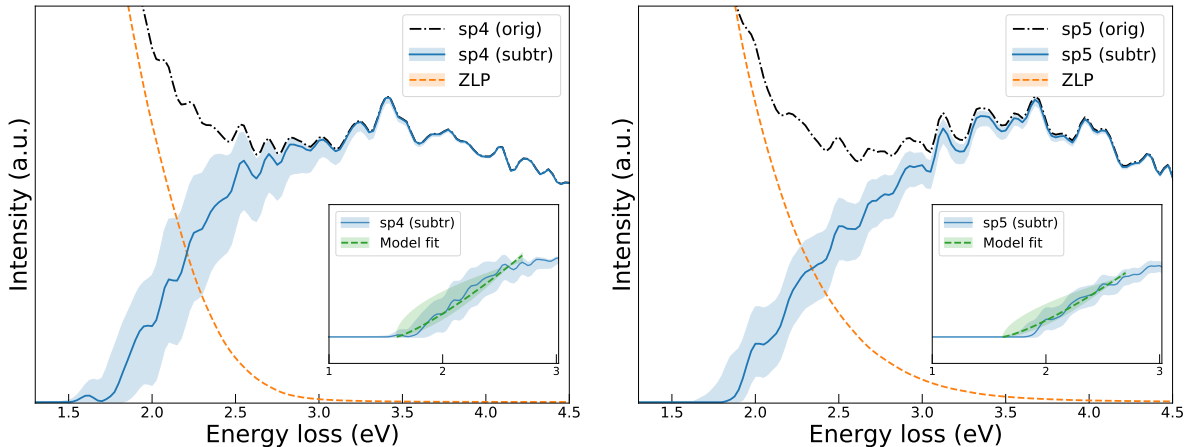


**Figure 7.5.** The original and subtracted EEL spectrum corresponding to location #4 (left) and #5 (right) of sample A in Fig. 7.1, together with the predictions of the ZLP model, where the bands indicate the 68% confidence level uncertainties. The inset displays the result of fitting Eq. (7.7) to the onset region of the subtracted spectrum.

One can observe how the ZLP model uncertainties are small at low  $\Delta E$  (due to the matching condition) and large  $\Delta E$  (where the ZLP vanishes), but become significant in the intermediate region where the contributions from  $I_{\text{ZLP}}$  and  $I_{\text{inel}}$  become comparable. It is worth emphasizing that these (unavoidable) uncertainties are neglected in most ZLP subtraction methods, and this is therefore the power of this method. The validity of our choice for the hyperparameter  $\Delta E_I$  (Table 7.2) can be verified *a posteriori* by evaluating the ratio

$$\mathcal{R}_{\text{abs}}^{(j)}(\Delta E_I) \equiv \left\langle I_{\text{ZLP}}^{(\text{mod})(j)} \right\rangle_{\text{rep}} / \left. I_{\text{EEL}}^{(\text{exp})(j)} \right|_{\Delta E = \Delta E_I}, \quad (7.9)$$

which in this case turns out to be  $\mathcal{R}_{\text{abs}} = 0.98$ . It is important to verify that  $\mathcal{R}_{\text{abs}}(\Delta E_I)$  is not too far from unity, indicating that the training dataset has not been contaminated by the inelastic contributions.

By requiring that  $\mathcal{R}_{\text{der}}^{(j)}(\Delta E_I) \simeq 0.9$  we obtain the value  $\Delta E_I = 1.8$  eV, which is used as baseline for the analysis. It should be noted that this choice is not unique, for example requiring  $\mathcal{R}_{\text{der}}^{(j)}(\Delta E_I) \simeq 0.8$  instead would have led to  $\Delta E_I = 2.0$  eV. It is therefore important to assess the stability of our results when the hyper-parameter  $\Delta E_I$  is varied around its optimal value.

With this motivation, we have performed the training over the EEL spectra for a range of  $\Delta E_I$  values to assess the stability of our results. In Fig. 7.6 we display the values of the exponent  $b$  and the bandgap energy  $E_{\text{BG}}$  obtained from spectrum #4 (left panel in Fig. 7.5) for variations of  $\Delta E_I$  around its optimal value (1.8 eV, indicated by the horizontal dashed line) by an amount of  $\pm 0.2$  eV. The central value and the error band for each value of  $\Delta E_I$  is evaluated as the median and the 68% CL interval over the  $N_{\text{rep}} = 500$  Monte Carlo replicas. We observe that the fit parameters for both  $b$  and  $E_{\text{BG}}$  are stable with respect to variations of  $\Delta E_I$ , with any shift in the central value contained within the uncertainty bands. We can therefore conclude that our approach is robust with respect to the choice of its hyper-parameters.

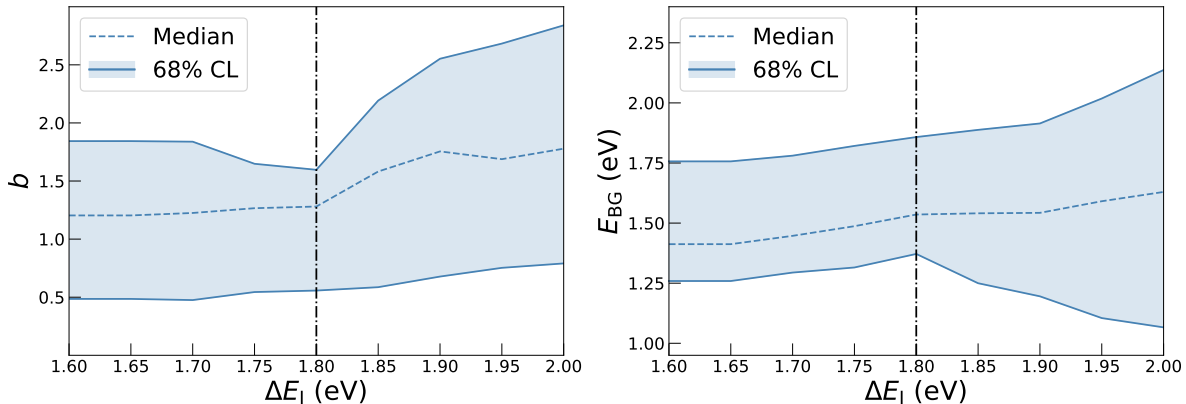


**Figure 7.6.** The values of the exponent  $b$  (left) and the bandgap energy  $E_{\text{BG}}$  (right panel) from the model Eq. (7.7) obtained from the subtracted spectrum sp14 as  $\Delta E_I$  is varied by  $\pm 0.2$  eV around its optimal value, indicated by the horizontal dashed line.

The final values for  $E_{\text{BG}}$  and  $b$  obtained in the analysis for spectrum 4 and 5 are

$$E_{\text{BG}}^{(4)} = 1.6_{-0.2}^{+0.3} \text{ eV}, \quad b^{(4)} = 1.3_{-0.7}^{+0.3} (\#4), \quad (7.10)$$

$$E_{\text{BG}}^{(5)} = 1.6_{-0.2}^{+0.2} \text{ eV}, \quad b^{(5)} = 1.3_{-0.5}^{+0.3} (\#5). \quad (7.11)$$

We thus find that for this specific region of the  $\text{WS}_2$  nanoflowers the model fit to the subtracted EEL spectrum exhibits a clear preference for an indirect bandgap (where  $b \simeq 1.5$ ), though a direct one ( $b \simeq 0.5$ ) cannot be excluded within uncertainties. This result is consistent with the theoretical expectations of the local electronic properties of bulk  $\text{WS}_2$ . Further, the value of  $E_{\text{BG}}$  is in agreement with previous determinations in the same material at the bulk level, such as those collected in Table 2.1. Consistent results are obtained for other locations over the specimen where spectra have been recorded. To demonstrate this, we show in Fig. 7.7 the fitted values for  $E_{\text{BG}}$  and  $b$  for all spectra in Sample A, all evaluated using  $\Delta E_I = 1.8$  eV for the model training. The error of the bandgap fit is different between the spectra, however what is most important is the fact that central values are stable within uncertainty bands. This implies that we find a favor

for an indirect bandgap for each of the locations on Sample A, which is what we would expect from theoretical expectations of bulk WS<sub>2</sub>.

To the best of our knowledge, these results represent the first EELS bandgap analysis of WS<sub>2</sub> nanostructures whose crystalline structure is based on mixed 2H/3R polytypes.

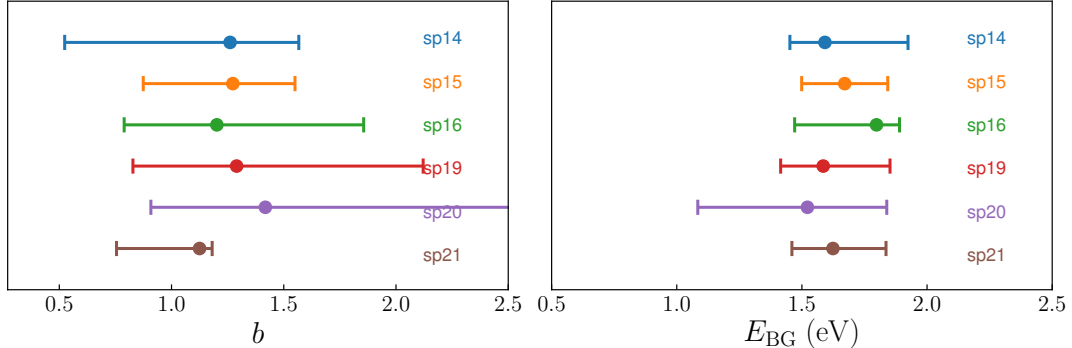


**Figure 7.7.** The values of the exponent  $b$  (left) and the bandgap energy  $E_{BG}$  (right panel) from the model Eq. (7.7) obtained from all the subtracted spectra in Sample A, for  $\Delta E_I$  at its optimal value (1.8 eV).

One final remark to make is that the polynomial fit to the bandgap onset comes with the introduction of new parameters to be tuned: one has to define the fitting range and bounds of the fit, introducing some degree of arbitrariness to the procedure. The influence of the chosen fit regime to the polynomial fit can be observed in Fig 7.8 below. Here, we have performed the polynomial fit using three different upper values of the energy loss:  $\Delta E_I + 0.5$ , 0.7, and 0.9 eV. The results for the exponents  $b$  are 1.37, 1.76 and 1.63 respectively. These values show a clear preference for an indirect bandgap, irrespective of the fitting regime. Values for  $E_{bg}$  are stable and equal to 1.6 eV for all cases.

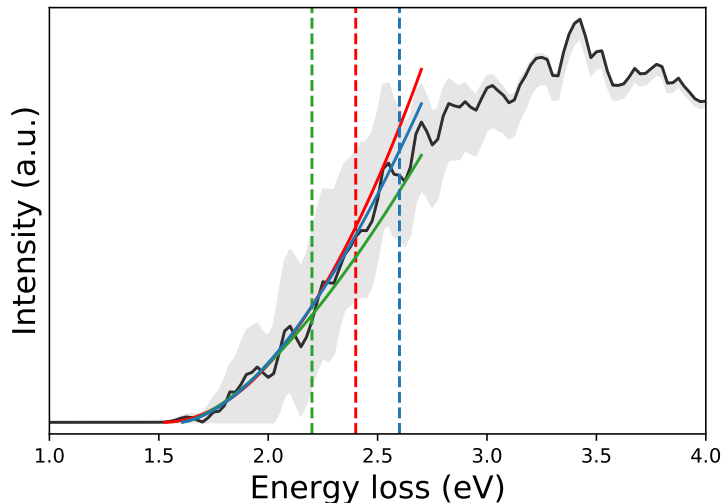


**Figure 7.8.** Bandgap fits for different fitting regimes:  $\Delta E_{fit} = [0, \Delta E_{lim,up}]$  with  $\Delta E_{lim,up} = \Delta E_I + 0.5$  (green), 0.7 (red), and 0.9 (blue). We find for the exponent  $b = 1.37$  (green), 1.76 (red), and 1.63 (blue). The bandgap energy is 1.6 eV irrespective of the fitting regime.

It is important to note that up to the subtraction procedure, methods are almost

completely free of manual finetuning of parameters. It is only for the analysis of the bandgap onset that few new tuning parameters are introduced, necessary to perform the bandgap onset fit, and changing these parameters yields slightly different fit results. This is a general flaw of the bandgap fitting procedure which is separate from our subtraction method.

## 7.4 Mapping excitonic transitions in sample B

We now discuss the results of the bandgap analysis of sample B, taking location #4 in Fig. 7.1 as representative spectrum; again, compatible results are found for the remaining positions. For the application of our ZLP subtraction strategy to the EEL spectra recorded in specimen B of the WS<sub>2</sub> nanoflowers (bottom panels in Fig. 7.1), the same criterion based on the derivative ratio Eq. (7.1) to select the hyper-parameter  $\Delta E_I$  was used. In this case, one finds a value of  $\Delta E_I \simeq 1.45$  eV, which is somewhat lower than the corresponding value obtained for sample A. The left panel of Fig. 7.9 displays the original and subtracted spectra corresponding to the representative location #4 of sample B together with the predictions of the ZLP model.

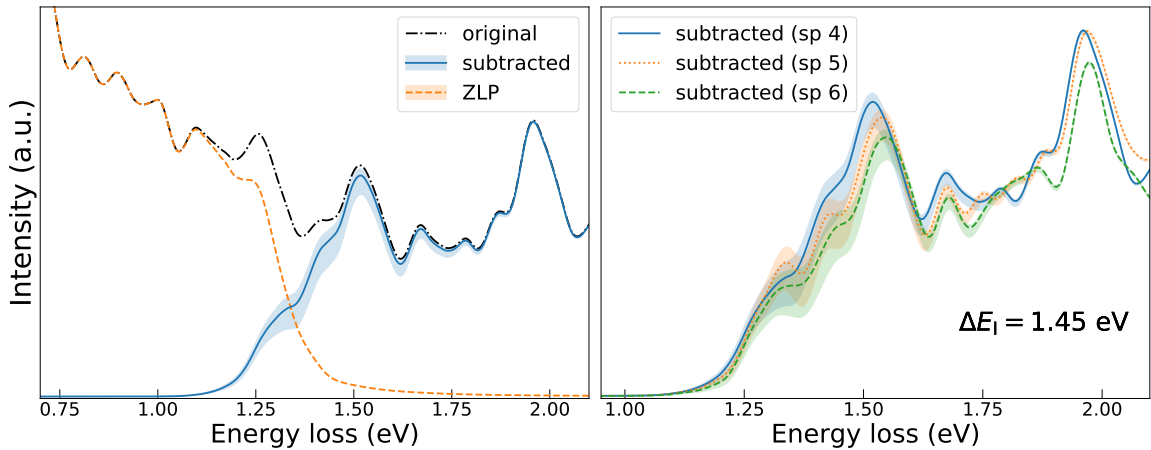


**Figure 7.9.** Left: the original and subtracted EEL spectra corresponding to location #4 of sample B in Fig. 7.1, together with the predictions of the ZLP model. The bands indicate the 68% confidence level uncertainties. Right: comparison of the ZLP-subtracted spectra from locations #4, #5, and #6 in sample B together with the corresponding model uncertainties. Note how several features of the subtracted spectra, in particular the peaks at  $\Delta E \simeq 1.5$ , 1.7 and 2.0 eV, are common across the three locations.

The main difference with respect to the spectra recorded in sample A is that in sample B, well-defined peaks appear in the subtracted spectrum already for very small values of  $\Delta E$ . In particular, we observe two pronounced peaks at  $\Delta E \simeq 1.5$  and 2.0 eV and a softer one near  $\Delta E \simeq 1.7$  eV. Additional features arise also for higher energy losses. There are two main explanations for the observed differences between the spectra recorded in sample A and B. The first one is that, while sample A is much thicker (bulk), sample B corresponds to thin, overlapping petals whose thicknesses can be as small as a few monolayers. The second is that the EELS measurements taken in sample A used a TEM without monochromator, while those in sample B were recorded with a monochromator, thereby achieving a superior spectral resolution. The average FWHM on Sample B is 87 meV, to be compared with 470 meV of sample A (see Table 7.1). This difference in

morphology between the specimens, together with the operation conditions of the TEM, could account for the observed differences between the two sets of spectra.

It is worth noting that our ZLP parametrisation and subtraction strategy performs well for all the spectra under consideration, irrespective of the spectral resolution of the TEM used for their acquisition. By comparing the left panel of Fig. 7.9 with Fig. 7.5, one observes that model uncertainties are larger in the latter case (sample A) than in the former (sample B), as expected from the superior spectral resolution of the EELS measurements taken on sample B. Nevertheless, the same approach has been used in both cases without the need of any fine-tuning or adjustments: of course, if the input spectra have been recorded with higher spectral resolution, the resulting ZLP model uncertainties will improve accordingly without the need for changing the procedure itself.

Given that the well-defined spectral features present in Fig. 7.9 appear close to the onset of the inelastic emissions,  $I_{\text{inel}}(\Delta E)$ , these spectra are not suitable for bandgap determination analyses. The reason is that the method of [14] used in sample A is only applicable under the assumption that there is a sufficiently wide region in  $\Delta E$  after the onset of  $I_{\text{inel}}$  to perform the polynomial fit of Eq. (7.7). This is clearly not possible for the spectra recorded in sample B, and indeed model fits restricted to  $\Delta E \leq 1.4$  eV are numerically very unstable. Instead of studying the bandgap properties, it is interesting to exploit the ZLP-subtracted results of sample B to characterise the local excitonic transitions of polytypic 2H/3R WS<sub>2</sub> that are known to arise in the ultra-low-loss region of the spectra.

Before being able to do this, however, one has to deal with the possible objection that the peaks present in the left panel of Fig. 7.9 are not genuine features, but rather fluctuations due to insufficient statistics that should be smoothed out before this region can be analysed. To tackle this concern, the right panel of Fig. 7.9 displays a comparison of the ZLP-subtracted spectra recorded in the (spatially separated) locations #4, #5 and #6 in sample B together with their model uncertainties. Both the position and the widths of the peaks at  $\Delta E \simeq 1.5$ , 1.7 and 2.0 eV remain stable, confirming that these are genuine physical features rather than fluctuations. In order to even further establish the presence of these peaks, we have created the right panel of Fig. 7.9 but now for a higher value of  $\Delta E_{\text{I}}$ . Results are shown in Fig. 7.10, now for two values of the hyperparameter  $\Delta E_{\text{I}}$ , 1.45 eV (left) and 1.55 eV (right panel). Note how these low-loss features of the subtracted spectra are still common across the three spectra, demonstrating that these peaks are constantly present also when using different hyper-parameters.

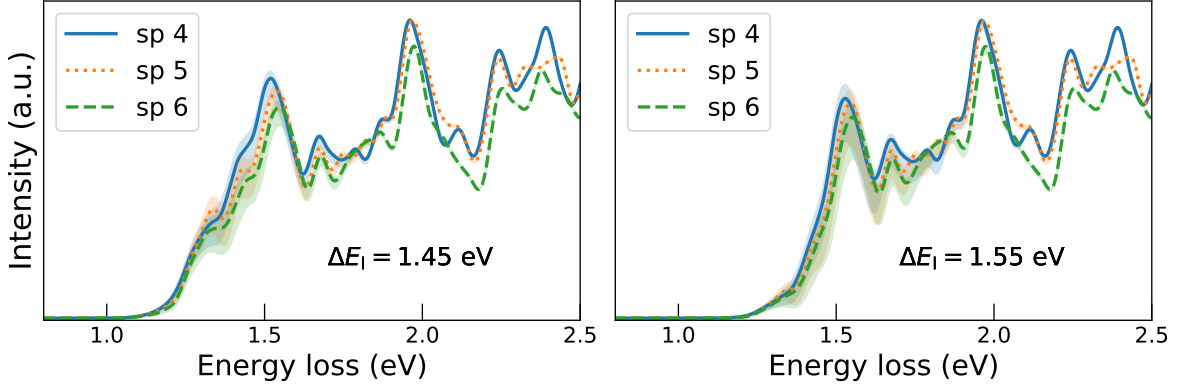


**Figure 7.10.** The ZLP-subtracted spectra from sample B corresponding to locations #4, #5, and #6 from Fig. 7.1 together with the corresponding model uncertainties. Results are shown for two values of the hyperparameter  $\Delta E_I$ , 1.45 eV (left) and 1.55 eV (right panel). Note how features of the subtracted spectra such as the peaks as  $\Delta E \simeq 1.5, 1.7$  and  $2.0$  are common across the three spectra.

These peaks in the ultra-low-loss region of the ZLP-subtracted EELS spectra recorded on thin, polytypic WS<sub>2</sub> nanostructures can be traced back to excitonic transitions. Their origin can be attributed to the formation of an electron-hole pair mitigated by the dielectric screening from the surrounding lattice [68]. In nanostructures with reduced dimensionality as well as in single layers of TMDs, exciton peaks arise with binding energies up to ten times larger than for bulk structures. In the optical spectra of TMDs, two strongly pronounced resonances denoted by A and B excitons are often observed, appearing at binding energies of 300 and 500 meV below the true band gap of the material [69]. Interestingly, this is in agreement with the features observed in Fig. 7.10 at  $\Delta E \simeq 1.5$  and 1.7 eV, which is exactly 300-500 meV below the true bandgap value expected for 2D structures of WS<sub>2</sub>, see Table 2.1.

We conclude that ZLP-subtracted spectra in sample B allow for establishing the presence of exciton peaks in the WS<sub>2</sub> nanoflowers down to  $\Delta E \simeq 1.5$  eV together with the associated uncertainty estimate. Further insights concerning the relationship between the exciton peaks in the ultra-low-loss region and the underlying crystalline structure could be obtained with computational techniques such as density functional theory.

## 8 Summary and outlook

In this work we have presented a novel, model-independent strategy to parametrise and subtract the omnipresent zero-loss peak that dominates the low-loss region of EEL spectra. Our strategy is based on machine learning techniques and provides an estimate of the uncertainties associated to both the input data and the procedure itself, which can then be propagated to physical predictions without any assumptions or approximations. We have demonstrated how, in the case of vacuum spectra, our approach is sufficiently flexible to accommodate several input variables corresponding to different operating conditions of the microscope, such as the exposure time and beam energy. Furthermore, we are able to reliably interpolate and extrapolate our predictions, *e.g.* for the expected FWHM of the ZLP, to operating conditions not included in the training dataset. When applied to spectra recorded over specimens, our approach makes it possible to separate the ZLP contribution from those arising from inelastic interactions with the sample. Thanks to this subtraction procedure, one can fully exploit the valuable physical information contained in the ultra low-loss region of the spectra.

As a proof of concept, we have applied the ZLP subtraction strategy to EEL spectra recorded in two samples of WS<sub>2</sub> nanoflowers characterised by a 2H/3R polytypic crystalline structure. Measurements taken in the first sample, representing a relatively thick region of WS<sub>2</sub> (bulk material), were used to determine the local value of the bandgap energy  $E_{BG}$  and to assess whether the nature of this bandgap is direct or indirect. A model fit to the onset of the inelastic intensity distribution leads to a bandgap energy  $E_{BG} \simeq 1.6^{+0.3}_{-0.2}$  eV and exhibits a clear preference for an indirect bandgap. Our findings are consistent with previous studies, both of theoretical and of experimental nature, concerning the bandgap structure of bulk WS<sub>2</sub>.

Subsequently, we have applied our method to a thinner sample of the WS<sub>2</sub> nanoflowers, a region composed by overlapping petals with varying thicknesses that can be as small as a few monolayers. We have demonstrated how in this case, the ZLP-subtracted results allow for the characterisation of the local excitonic transitions that arise in the ultra-low-loss region. By charting the bandgap region of 2H/3R polytypic WS<sub>2</sub>, we identify two strong peaks at  $\Delta E \simeq 1.5$  and 2 eV and we show how these features are consistent when comparing spatially-separated locations in sample B, independent of our choice of hyper-parameters.

The power of this method is that it provides an associated uncertainty estimate, which makes it possible to robustly establish the statistical significance of each of these features in the ultra-low-loss region.

The approach presented in this work could be extended in several directions. First, there are a couple of cross-validations that can be done to test the robustness of our model. For example, when additional operating conditions of the microscope are included as input variables, *e.g.* aperture width or temperature, to verify to which extent the ZLP parametrisations obtained for a specific microscope can be generalised to a completely different TEM. Furthermore, in order to validate our predictions for other operating conditions of the microscope, we could use actual measurements to measure for example the FWHM as a function of the beam energy  $E_b$  or the exposure time  $t_{exp}$ , as shown in Fig. 6.7. It would also be interesting to use a sample which is known to exhibit a direct bandgap without dominating excitonic transitions in the low-loss regime, to verify that

the bandgap fitting procedure works also for this case.

Concerning the physical interpretation of the low-loss region of EEL spectra, our method could be applied to study the bandgap properties for different types of nanostructures built upon 2D or specifically TMD materials, such as MoS<sub>2</sub> nanowalls [70] and vertically-oriented nano-sheets [71]. In addition to bandgap characterisation, this ZLP-subtraction strategy should allow the detailed study of other phenomena relevant for the interpretation of the low-loss region such as plasmons, excitons, phonon interactions, and intra-band transitions. One could also further exploit the observed peaks in the ultra-low-loss regime in WS<sub>2</sub> monolayers, infer their binding energies and verify if these peaks indeed correspond to the expected exciton transitions. Furthermore, the subtracted EEL spectra could be used to study features in the energy-gain region of EEL spectra, which is at the left-hand side of the ZLP, which helps to develop novel cooling strategies for atomically thin TMD nanostructures.

Another possible application of the strategy presented in this work would be the automation of the study of spectral TEM images, such as those displayed in the right panels of Fig. 7.1, where each pixel contains an individual EEL spectrum. Here machine learning methods would provide a useful automated method to gain insight from these spectra with minimal identify human intervention, since there is no need to process each spectrum individually.

## Methods

The EEL spectra used for the training of the vacuum ZLP model presented in Sect. 6 were collected in a ARM200F Mono-JEOL microscope equipped with a GIF continuum spectrometer and operated at 60 kV and 200 kV. For these measurements, a slit in the monochromator of  $2.8 \mu\text{m}$  was used. The TEM and EELS measurements acquired in Specimen A for the results presented in Sect. 7 were recorded in a JEOL 2100F microscope with a cold field-emission gun equipped with aberration corrector operated at 60 kV. A Gatan GIF Quantum was used for the EELS analyses. The convergence and collection semi-angles were 30.0 mrad and 66.7 mrad respectively. The TEM and EELS measurements acquired for Specimen B in Sect. 7 were recorded using a JEM ARM200F monochromated microscope operated at 60 kV and equipped with a GIF quantum ERS. The convergence and collection semi-angles were 24.6 mrad and 58.4 mrad respectively in this case, and the aperture of the spectrometer was set to 5 mm.

# Supplementary Material

## A Installation and usage of EELSfitter

In this appendix we provide some instructions about the installation and the usage of the `EELSfitter` code developed in this work. The code is available from its GitHub repository

<https://github.com/LHCfitNikhef/EELSfitter>

and is composed by a number of Python scripts. The code requires a working installation of Python3 and the following libraries: NumPy, TensorFlow (v2), pandas, SciPy and scikit-learn.

`Load_data.py` This script reads the spectrum intensities and create data-frames to be used for training the neural network. It reads out the EEL spectra intensities, automatically selects the energy loss at which the peak intensity occurs and shifts the dataset such that the peak intensity is centered at  $\Delta E = 0$ . Further, for each spectrum it returns the normalized intensity by normalizing over the total area under the spectrum. The output is two datasets, `df` and `df_vacuum` which contain the information on the in-sample and in-vacuum recorded spectra respectively. The user needs to upload the spectral data in .txt format to the 'Data' folder and make sure that the vacuum and in-sample spectra are added to the appropriate one. For each of the spectra the minimum and maximum value of the recorded energy loss need to be set manually in `Eloss_min` and `Eloss_max`.

`Fitter.ipynb` This script is used to run the neural network training on the data that was uploaded using `load_data.py`. It involves a number of pre-processing steps to determine the hyper-parameters  $\Delta E_I$  and  $\Delta E_{II}$  and then it automatically prepares and cuts the data before it is fed to the neural network to start the training. It is structured as follows:

- *Importing libraries and spectral data* from the `load_data.py` script.
- *Evaluate  $\Delta E_I$  from the intensity derivatives.* In order to determine the value for the hyper-parameter  $\Delta E_I$ , a dataframe `df_dx` is created and it calculates the derivatives of each of the in-sample recorded spectra, stored as `df_dx['derivative y*']`, where \* is any of the in-sample recorded spectra. The first crossing of any of the derivatives with zero is determined and stored as the value of  $\Delta E_I$ .
- *Evaluate  $\Delta E_{II}$  for the pseudo-data.* It calculates the mean over all vacuum spectra, `df_mean`, and the ratio of the intensity to the experimental uncertainty for each value of  $\Delta E$ , `df_mean['ratio']`. The value of  $\Delta E_{II}$  is then determined as the energy loss at which this ratio drops below 1 and is stored together with the value of  $\Delta E_I$  as the hyper-parameters for training. However, if one wishes to use other values for these parameters, for instance for cross-validating the best value for  $\Delta E_I$ , these can also be adjusted manually.
- *Experimental data processing.* The next step is to keep only the data points with  $\Delta E \leq \Delta E_I$  and dropping the points with higher energy losses. Experimental central values and uncertainties are calculated by means of equal width discretization, for which the number of bins has to be set as `nbins`. The default value is 32, which

means that 32 training inputs are spread equally over the range  $[\Delta E_{\min}, \Delta E_{\max}]$ . Note that the logarithm of the intensity is used as training inputs, because this facilitates the optimization of the neural network ( $I_{\text{EEL}}$  being a steeply falling function of  $\Delta E$ ). The code translates this back to the original intensity values after the training.  $N_{\text{pd}}$  pseudo datapoints are added in the range  $[\Delta E_{\text{II}}, \Delta E_{\max}]$ , where  $\Delta E_{\max}$  is the maximum energy loss value of the recorded spectra. The values for  $N_{\text{pd}}$  and  $\Delta E_{\max}$  should be changed manually by setting them in `max_x` and `N_pseudo`. The output is a dataframe `df_full` containing all training data and pseudo data points, corresponding to a total of  $N_{\text{in}} (= n_{\text{bins}} + N_{\text{pd}})$  training inputs.

- *Initialize the NN model*, where the code defines the neural network architecture and prepares the data inputs to feed them to the neural network for training. The function `make_model()` allows to define the number of hidden layers and nodes per layer. The default architecture is 1-10-15-5-1.
- *Initialize data for NN training*. Here the code prepares the recorded spectra to be used as inputs for the neural network. First, we initiate placeholders for the variables `x`, `y` and `sigma` which allow us to create our operations and build our computation graph, without needing the data itself. The dimension of the placeholder is defined by `[None, dim]` where 'dim' should be set to the dimension of the corresponding variable. In this case the input is one-dimensional, so `dim=1`. These placeholders are used to define `predictions`, which is in fact a placeholder that is used later to make predictions on inputs `x`. Also, we define a vector `predict_x` that is used to make a direct prediction after training on each of the replicas. It consists of  $N_{\text{pred}}$  data points in the energy loss range `[pred_min, pred_max]`.
- *Create the Monte Carlo replicas*. The final step to be taken before we can start training is the creation of sample of  $N_{\text{rep}}$  Monte Carlo replicas of the original EEL spectra, following the procedure described in Sect. ???. This is done automatically using the experimental intensities `train_y` and uncertainties `train_sigma` for a total of `Nrep` replicas. The output is an  $(N_{\text{in}}, N_{\text{rep}})$  vector containing all the MC replicas.
- *Train the neural networks*. The final part of the script, where the NN training is carried out, is based on the function `function_train()` that implements the strategy presented in Sect. 5.3. The cost function, optimizer and learning rate are defined here, together with a 'saver' used to save the network parameters after each optimization. We start a loop over `Nrep` replicas to initiate a training session on each of the individual replicas in series. For each iteration, the  $k$ -th replica is selected from the sample of  $N_{\text{rep}}$  replicas. The data is split into 80% training and 20% validation data, this partition is done at random for each replica. The resulting `train_y` and `test_y` arrays are used as training and validation labels. The total number of training epochs per session is defined in `training_epochs`. The script displays intermediate results after each number of epochs defined by `display_step`. Running the session object over the optimizer and cost function requires knowledge about the values of `x` and `sigma`, which are defined inside the `feed_dict` argument. After each epoch the average training validation costs are evaluated and the network parameters updated accordingly.

Once the maximum number of epochs had been reached, the optimal stopping point is determined by taking the absolute minimum of the validation cost and restoring

the corresponding network parameters by means of the 'saver' function. From this network graph, one can directly output the prediction on the values of `train_x` and the results are stored in the array `predictions_values`. It is also possible to make predictions on any input vector of choice by feeding the vector `predict_x` to the network, which outputs an array `extrapolation`.

The datafiles that are stored upon successfully executing this script are the following:

- `Prediction_k` contains the energy loss `train_x`, the MC training data `train_y` and the ZLP prediction made on the array `train_x`, where  $k$  is the  $k$ -th replica.
- `Cost_k` contains the training and validation error for the  $k$ -th replica stored after each display step. The minimum of the validation array is used to restore the optimal neural network parameters.
- `Extrapolation_k` contains the arrays `predict_x` and the ZLP predictions made on these values.

These text files can be retrieved later to make new ZLP predictions without the need to repeat the training procedure. Further, we store the optimal network parameters after each training session in the folder 'Models/Best\_models'. These can be loaded at a later stage to make predictions for an arbitrary set of input variables.

Running the loop over all replicas in series, using an input array of  $\sim 50$  training points and a total number of training epochs of 25000 per session, takes approximately 20 seconds per optimization ( $\sim 200$  replicas per hour).

`predictions.ipynb` This script is used to analyse the predictions from the trained neural networks that have been stored in the text files indicated above.

- *Import libraries and spectral data* from the `load_data.py` script.
- *Create dataframes with all individual spectra.* In order to later subtract all the predictions from the original individual spectra, we create a datafile `original` which contains the intensity values for each of the original input spectra restricted to the region between `E_min` and `E_max`.
- *Load result files.* In order to import the files that were stored during the NN training, one should input to this script the right directions to find the prediction .txt files by adjusting the lines `path_to_data` and `path_predict`, `path_cost` and `path_extrapolate`, containing the predictions, cost function data and the extrapolation predictions respectively.
- *Post-selection criteria.* Here one select the datafiles that satisfy suitable post-fit selection criteria, such as the final error function being smaller than a certain threshold. Once these datasets have been selected and stored in an array called `use_files`, we move on to the evaluation of the ZLP predictions.
- *Subtraction.* At this step the code uses the function `matching()` to implement the matching procedure described in Sect. 7. It also automatically selects the values of  $\Delta E_I$  and  $\Delta E_{II}$  for the training session. If the user aims to extract the bandgap

properties from the onset of  $I_{\text{inel}}$ , the `bandgap()` function can be used to fit Eq. 7.7 to the onset region.

Here the code loops over the  $N_{\text{rep}}$  replicas and reads each prediction from the extrapolation data file `predict_x`. For each replica  $k$ , the code creates a datafile containing the original spectra intensities (`original['x*']` and `original['y*']`), the predicted ZLP for this replica (`prediction y`) and the predicted ZLP after matching with each spectrum (`match *`). For each replica we subtract the matched spectrum from the original spectrum to obtain the desired subtraction: `dif * = original * - match *`. This is done for each of the total of the replicas and all these results are stored in the `total_replicas` dataframe. This file is saved in ‘Data/results/replica\_files’ such that a user can retrieve them at any time to calculate the statistical estimators such as prediction means and uncertainties.

- *Evaluate the subtracted spectra.* Here the code creates a `mean_rep` file that contains all the median predictions and the upper and lower bounds of the 68% confidence intervals for the predicted ZLP, matched spectra and the subtracted spectra, for each of the original recorded spectra originally given as an input. A graphical representation of the result is then produced, showing the original spectrum, the matched ZLP and the ZLP-subtracted spectrum including uncertainty bounds.

We emphasize that the `predictions_pretrained_net.ipynb` script is similar to the `predictions.ipynb` script, but can be executed stand-alone without the need to train again the neural networks, provided that the model parameters corresponding to some previous training with the desired input settings are available. The item **load result files** is now replaced by **create result files**, which can be done by importing the pre-trained nets from the `Models` folder.

## References

- [1] K. S. Novoselov, A. K. Geim, S. V. Morozov, D. Jiang, Y. Zhang, S. V. Dubonos, I. V. Grigorieva, and A. A. Firsov, *Electric Field Effect in Atomically Thin Carbon Films*, Science **306** (2004) 666–669.
- [2] K. S. Novoselov, A. Mishchenko, A. Carvalho, and A. H. C. Neto, *2D materials and van der Waals heterostructures*, Science **353** (2016).
- [3] M. Terauchi, T. M., K. Tsuno, and M. Ishida, *Development of a high energy resolution electron energy-loss spectroscopy microscope*, Journal of Microscopy **194** (2005) 203–209.
- [4] B. Freitag, S. Kujawa, P. Mul, J. Ringnalda, and P. Tiemeijer, *Breaking the spherical and chromatic aberration barrier in transmission electron microscopy*, Ultramicroscopy **102** (2005) 209–214.
- [5] M. Haider, S. Uhlemann, E. Schwan, H. Rose, B. Kabius, and K. Urban, *Electron microscopy image enhanced*, Nature **392** (1998) 768–769.
- [6] J. Geiger, *Inelastic Electron Scattering in Thin Films at Oblique Incidence*, Phys. Stat. Sol. **24** (1967) 457–460.
- [7] H. R. Daniels, R. Brydson, A. Brown, and B. Rand, *Quantitative valence plasmon mapping in the TEM: viewing physical properties at the nanoscale*, Ultramicroscopy **96** (2003) 547–558.
- [8] B. Schaffer, K. Riegler, G. Kothleitner, W. Grogger, and F. Hofer, *Monochromated, spatially resolved electron energy-loss spectroscopic measurements of gold nanoparticles in the plasmon range*, Micron **40** (2008) 269–273.
- [9] R. Erni, N. D. Browning, Z. Rong Dai, and J. P. Bradley, *Analysis of extraterrestrial particles using monochromated electron energy-loss spectroscopy*, Micron **35** (2005) 369–379.
- [10] H. Ibach and D. Bruchmann, *Observation of Surface Phonons on Ni(111) by Electron Energy-Loss Spectroscopy*, Physical Review Letters **44** (1980) 36–39.
- [11] B. Rafferty and L. Brown, *Direct and indirect transitions in the region of the band gap using electron-energy-loss spectroscopy*, Physical Review B **58** (1998) 10326.
- [12] M. Stöger-Pollach, *Optical properties and bandgaps from low loss EELS: Pitfalls and solutions*, Nano Lett. **39** (2008) 1092–1110.
- [13] F. García de Abajo, *Optical excitations in electron microscopy*, RevModPhys **82** (2010) 209–256, [[arXiv:0903.1669](https://arxiv.org/abs/0903.1669)].
- [14] B. Rafferty, S. Pennycook, and L. Brown, *Zero loss peak deconvolution for bandgap EEL spectra*, Journal of Electron Microscopy **49** (2000) 517–524.
- [15] R. Egerton, Electron Energy-Loss Spectroscopy in the Electron Microscope. Plenum Press, 1996.

- [16] A. Dorneich, R. French, H. Müllejans, et al., *Quantitative analysis of valence electron energy-loss spectra of aluminium nitride*, Journal of Microscopy **191** (1998) 286–296.
- [17] K. van Benthem, C. Elsässer, and R. French, *Bulk electronic structure of SrTiO<sub>3</sub>: Experiment and theory*, Journal of Applied Physics **90** (2001).
- [18] S. Lazar, G. Botton, et al., *Materials science applications of HREELS in near edgestructure analysis an low-energy loss spectroscopy*, Ultramicroscopy **96** (2003) 535–546.
- [19] R. Egerton and M. Malac, *Improved background-fitting algorithms for ionization edges in electron energy-loss spectra*, Ultramicroscopy **92** (2002) 47–56.
- [20] J. T. Held, H. Yun, and K. A. Mkhoyan, *Simultaneous multi-region background subtraction for core-level EEL spectra*, Ultramicroscopy **210** (2020) 112919.
- [21] C. S. Granerød, W. Zhan, and Øystein Prytz, *Automated approaches for band gap mapping in STEM-EELS*, Ultramicroscopy **184** (2018) 39–45.
- [22] K. L. Fung, M. W. Fay, S. M. Collins, D. M. Kepaptsoglou, S. T. Skowron, Q. M. Ramasse, and A. N. Khlobystov, *Accurate EELS background subtraction, an adaptable method in MATLAB*, Ultramicroscopy **217** (2020) 113052.
- [23] **The NNPDF Collaboration**, R. D. Ball et al., *A determination of parton distributions with faithful uncertainty estimation*, Nucl. Phys. **B809** (2009) 1–63, [[arXiv:0808.1231](#)].
- [24] R. D. Ball et al., *Parton distributions with LHC data*, Nucl.Phys. **B867** (2013) 244, [[arXiv:1207.1303](#)].
- [25] **NNPDF Collaboration**, R. D. Ball et al., *Parton distributions for the LHC Run II*, JHEP **04** (2015) 040, [[arXiv:1410.8849](#)].
- [26] **NNPDF Collaboration**, R. D. Ball et al., *Parton distributions from high-precision collider data*, Eur. Phys. J. **C77** (2017), no. 10 663, [[arXiv:1706.00428](#)].
- [27] S. E. van Heijst, M. Masaki, E. Okunishi, H. Kurata, and S. Conesa-Boj, *A nanoscale tulip garden: Fingerprinting plasmons and excitons in the petals of 2h/3r - ws2 nanoflowers*, .
- [28] R. J. Toh, Z. Sofer, J. Luxa, D. Sedmidubský, and M. Pumera, *3R phase of MoS<sub>2</sub> and WS<sub>2</sub> outperforms the corresponding 2H phase for hydrogen evolution*, Chemical Communications **53** (2017) 3054–3057.
- [29] M. Chhowalla, H. S. Shin, G. Eda, L.-J. Li, K. P. Loh, and H. Zhangs, *The chemistry of two-dimensional layered transition metal dichalcogenide nanosheets*, Nature Chemistry **5** (2013) 263–275.
- [30] Q. H. Wang, K. Kalantar-Zadeh, A. Kis, J. N. Coleman, and M. S. Strano, *Electronics and optoelectronics of two-dimensional transition metal dichalcogenides*, Nature Nanotechnology **7** (2012).

- [31] A. Splendiani, L. Sun, T. Li, et al., *Emerging Photoluminescence in Monolayer MoS<sub>2</sub>*, *Nano Lett.* **10** (2010) 1271–1275.
- [32] R. Bhandavat, L. David, and G. Singh, *Synthesis of Surface-Functionalized WS<sub>2</sub> Nanosheets and Performance as Li-Ion Battery Anodes*, *J. Phys. Chem. Lett.* **3** (2012) 1523–1530.
- [33] W. Na, K. Kim, J.-U. Lee, and H. Cheong, *Davydov splitting and polytypism in few-layer MoS<sub>2</sub>*, *2D Materials* **6** (2018) 015004.
- [34] L. J. Li, E. C. T. O'Farrell, K. P. Loh, B. G. Eda, and A. H. C. Neto, *Controlling many-body states by the electric-field effect in a two-dimensional material*, *Nature* **529** (2016) 185–189.
- [35] D. Braga, I. G. Lezama, H. Berger, and A. F. Morpurgo, *Quantitative Determination of the Band Gap of WS<sub>2</sub> with Ambipolar Ionic Liquid-Gated Transistors*, *NanoLetters* **12** (2012) 5218.
- [36] S. Jo, N. Ubrig†, H. Berger, A. B. Kuzmenko†, and A. F. Morpurgo, *Mono- and Bilayer WS<sub>2</sub> Light-Emitting Transistors*, *Nano Letters* **14** (2014) 2019–2025.
- [37] J. G. et al, *Electronic Properties of Bulk and Monolayer TMDs: Theoretical Study Within DFT Framework (GVJ-2e Method)*, *Physica Status Solidi A* **214** (2007).
- [38] K. Kam and B. Parkinson, *Detailed photocurrent spectroscopy of the semiconducting group VIB transition metal dichalcogenides*, *J. Phys. Chem.* **86** (1982) 463–467.
- [39] H. Shi, H. Pan, Y.-W. Zhang, and B. I. Yakobson, *Quasiparticle band structures and optical properties of strained monolayer MoS<sub>2</sub> and WS<sub>2</sub>*, *PHYSICAL REVIEW B* **87** (2013) 155304.
- [40] J. Hillier and R. Baker, *Microanalysis by Means of Electrons*, *Journal of Applied Physics* **15** (1944) 663.
- [41] H. Rose, *Optics of high-performance electron microscopes*, *Science and Technology of Advanced Materials* **9** (2008).
- [42] H. Nerl, K. Winther, and F. Hage, *Probing the local nature of excitons and plasmons in few-layer MoS<sub>2</sub>*, *2D Materials and Applications* **1** (2016) [[arXiv:1702.00359](https://arxiv.org/abs/1702.00359)].
- [43] J. Bruley and L. Brown, *Analytical Electron Microscopy Workshop*, The Institute of Metals, London, Edited by G.W. Lorimer, 1987.
- [44] O. Krivanek, N. Dellby, J. Hachtel, and M. Hotz, *Progress in ultrahigh energy resolution EELS*, *Ultramicroscopy* **203** (2009) 60–67.
- [45] F. Hofer, F.-P. Schmidt, et al., *Fundamentals of electron energy-loss spectroscopy*, *Materials Science and Engineering* **109** (2016) 1183–1188.
- [46] J. Park, S. Heo, et al., *Bandgap measurement of thin dielectric films using monochromated STEM-EELS*, *Ultramicroscopy* **109** (2008) 1183–1188.

- [47] U. Bangert, A. Harvey, D. Freundt, and R. Keyse, *Highly spatially resolved electron energy-loss spectroscopy in the bandgap regime of GaN*, *Journal of Microscopy* **188** (1998) 237–242.
- [48] J. Hachtel, A. Lupini, and J. Idrobo, *Exploring the capabilities of monochromated electron energy loss spectroscopy in the infrared regime*, *Scientific Reports* **8** (2018) 5637.
- [49] H. Tenailleau and J. M. Martin, *A new background subtraction for low-energy EELS core edges*, *Journal of Microscopy* **116** (1992) 297–306.
- [50] B. Reed and M. Sarikaya, *Background subtraction for low-loss transmission electron energy-loss spectroscopy*, *Ultramicroscopy* **93** (2002) 25–37.
- [51] M. Bosman, M. Watanabe, D. Alexander, and V. Keast, *Mapping chemical and bonding information using multivariate analysis of electron energy-loss spectrum images*, *Ultramicroscopy* **106** (2006) 1024–1032.
- [52] G. Kothleitner and F. Hofer, *EELS performance measurements on a new high energy resolution imaging filter*, *Micron* **34** (2003) 211–218.
- [53] E. Greplova et al., *Quantum parameter estimation with a neural network*, .
- [54] J. Rojo, “Machine learning: a new toolbox for theoretical physics.” University Study Guide, 2019.
- [55] R. Hecht-Nielsen, *Neural Networks for Perception*. Elsevier, 1992.
- [56] O. M. Gordon and P. J. Moriarty, *Machine learning at the (sub)atomic scale: next generation scanning probe microscopy*, *Machine Learning: Science and Technology* **1** (2020) 023001.
- [57] Y. Zhang, A. Mesaros, and K. e. Fujita, *Machine learning in electronic-quantum-matter imaging experiments*, *Nature* **570** (2020) 484–490.
- [58] B. Jany, A. Janas, and F. Krok, *Retrieving the Quantitative Chemical Information at Nanoscale from Scanning Electron Microscope Energy Dispersive X-ray Measurements by Machine Learning*, *Nano Letters* **17** (2017) 6520–6525.
- [59] M. Ziatdinov, O. Dyck, A. Maksov, X. Li, X. Sang, K. Xiao, R. R. Unocic, R. Vasudevan, S. Jesse, and S. V. Kalinin, *Deep Learning of Atomically Resolved Scanning Transmission Electron Microscopy Images: Chemical Identification and Tracking Local Transformations*, *ACS Nano* **11** (2017) 12742–12752.
- [60] S. R. Young, D. C. Rose, T. P. Karnowski, S.-H. Lim, and R. M. Patton, *Optimizing deep learning hyper-parameters through an evolutionary algorithm*, in *Proceedings of the Workshop on Machine Learning in High-Performance Computing Environments*, MLHPC ’15, (New York, NY, USA), Association for Computing Machinery, 2015.
- [61] M. Ziatdinov, O. Dyck, A. Maksov, X. Li, X. Sang, K. Xiao, R. R. Unocic, R. Vasudevan, S. Jesse, and S. V. Kalinin, *Deep learning of atomically resolved scanning transmission electron microscopy images: Chemical identification and*

- tracking local transformations*, ACS Nano **11** (2017), no. 12 12742–12752, [<https://doi.org/10.1021/acsnano.7b07504>]. PMID: 29215876.
- [62] K. de Haan, Z. S. Ballard, Y. Rivenson, Y. Wu, and A. Ozcan, *Resolution enhancement in scanning electron microscopy using deep learning*, Scientific Reports **9** (2019), no. 1 12050.
  - [63] S. Kiyohara, T. Miyata, K. Tsuda, and T. Mizoguchi, *Data-driven approach for the prediction and interpretation of core-electron loss spectroscopy*, Nature Scientific Reports **8** (2018) 13548.
  - [64] J. Rojo, *Machine Learning tools for global PDF fits*, in 13th Conference on Quark Confinement and the Hadron Spectrum, 9, 2018. [arXiv:1809.04392](https://arxiv.org/abs/1809.04392).
  - [65] J. Gao, L. Harland-Lang, and J. Rojo, *The Structure of the Proton in the LHC Precision Era*, Phys. Rept. **742** (2018) 1–121, [[arXiv:1709.04922](https://arxiv.org/abs/1709.04922)].
  - [66] S. Forte, L. Garrido, J. I. Latorre, and A. Piccione, *Neural network parametrization of deep-inelastic structure functions*, JHEP **05** (2002) 062, [[hep-ph/0204232](https://arxiv.org/abs/hep-ph/0204232)].
  - [67] S. Schamm and G. Zanchi, *Study of the dielectric properties near the band gap by VEELS:gap measurement in bulk materials*, Ultramicroscopy **96** (2003) 559–564.
  - [68] A. Hanbicki, M. Currie, G. Kioseoglou, A.L. Friedman, and B.T. Jonker, *Measurement of high exciton binding energy in the monolayer transition-metal dichalcogenides WS<sub>2</sub> and WSe<sub>2</sub>*, Solid State Communications **204** (2016) 16–20.
  - [69] B. Kaviraj and D. Sahoo, *Physics of excitons and their transport in two dimensional transition metal dichalcogenide semiconductors*, RSC Advances (2019).
  - [70] M. Tinoco, L. Maduro, and S. Conesa-Boj, *Metallic edge states in zig-zag vertically-oriented mos<sub>2</sub> nanowalls*, Scientific Reports **9** (2019), no. 1 15602.
  - [71] M. Bolhuis, J. Hernandez-Rueda, S. E. van Heijst, M. Tinoco Rivas, L. Kuipers, and S. Conesa-Boj, *Vertically-oriented mos<sub>2</sub> nanosheets for nonlinear optical devices*, Nanoscale **12** (2020) 10491–10497.

## Acknowledgements

My endless gratitude goes to my official and unofficial supervisors Sonia and Juan. Sonia, your incredible enthusiasm, support and optimism have been a driving force throughout my project. Unfortunately, due to Covid, it only lasted one month that we could spend our coffee breaks in real life together with Luigi. I'm glad that we shared many more virtually.

Thank you also for introducing a mysterious professor from Amsterdam to my project, who would later become my most-dialed contact in my contact list. Juan, I'm so thankful for your engagement and never-ending pool of ideas, for all the time that you put in our collaboration, and also for being critical and down to earth. I think we made a super good team.

Luigi, thank you for regularly checking up on me, sending me random memes and introducing me in the PhD bar when it was still allowed, although still I wasn't allowed there.

Finally, I want to thank my parents, brother and friends for their support along the way, always there to offer some love and distraction when my eyes were squared.

Laurien